Technische Universität München
TUM School of Natural Sciences

Influence of Salts on the Response Behavior of PNIPMAM Thin Films

Julija Reitenbach, M. Sc.

Vollständiger Abdruck der von der TUM School of Natural Sciences der Technischen Universität München zur Erlangung einer

Doktorin der Naturwissenschaften (Dr. rer. nat.)

genehmigten Dissertation.

Vorsitz: Prof. Dr. Martin Zacharias

Prüfende der Dissertation:

1. Prof. Dr. Peter Müller-Buschbaum
2. Prof. Dr. Wilhelm Auwärter

Die Dissertation wurde am 18.12.2024 bei der Technischen Universität München eingereicht und durch die TUM School of Natural Sciences am 28.01.2025 angenommen.

Abstract

The solvent uptake behavior and the volume phase transition of thermoresponsive poly(*N*-isopropylmethacrylamide) (PNIPMAM) thin films is investigated. By the addition of water soluble salts, the responsiveness towards different vapor atmospheres is studied in terms of the macroscopic swelling degree as well as interactions on a molecular level. On the macroscopic scale, the time dependent swelling degree is followed by spectral reflectance (SR) and time-of-flight neutron reflectivity (ToF-NR), whereas contributions from individual molecular interactions are analyzed using Fourier-transform infrared spectroscopy (FTIR). The volume phase transition of the swollen films is induced by leveraging the cononsolvency effect. Furthermore, the influence of the presence of ions on the cononsolvency effect is investigated, reveling a strong dependence of the response behavior on the specific salt introduced. In view of practical applications, this provides an easily tunable parameter to modify the responsivness of nanodevices, such as sensors or nanoswitches.

Zusammenfassung

Das Lösungsmittelaufnahmeverhalten und der Volumen-Phasenübergang von thermoresponsiven Poly(*N*-isopropylmethacrylamid) (PNIPMAM) Dünnfilmen werden untersucht. Durch die Zugabe von wasserlöslichen Salzen wird die Empfindlichkeit gegenüber verschiedenen Dampfatmosphären in Bezug auf den makroskopischen Quellungsgrad sowie auf intrinsische Wechselwirkungen auf molekularer Ebene untersucht. Auf der makroskopischen Skala wird der zeitabhängige Quellungsgrad mittels spektraler Reflexion (SR) und Flugzeit-Neutronenreflektometrie (ToF-NR) verfolgt, während die Beiträge einzelner molekularer Wechselwirkungen mittels Fourier-Transform-Infrarotspektroskopie (FTIR) analysiert werden. Der Volumen-Phasenübergang der gequollenen Filme wird durch Ausnutzung des *cononsolvency* Effekts herbeigeführt. Darüber hinaus wird der Einfluss der Anwesenheit von Ionen auf den *cononsolvency* Effekt untersucht, wobei sich eine starke Abhängigkeit der Empfindlichkeit vom eingebrachten Salz zeigt. Im Hinblick auf praktische Anwendungen bietet dies einen leicht anpassbaren Parameter, um die Sensitivität von Nanobauteilen wie Sensoren oder Nanoschaltern zu verändern.

Contents

List of Abbreviations

AIBN	azobisisobutyronitrile
DMF	*N*-dimethylformamide
DMSO	dimethyl sulfoxide
DTGS	deuterated triglycine sulfate
FTIR	Fourier-transform infrared spectroscopy
GISAXS	grazing incidence small-angle X-ray scattering
HSAB	hard and soft acids and bases
ILL	Institute Laue-Langevin
KEC	knife edge collimator
LCST	lower critical solution temperature
NR	neutron reflectivity
PNIPAM	poly(*N*-isopropylacrylamide)
PNIPMAM	poly(*N*-isopropylmethacrylamide)
PTFE	poly(tetrafluoroethylene)
SDD	sample detector distance
SEC	size exclusion chromatography
SIE	specific ion effect
SLD	scattering length density
SR	spectral reflectance
TFE	2,2,2-trifluoroethanol

THF ..... tetrahydrofuran

ToF ..... time-of-flight

ToF-NR ..... time-of-flight neutron reflectivity

UCST ..... upper critical solution temperature

VPTT ..... volume phase transition temperature

XRR ..... X-ray reflectivity

1. Introduction

Stimuli-responsive polymers are a class of polymers, which undergo physical changes upon an external stimulus such as light irradiation [1], pH [2], cosolvent composition [3], temperature [4], pressure [5], ionic strength [6], or upon the application of a magnetic or electric field [7]. As a response to the external trigger, the properties of a polymer, such as its solubility, viscosity, conductivity, color, and conformation can be altered, even reversibly [8,9]. Among such responsive polymers, thermoresponsive polymers change their conformation upon variations in temperature and therefore are attractive in the fields of tissue engineering, drug delivery, soft robotics, and nanosensors [10–12]. In solution, thermoresponsive polymers undergo a transition from an expanded coil to a collapsed globule state, which leads to a phase separation at certain temperatures [13,14]. For thermoresponsive polymers featuring a lower critical solution temperature (LCST), a phase separation occurs at temperatures above the LCST. For upper critical solution temperature (UCST)-type polymers the phase transition takes place at temperatures below the UCST [15]. Consequently, below the LCST and above the UCST the polymer is soluble in all proportions. The transition temperature of a given thermoresponsive polymer can be influenced by various factors, such as the molar mass [16], the end groups [16,17], and the tacticity [18,19], or by the addition of salts [20,21] or cosolvents [3,22]. The ion-induced modulation of the transition temperature is typically dependent on the ion identity and therefore is referred to as a so-called specific ion effect (SIE) [23,24]. The most prominent example for a specific ion effect was reported and analyzed by Hofmeister for the solubility of proteins in water in the presence of various salts [25,26]. According to Hofmeister, the ion type either causes a stabilization or destabilization of a macromolecule in solution. It was proposed, that highly charged ions enhance the structuring of nearby water, thereby decreasing the solubility of the macromolecule. Consequently, these ions are referred to as water structure makers or kosmotropes. In contrast, chaotropes or water structure breakers increase the solubility due to their weakly charged nature. In line with the observations of Hofmeister, similar effects on the solubility of thermoresponsive polymers have been reported, which demonstrated that the transition temperature is highly affected by the presence of ions [27]. Thus, the addition of salts has emerged as a versatile tool to tailor the transition temperature and the solubility of a polymer. Furthermore, the addition of a cosolvent can have an impact on the aforementioned properties of a ther-

moresponsive polymer. In this context, two contrary phenomena, the cosolvency and the cononsolvency effect, can be explored. The cosolvency effect describes the phenomenon in which a polymer becomes soluble in the presence of two poor solvents. In contrast, the cononsolvency effect refers to the phenomenon of a polymer being insoluble in a mixture of two good solvents. Like in the case of specific ion effects, the variation in the solubility originates from the impact of the cosolvent on the transition temperature of the polymer and therefore can be used to tailor the response behavior. Leveraging specific ion effects and the co(non)solvency phenomenon, the design of advanced functional thermoresponsive materials with fine-tuned response behaviors becomes feasible and broadens the scope of their potential applications.

In addition to polymers in solution, the coil-to-globule transition by temperature variation is also found for different sample architectures such as polymer brushes [28] or physically and chemically cross-linked polymers [14]. In these architectures the coil-to-globule transition is referred to as a volume phase transition [29]. In general, bulk materials offer advantageous mechanical stability albeit with the drawback of a less pronounced response behavior compared to polymers in solution. The balance between high responsiveness and enhanced mechanical stability can be achieved with polymers in thin film geometry up to $\approx$ 100 nm thickness. [30]. These thin films possess a high surface-to-volume ratio and therefore a large exposable area for a stimulus. Furthermore, mechanical stability is provided by chemical or physical cross-links between the functional groups of the polymer [8,30]. For the purpose of application, the volume change can be leveraged by exposure of a swollen thin film – also referred to as a polymer gel – to an external stimulus. The conformational change of the polymer chains results in a variation of the swelling degree, which can exemplarily be used for the ejection of pharmaceutically active small molecules in targeted drug delivery or for the generation of signals by translation of the response to an electrical current [8,31–33]. For medical use of thermoresponsive polymers, it is essential that the polymer is biocompatible and that it features a transition temperature close to the human body temperature. In this regard, the non-toxic poly(*N*-isopropylacrylamide) (PNIPAM) has become an attractive choice, due to having its LCST in aqueous solution at around 32 °C [34–36]. PNIPAM primarily consists of a hydrophobic polymer backbone and isopropyl bearing amide groups in the side chains. Through slight modifications of the molecular structure of the polymer, significant changes of the LCST are obtained. For instance, in poly(*N*-isopropylmethacrylamide) (PNIPMAM), the addition of a methyl group at each repeating unit at the polymer backbone shifts the LCST to 44 °C in aqueous solution, which amounts to an increase of 12 °C [37–41]. This is explained by the modification of the molecular structure influencing the inter- and in-

trapolymer interactions as well as hydrogen bond formation and thus the LCST [40,42–45].

In the present thesis, the influence of salt addition on the response behavior of PNIPMAM thin films in different solvent vapor atmospheres is investigated. The films are fabricated on silicon substrates, which geometrically constrains the polymer chains and creates a high surface-to-volume ratio. By exposing the thin films to water vapor and subsequently to a water/acetone vapor mixture atmosphere, the swelling and cononsolvency induced contraction are studied with the addition of either $Mg(ClO_4)_2$, $Mg(NO_3)_2$, or $NaClO_4$ as shown in Figure 1.1.

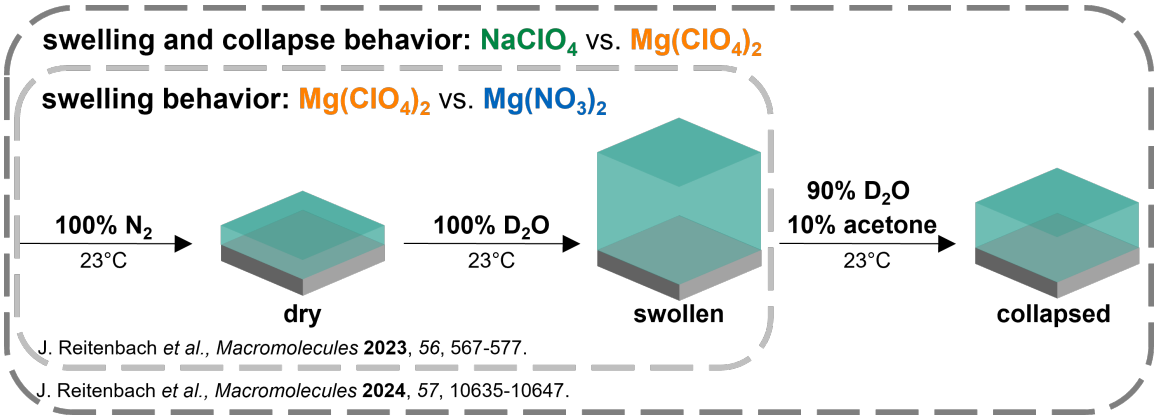

Figure 1.1.: Schematic overview over the investigation of the volume phase transition behavior of PNIPMAM thin films with the addition of either $Mg(ClO_4)_2$, $Mg(NO_3)_2$, or $NaClO_4$ under different solvent vapor atmospheres. The swelling under D_2O and collapse behavior under a mixture of D_2O and acetone is illustrated.

Creating a solvent vapor atmosphere in close vicinity to the film surface, the incorporation of the solvent molecules into the polymer matrix leads to a volume expansion accompanied with a thickness increase. The swelling process is thereby dependent on the solvent quality, the added ion type, the diffusion rate, and the humidity itself. The presence of salts inside the polymer matrix further influences the overall interactions between the components and therefore impacts the swelling ability of a polymer film. The contraction of a swollen film by the addition of a cononsolvency inducing cosolvent enables a film to possess two distinct and stable swollen states. The extent of the volume phase transition hereby decides the applicability of the polymer film in devices such as nanoswitches, nanosensors, and actuators. In general, tailoring the response behavior to be faster and stronger to enhance the sensitivity of the device is beneficial, which is demonstrated to be achievable by the addition of salts. This circumvents the necessity to synthesize polymers with the desired requirements by instead tuning the response behavior of already existing materials. Experimentally, the response behavior is followed by appropriate time-

resolved measurement techniques. The macroscopic thickness evolution of the polymer thin film is measured by *in situ* spectral reflectance (SR) or time-of-flight neutron reflectivity (ToF-NR). In addition, ToF-NR allows for the calculation of the evolution of the solvent content inside the film over time from the scattering length density (SLD). By applying a physically sensible fit model to the measured ToF-NR reflectivity curves further information about the vertical distribution of components, interface layers, and interface or surface roughnesses is obtained. This information gives insights into the uptake and release behavior of solvent molecules into the film, as well as into the presence of enrichment/depletion layers from the migration, preferential absorption, or accumulation of components. The vertical distribution of salts inside PNIPMAM thin films is investigated by X-ray reflectivity (XRR). Due to the different scattering mechanisms, i.e., neutrons scatter at the nuclei and X-rays at the electron shell, a combination of neutron and X-ray experiments complement each other due to the different scattering abilities of the individual components. The difference in the scattering ability results in a contrast, which enables the differentiation of the individual species. The neutron SLD of elements varies randomly with the atomic number and is highly sensitive towards different isotopes. This is different to X-rays, where the SLD strongly depends on the atomic number and therefore follows a trend across the periodic table. Furthermore, to study the evolving molecular interactions during the swelling and collapse processes of the film, *in situ* Fourier-transform infrared spectroscopy (FTIR) is used to resolve the participation of the individual functional groups of the polymer, solvent molecules, and salt additives. The combination of time-resolved ToF-NR and FTIR links the macroscopic response behavior to the underlying molecular processes, giving detailed mechanistic insights. On top of that, the order of solvation events is analyzed by subjecting the FTIR spectra to 2D correlation analysis, which further allows for the resolution of overlapping signals.

For a comprehensive understanding of the presented research topic, Chapter 2 provides the fundamental theoretical background about parameters influencing the LCST of thermoresponsive polymers in thin film geometry. The basic concepts of specular reflectivity, necessary for the physical principles of the measurement techniques in Chapter 3 are presented. In Chapter 4, the unique sample environments for the characterization of polymer thin films in solvent vapor atmospheres are introduced and the individual materials as well as the sample fabrication methods are addressed in Chapter 5.

In the first study presented in Chapter 6, the swelling behavior of PNIPMAM thin films in D_2O vapor atmosphere with the addition of either $Mg(ClO_4)_2$ or $Mg(NO_3)_2$ is investigated. D_2O is used instead of H_2O to increase the contrast between the polymer and

the solvent molecules for ToF-NR experiments and to avoid overlapping signals from the solvent molecules and the prominent polymer signals in FTIR measurements. By investigating the system with XRR, ToF-NR, and FTIR, the impact of the anion variation on the swelling behavior is investigated. The addition of $Mg(NO_3)_2$ increases the responsiveness of PNIPMAM thin films to D_2O vapor in terms of swelling ratio a change to over 70 % compared to the salt-free and $Mg(ClO_4)_2$-containing PNIPMAM film. Complementary, by *in situ* FTIR measurements the interactions between water molecules, charged ions, polar functional groups and hydrophobic alkyl moieties of the polymer are identified.

Based on the results for the swelling behavior presented in Chapter 6, the study in Chapter 7 extends the investigation to the influence of different salts on the cononsolvency induced volume phase transition of an initially swollen PNIPMAM thin film. Instead of varying the anions, different perchlorate salts with cations of different valence, namely Na^+ and Mg^{2+}, are investigated by using a combination of XRR, ToF-NR, and FTIR in accordance with the investigations presented in Chapter 6. The addition of $NaClO_4$ enables to further increase the swelling ability of PNIPMAM thin films and successfully enhances the magnitude of the volume phase transition upon subsequent introduction of a mixed D_2O/acetone vapor atmosphere.

The combined investigations from both research projects are summarized in Chapter 8 and aim to provide perspective into the not yet fully understood fields of the specific ion effects and the cononsolvency effect in thermoresponsive polymer thin films.

2. Theoretical Background

This chapter provides theoretical principles of polymer solubility, as well as the origin of the temperature dependence for thermoresponsive polymers and how the transition temperature can be influenced by the addition of a cosolvent. Furthermore, the effect of ions on the solubility as well as on the transition temperature of polymers are discussed. The presented theories are further extended for the behavior of polymers in thin film geometry. The last section addresses the basic concepts of specular reflectivity necessary for the physical principles of the measurement techniques presented in Chapter 3.

2.1. Polymer Solubility

The solubility of a polymer in a given solvent is determined by the Gibbs free energy G, which describes the tendency of systems to mix with each other. The Gibbs free mixing enthalpy ΔG_m is given as [46,47]

$$\Delta G_m = \Delta H_m - T\Delta S_m \,, \tag{2.1}$$

where T is the temperature, and H_m and S_m are the mixing enthalpy and entropy terms, respectively. For most systems, ΔS_m is positive due to the increase of possible arrangements in the mixed system. For $\Delta G_m < 0$ the polymer will dissolve in the solvent, which is the case when the entropy term dominates the enthalpy term. However, if $\Delta G_m > 0$, i.e., when $\Delta H_m > T\Delta S_m$, the polymer will be insoluble. Furthermore, if ΔH_m and ΔS_m have equal signs, the solubility is primarily dependent on the temperature. In absence of interactions between the components in an ideal non-interacting system, $\Delta H_m = 0$ and the occurrence of mixing is only depending on the entropy. However, for real systems such as polymers in solution, $\Delta H_m \neq 0$ due to the formation of polymer-polymer and polymer-solvent interactions. Moreover, due to the long-chain nature of polymers, consisting of covalently linked monomer units, ΔS_m is decreased compared to a solution of small molecules. According to the definition by Boltzmann the entropy is given as [46,47]

$$S = k_B \ln \Omega \,, \tag{2.2}$$

where k_B is the Boltzmann constant and Ω describes the number of possible arrangements. To account for the chemical nature of polymers, the enthalpy and entropy term have to be adjusted, which is described by the Flory–Huggins theory [48–50]. Here, the solution is described by a lattice, in which each solvent molecule and each segment of a polymer chain occupies one lattice site, which is shown in Figure 2.1.

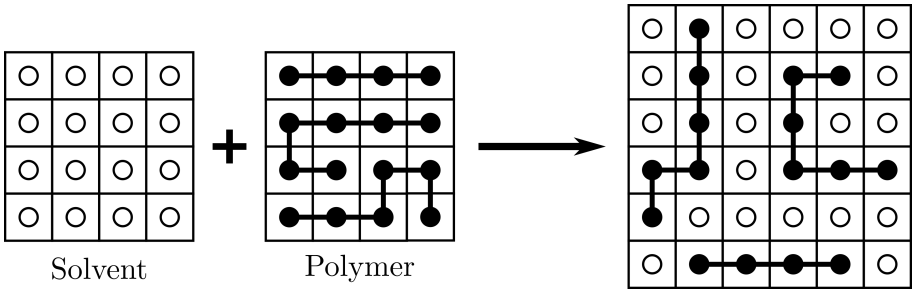

Figure 2.1.: Depiction of the Flory–Huggins lattice model [46,47] for the description of polymers in solution. Solvent molecules are shown as hollow circles, segments of a polymer chain as solid black circles, and bonds between polymer segments as solid black lines.

In solution, the number of possible arrangements Ω is according to Flory–Huggins theory described by the number of lattice sites n and the total volume ϕ of a system as

$$\Omega = n\phi\,. \tag{2.3}$$

Before mixing, a given component i occupies the whole lattice space and therefore $\phi_i = 1$, which reduces the number of possible arrangements to $\Omega_i = n\phi_i = n$. In a mixture of two components i and j the total volume is constrained by $\phi_i + \phi_j = 1$, which results in $\Omega_{i,j} = n(\phi_i + \phi_j) = n$. Therefore the mixing entropy ΔS_m for component i can be expressed as

$$\Delta S_{m,i} = k_B \ln \Omega_{i,j} - k_B \ln \Omega_i \tag{2.4}$$

$$= -k_B \ln \phi_i\,. \tag{2.5}$$

Since $0 < \phi_i < 1$, ΔS_m is always positive for a mixture consisting of small molecules. However, for polymers where a chain occupies multiple lattice sites, the definition of the mixing entropy has to be adjusted. In this case, the total number of occupied lattice sites n_i for a component i is defined as

$$n_i = \frac{n\phi_i}{N_i}\,, \tag{2.6}$$

where N_i is the number of lattice sites a given molecule of component i occupies, i.e., $N_i = 1$ for solvent molecules and $N_i > 1$ for a polymer chain. Finally, ΔS_m can be expressed as

$$\Delta S_m = -k_B(n_i \ln \phi_i + n_j \ln \phi_j)\,. \tag{2.7}$$

For ideal solutions ($\Delta H_m = 0$), ΔG_m is mainly dependent on the temperature T and the chain length of the polymer. In nonideal systems where $\Delta H_m \neq 0$, short-ranged inter- and intramolecular interactions need to be accounted for and are defined by the Flory–Huggins interaction parameter χ as [46,47]

$$\chi = \frac{z\Delta\epsilon}{k_B T}\,, \tag{2.8}$$

where z is the number of next neighbors in the lattice and the interchange energy $\Delta\epsilon$ accounts for the solvent-solvent contact energy ϵ_{ii}, the polymer-polymer contact energy ϵ_{jj} and the polymer-solvent contact energy ϵ_{ij} by $\Delta\epsilon = \epsilon_{ij} - 1/2(\epsilon_{ii} + \epsilon_{jj})$. For an interaction parameter $\chi = 0.5$, the solvent is considered to be a theta solvent and an ideal chain conformation is given. For $\chi > 0.5$ the solvent is referred to as a poor solvent in which the polymer tends to precipitate, whereas for $\chi < 0.5$ the solvent is a good solvent and the polymer is present as an expanded coil [51]. Using the definition of the interaction parameter χ from Equation 2.8, the mixing enthalpy ΔH_m is given as

$$\Delta H_m = n k_B T\, \chi\, \phi_i \phi_j\,, \tag{2.9}$$

and therefore – after normalization to the number of lattice sites n – ΔG_m can be expressed as

$$\Delta G_m = RT\left(\frac{\phi_i}{N_i}\ln\phi_i + \frac{\phi_j}{N_j}\ln\phi_j + \chi\phi_i\phi_j\right)\,, \tag{2.10}$$

where R is the ideal gas constant. It has to be noted, that Flory–Huggins theory is based on the assumptions that specific interactions between components such as clustering, excluded free volume, or fluctuations are neglected such that deviations for a real system have to be considered. Furthermore, for polymer solutions the solvation process is not only thermodynamically but also kinetically driven and therefore also limited by diffusion. Additionally, higher molecular weights or chain branching can also influence the solvation behavior [52].

2.2. Thermoresponsive Polymers

For polymer solutions where both ΔH_m and ΔS_m have an equal sign, the Gibbs free mixing enthalpy depends on the temperature of the system. If both terms are positive, ΔG_m will become negative at elevated temperatures, causing the system to change from being insoluble to being soluble at a specific temperature. This transition temperature is referred to as the upper critical solution temperature (UCST). In contrast, if ΔH_m and ΔS_m are both negative, ΔG_m becomes positive at elevated temperatures, such that the system goes from a soluble to an insoluble state at a certain transition temperature called the lower critical solution temperature (LCST) [46]. When the solubility of a polymer is temperature-dependent, this type of polymers is referred to as a thermoresponsive polymer. The transition temperature is defined as the point at which $\Delta G_m = 0$, resulting in an expression for the transition temperature as

$$T = \frac{\Delta H_m}{\Delta S_m} \,. \tag{2.11}$$

Therefore the transition temperature depends on the chemical and physical interactions between the solution and the polymer as well as on the molar mass of the polymer and its concentration. In Figure 2.2 the dependence of the Gibbs free mixing enthalpy ΔG_m on the polymer volume fraction ϕ_i and the temperature T is shown [47,53].

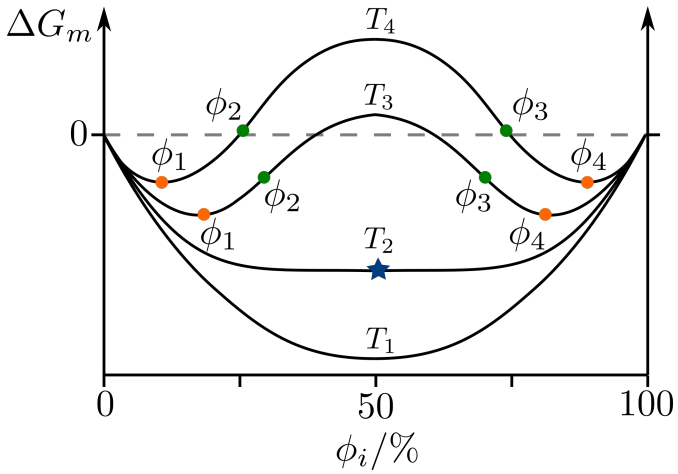

Figure 2.2.: Gibbs free energy as a function of the polymer volume fraction ϕ_i. T_1-T_4 represent curves at different temperatures, where minima are marked in orange and inflection points in green dots. The critical temperature is highlighted with a blue star [47].

For the temperatures T_1 and T_2, ΔG_m is always lower compared to the pure components, leading to the polymer being soluble at any volume fraction ϕ_i. The curve for T_2 represents the behavior just before the occurrence of a maximum at higher temperatures, and consequently T_2 is referred to as the critical or transition temperature. At elevated

temperatures as in the case of T_3 and T_4, the curves pass through minima at ϕ_1 and ϕ_4, where the system is soluble, which is also true for $\phi < \phi_1$ and for $\phi > \phi_4$. Consequently, at these temperatures the polymer is only soluble at certain volume fractions. Between the minima and the inflection point, i.e., between ϕ_1 and ϕ_2 as well as between ϕ_3 and ϕ_4, a metastable region is reached in which local concentration fluctuations determine whether or not phase separation occurs. The metastable region is unaffected by small fluctuations but larger fluctuations can cause the system to enter the unstable or stable region. Between the inflection points ϕ_2 and ϕ_3 an unstable region occurs at which phase separation takes place when ΔG_m becomes positive. Thus, phase separation of a solution occurs at a given temperature above the critical temperature for volume fractions ϕ_i between the minima at ϕ_1 and ϕ_4. For polymers featuring an UCST-type behavior the minima move closer together with increasing temperature thereby narrowing the unstable region. In contrast, polymers featuring a LCST-type behavior the minima move further apart at increasing temperatures. The temperature at which the minima at ϕ_1 and ϕ_4 coalesce describes the transition temperature. The curves depicting the miscibility gap in Figure 2.2 are further convertible into phase diagrams [47,54,55]. The phase diagrams of polymers in solution exhibiting an UCST-type or a LCST-type behavior are shown in Figure 2.3.

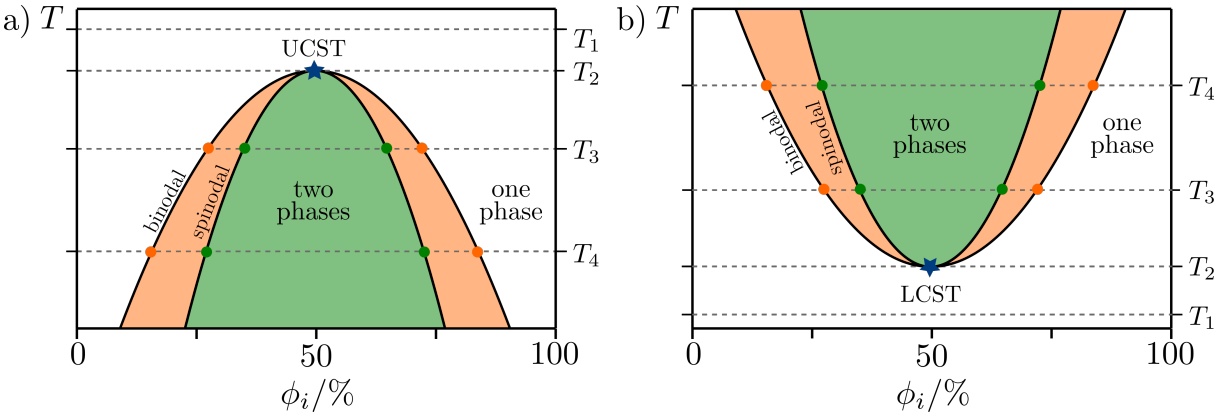

Figure 2.3.: Schematic phase diagrams of polymers in solution exhibiting an (a) UCST-type or a (b) LCST-type behavior. The phase diagrams consist of a one phase and a two phase region as well as of the binodal and spinodal curves [47,54,55]. In accordance with Figure 2.2, temperatures T_1–T_4 are indicated by dashed lines and characteristic points by colored circles and stars.

The binodal curve represents the points at which minima in ΔG_m occur, here, ϕ_1 and ϕ_4. The spinodal curve is determined by the inflection points, here, ϕ_2 and ϕ_3. Therefore, the region between the binodal and spinodal curves corresponds to the metastable region, which is colored in orange in Figure 2.3. Furthermore, the region highlighted in green in

Figure 2.3 enclosed by the spinodal curve corresponds to the unstable region where phase separation occurs. The region beyond the binodal curve is the one phase region at which the polymer is soluble.

As derived by Flory–Huggins theory, ΔS_m is highly dependent on the chain length of a polymer. Consequently, the chain length also influences the miscibility and the transition temperature of a polymer, which is then referred to as type I behavior. However, experimentally in certain cases only a slight dependence of the transition temperature on the chain length is observed, which is referred to as type II behavior [54,56,57].

2.2.1. Polymer-Solvent Interactions

As described in the previous section, the solubility of polymers mainly depends on the enthalpy term rather than on the entropy term. Thus, the interactions between the components have a major impact on the solubility as well as on the transition temperature of a thermoresponsive polymer. The solubility of a polymer in water is in general determined by its hydrophilicity. Polar functional groups at in the polymer chain are able to form hydrogen bonds and ionic or dipole interactions with the water molecules increasing the solubility. In contrast, hydrophobic parts of the polymer can only be hydrated according to the hydrophobic hydration, such that a solvation shell is formed. Therefore, the balance between hydrophilic and hydrophobic moieties determines the solubility of a polymer in water [57,58]. Solvents which are able to solvate polymers are referred to as good solvents, whereas solvents which do not dissolve the polymer are referred to as poor solvents. In regards of thermoresponsive polymers exhibiting a LCST, attractive forces between the solvent molecules and the polymer have to be favored at low temperatures compared to polymer-polymer interactions, and unfavored at higher temperatures [58]. At elevated temperatures the kinetic energy of the small solvent molecules dominates the thermodynamic energy gain of mixing, resulting in a coil-to-globule transition of the polymer and a phase separation [23,57]. At such temperatures, polymer-polymer interactions become more favorable compared to polymer-solvent interactions.

2.2.2. Cononsolvency

The cosolvency effect describes the phenomenon that a polymer becomes soluble in a mixture of two poor solvents. In contrast, if a polymer becomes insoluble in a mixture of two good solvents the effect is called cononsolvency. In the case of cononsolvency, the addition of a cosolvent can lead to a strong decrease of the transition temperature of LCST-type polymers. At high fractions of one or the other solvent, the polymer is miscible due to the

good solvent nature of the main solvent. At intermediate solvent fractions, however, the LCST passes through a minimum that can even be below room temperature. Thus, at a constant temperature the solubility of the polymer becomes dependent on the cosolvent concentration [3,9]. In this context, the most well studied system exhibiting cononsolvency behavior is poly(*N*-isopropylacrylamide) (PNIPAM) in water-methanol mixtures [59–67]. Additionally, PNIPAM exhibits cononsolvency behavior in aqueous solutions when mixed with ethanol [68–70], isopropanol [71], *n*-propanol [71,72], *N*,*N*-dimethylformamide (DMF) [59,73], tetrahydrofuran (THF) [22,74,75], 1,4-dioxane [22,74], acetonitrile [74], acetone [59,68,76], and dimethyl sulfoxide (DMSO) [59,74,76]. Beyond PNIPAM, another polymer demonstrating the cononsolvency effect is poly(*N*-isopropylmethacrylamide) (PNIPMAM), which is a structural analogon to PNIPAM only differing in an additional methyl group for each repeating unit at the polymer backbone. The chemical structures of PNIPAM and PNIPMAM are shown in Figure 2.4.

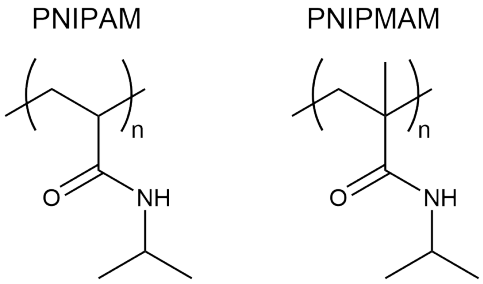

Figure 2.4.: Chemical structures of poly(*N*-isopropylacrylamide) (PNIPAM) and poly(*N*-isopropylmethacrylamide) (PNIPMAM).

Likewise as PNIPAM, PNIPMAM is also a thermoresponsive polymer with a LCST in aqueous solution at around 44 °C [37–41], which is considerably higher than the LCST of PNIPAM at 32 °C [57,77–80]. The elevated LCST of PNIPMAM compared to PNIPAM is explained by the sterically more hindered polymer backbone of PNIPMAM, which is weakening inter- and intrapolymer interactions [40,42–45]. To date fewer investigations on the cononsolvency effect of PNIPMAM have been conducted [81–86]. Nonetheless, PNIPMAM provides the unique opportunity to deduce trends in the cononsolvency behavior due to its similarity to the already well studied PNIPAM. Henschel et al. [86] investigated the cononsolvency effect based on the dependence of the cloud point of PNIPAM and PNIPMAM on the concentration of different cosolvents in aqueous solutions. In Figure 2.5 the cloud points of PNIPAM (hollow symbols) and PNIPMAM (solid symbols) are shown for lower alcohols (Figure 2.5a) as well as for aprotic polar cosolvents (Figure 2.5b). In general, two different patterns of the dependence of the cloud point on the cosolvent molar fraction in water is observed. Either the LCST transition passes through a minimum with increasing cosolvent fraction, which is the case for methanol

and acetone, or the LCST decreases continuously until it passes the melting point of the solvent mixture, which is the case for all alcohols besides methanol and for DMSO and DMF. Furthermore, it is observed that the decrease in the transition temperature is more pronounced for PNIPAM compared to PNIPMAM. Hence, the transition temperature is dependent on the hydrophobicity of the polymer and potentially also on the size of the excluded free volume. By decreasing the polarity of the alcohol, a lower cosolvent molar fraction is needed to induce a strong shift of the cloud point. In the case of polar aprotic cosolvents, acetone has a similar impact on the cloud point as methanol, whereas DMSO and DMF show similar behavior as longer-chained alcohols. Moreover, DMF seems to cause a slight increase in the cloud point at lower fractions before a decrease at higher fractions is obtained [86].

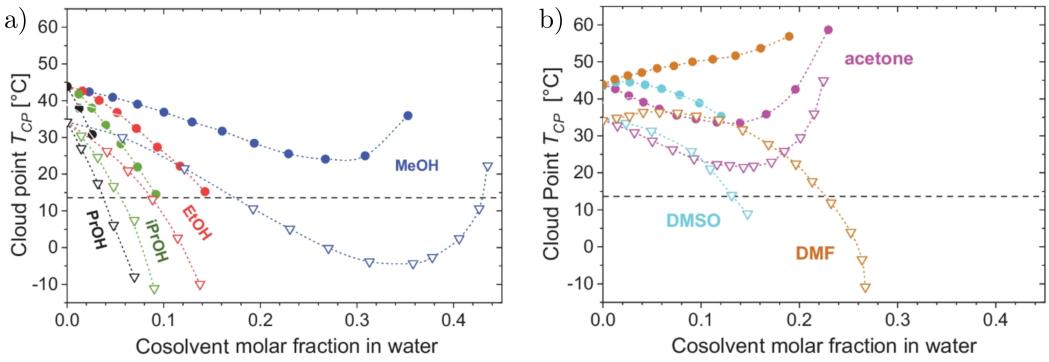

Figure 2.5.: Behavior of the cloud points of PNIPMAM (solid symbols) and PNIPAM (hollow symbols) in (a) mixtures of water and lower alcohols (methanol (MeOH, blue), ethanol (EtOH, red), isopropanol (*i*PrOH, green), and *n*-propanol (PrOH, black)) and (b) mixtures of water and dipolar aprotic solvents (DMSO (cyan), DMF (brown), and acetone (magenta)). The horizontal dashed line indicates the lower temperature limit of the experimental set-up used. Reprinted from Ref. [86], licensed under CC BY 4.0.

As aforementioned, until today the origin of the cononsolvency effect is not yet fully understood and many mechanisms were proposed to describe this intriguing phenomenon. It is unclear if the cononsolvency effect is governed by generic properties of the system, excluding specific interactions between the polymer and the solvents, or not. However, many theories were proposed which include specific interactions to be the origin for the cononsolvency effect. The explanations range from water-cosolvent complex formation over competitive binding to preferential adsorption, which are depicted in Figure 2.6. The explanation of Zhang et al. [87] relies on the formation of water-cosolvent clusters, which are more favorable than the individual interactions of the solvents with the polymer, causing the solvent mixture to become a poor solvent for the polymer and thus the polymer precipitates. In a related vain, Bischofberger et al. [88] defined the origin of the

cononsolvency effect based on a thermodynamic effect, where the addition of a cosolvent strengthens the hydrogen bonded water network, which in turn reduces the preference to hydrate the hydrophobic moieties of the polymer. In contrast, Tanaka et al. [60,89] hypothesized that the effect is driven by competitive binding of both solvents to the polymer, resulting in the precipitation of the polymer at higher cosolvent concentrations. Dalgicdir et al. [90] proposed that by the interaction of the cosolvent with the hydrophobic moieties of PNIPAM, the polar amide functional group is sterically hindered to form hydrogen bonds with water molecules, which in turn impacts the solubility of the polymer. Hao et al. [75] further proposed that concentration fluctuations in the close vicinity of the polymer – originating from the preferential adsorption of the organic solvent – are the reason for the cononsolvency effect. Similarly, Walter et al. [91] hypothesized that due to the preferential adsorption of the organic cosolvent by the polymer, the orientation of the nonpolar functional groups of the cosolvent face outwards, resulting in the formation of a hydrophobic surface which drives the coil-to-globule transition of the polymer. Contrarily, Heyda et al. [92] as well as Mukherji et al. [93] proposed that the preferential adsorption of the organic solvent causes bridging of neighboring segments, resulting in a phase separation of the system.

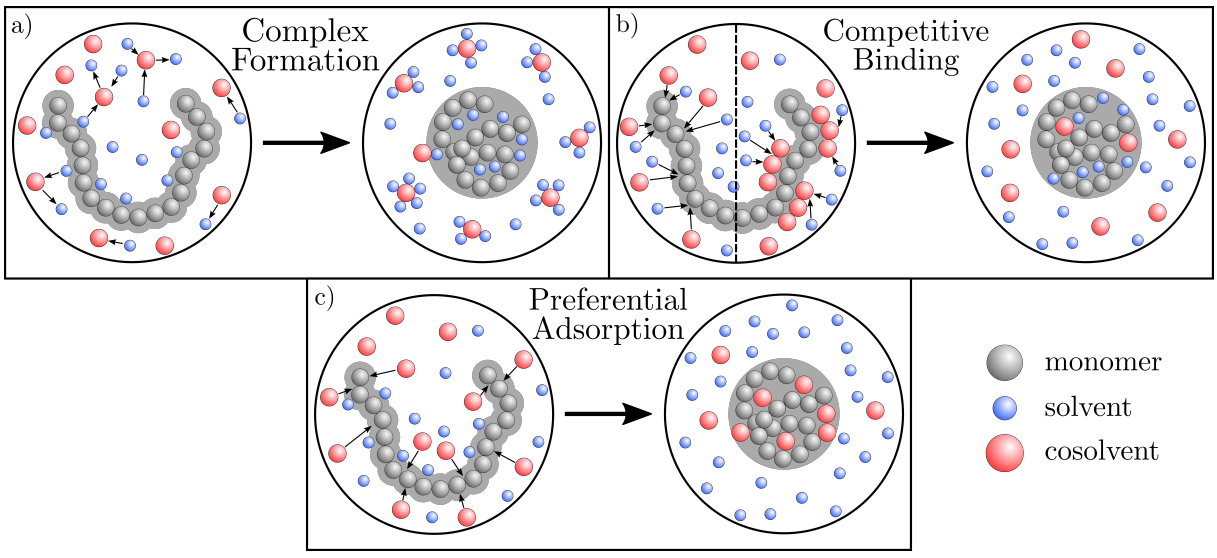

Figure 2.6.: Proposed mechanisms for the origin of the cononsolvency effect of polymers in solvent-cosolvent solutions. (a) Complex formation between solvent (blue) and cosolvent (red) molecules lead to a decrease in the overall solvation and thus to a coil-to-globule transition of the polymer. (b) Competitive binding of both solvent molecules to the functional groups of the polymer chain leading to desolvation of the polymer. Black dashed line separates the mechanism into the theories by Tanaka et al. [60,89] (left) and Dalgicidir et al. [90] (right). (c) Preferential adsorption of the cosolvent to the polymer changes the solvation shell of the polymer, causing it to collapse. Adapted from Ref. [3].

Evidently, even though many theories have been proposed, a theory accurately explaining the cononsolvency effect has yet to be developed. For each theory outlined above, arguments against were stated. However, it is apparent that in order to accurately describe the cononsolvency effect all possible interactions, i.e., polymer-solvent, polymer-cosolvent, and solvent-cosolvent need to be considered.

2.2.3. Specific Ion Effects

Upon solvation, salts undergo separation into the constituting ions and form solvent ion complexes due to their charged nature. Depending on the dielectric constant of the solvent, the ion concentration, and the charge density of the ions, ion association can occur where the electrostatic force is described by the Coulomb law according to

$$F = \frac{q_1 q_2}{4\pi\varepsilon r^2}\,, \tag{2.12}$$

where F is the Coulomb force, q_1 and q_2 are the individual electrical charges of the interacting ions, ε is the dielectric constant of the solvent, and r is the distance between the ions. In this regard, ion pairs are classified according to the structure of their solvation shells and their distance from each other as contact, solvent-shared, or solvent-separated ion pairs, which are depicted in Figure 2.7 [94].

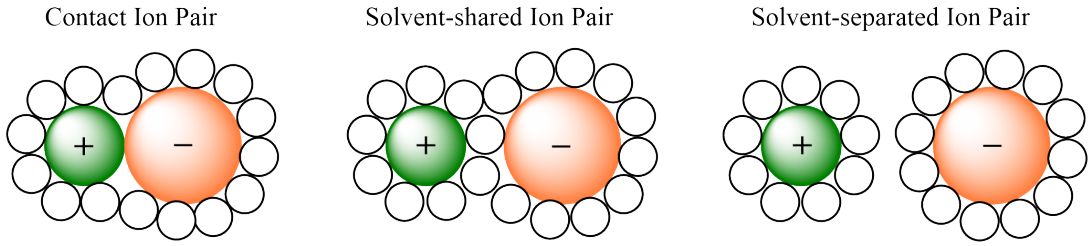

Figure 2.7.: Schematic depiction of contact, solvent-shared, and solvent-separated ion pairs. Solvent molecules are shown as black circles, cations as green and anions as orange spheres.

Contact ion pairs are ions which are directly in contact with each other without a separating solvation shell. For solvent-shared ion pairs, the ions share solvent molecules in their respective primary solvation shells, whereas solvent-separated ion pairs have disjunct primary solvation shells. Solvent molecules in the primary solvation shell are in direct contact with the ions and therefore form defined arrangements, whereas solvent molecules in secondary and higher solvation shells are increasingly less organized. In general, the formation of ion associates is determined by the Gibbs free energy, where the enthalpy term is dependent on the coulombic energy release by ion association opposed by the energy necessary for displacing a solvent molecule from the primary solvation shell.

Since the degree of disorder is reduced by the formation of ion pairs, the entropy term becomes negative. For higher concentrations of the solute the average distance between the ions decreases, which leads to a higher likeliness of the formation of ion associates [94].

Beyond the formation of solvation shells, ions in solution can affect the properties of additionally present components through hydrogen bonding, ion-dipole complex formation, and van der Waals interactions. If the influence of the ions is not only dependent on its charge or concentration but also on the identity of the ion itself, the phenomenon is referred to as a specific ion effect (SIE) [24,95]. A prominent example for one of the first reported SIEs is the Hofmeister series, in which the ability to solubalize a protein in the presence of ions is characterized dependent on the counterion introduced [25,26]. Therefore, the Hofmeister series distinguishes between anions and cations and groups them into kosmotropes and chaotropes. The anion series was found to be more dominant and is given by $CO_3^{2-} > SO_4^{2-} > S_2O_3^{2-} > H_2PO_4^- > F^- > Cl^- > Br^- \approx NO_3^- > I^- > ClO_4^- > SCN^-$ going from kosmotropic to chaotropic. For cations the series is likewise given by $Li^+ > K^+ \approx Na^+ > NH_4^+ > Mg^{2+}$. Hofmeister proposed that kosmotropes are strongly hydrated in water, resulting in an ordering of the solution and consequently in a salting-out of the protein, whereas chaotropes are weakly hydrated, disrupting the order of the solution as well as salting-in the protein. However, the ion–water adsorption model proposed by Hofmeister is controversial and the origin of SIEs is still under debate [24,95]. Another early attempt to characterize SIEs was reported by Pearson [96], which differentiates the ions according to their hardness and softness. Hardness is defined as ions having a high charge density, a low polarizability, and a small ionic radius, which is the opposite for softness. However, the Pearson concept is not universal and does in some cases predict, e.g., wrong solubilities [24]. It is noteworthy, that the series proposed by Hofmeister and Pearson, however, show – to a large extent – similarities, since the cation and anion order of Hofmeister resemble the trend based on the hardness concept. However, many studies show deviations from the Hofmeister series, which is explained by competing effects, different underlying mechanisms, the presence of cosolutes, the counterion identity, temperature variation, or changes of the pH or the ion concentration [24].

Today, specific ion effects are known to affect various systems such as solutions and surfaces on a wide range of properties including solution viscosity [97,98], surface tension [99], buffer [100,101], ion binding [102,103], micelle formation [104], enzyme activity [105–112], or the transition temperatures of thermoresponsive polymers [20,113–115]. Due to the variety of occurrences, many theories have been put forward to relate the origin of the SIEs to underlying physico-chemical properties such as ion polarizability,

size, shape, solubility, pKa, and ion association [24]. The theories for the influence of SIEs on polymer solutions account for the variety of possible interactions, i.e., ion–water (ion hydration), ion–polymer, ion–ion (ion pairing), polymer–water (polymer hydration), polymer–polymer (intra- and interchain interactions), and water–water (hydrogen bonding) interactions [23]. For the solubility of polymers in the presence of ions, the influence of the ions on hydrogen bond formation and stability are considered, i.e., the competition of hydrogen bond formation between the ion and the polymer, the influence on the hydrogen bond strength, and the influence of the hydration shell of the ion on the water structure. Large symmetrical ions exhibit a weak orientation-dependent binding due to their more delocalized and polarizable electron density, which makes them more easily desolvate and therefore increasingly interactive with the cosolute. In contrast, small ions with a high charge density allow for orientation-dependent binding. Multiple binding locations and anisotropic charge densities influence the ability of possible interactions. Charges located at the internal atom of a polyatomic ion can be shielded by the presence of outer site atoms, whereas charges located at outer sites increase the interaction strength towards neighboring species. Furthermore, the aforementioned properties can influence the likeliness of the presence of ions at vapor-liquid interfaces. In this regard, polarizable, charge diffuse ions can redistribute their hydration shell at the dynamic interface, while less polarizable, charge dense ions prefer to stay in the bulk region of the system [24,116]. Properties of polymers which rely on the formation and stability of hydrogen bonds, such as the phase transition temperature in thermoresponsive polymers can be greatly affected by the presence of ions. Thus, the chemical structure and surface properties of a polymer are correlated with the ion-polymer interactions and the hydration shell of the polymer, which indicates that SIEs are polymer-specific as well. Cremer et al. [20,21,117] investigated the influence of different sodium salts and their concentration on the LCST of PNIPAM in aqueous solution and – on a molecular level – proposed three distinct interaction mechanisms between the ions and the polymer. Figure 2.8 shows the three interaction mechanism, namely interactions through polarization, surface tension, and direct binding. The polarization mechanism describes the ability of strongly hydrated anions to polarize the water molecules that are hydrogen-bonded to the amide functional groups of PNIPAM. Thus, the resulting salting-out effect is governed by the dehydration of the hydrophilic amide groups. Additionally, anions can lower or raise the surface tension of the polymer-water interface by interfering with the hydrophobic hydration around the nonpolar functional groups leading to either a stabilization and a salting-in effect, or to a destabilization of the hydrated polymer and consequently to a salting-out effect. Weakly hydrated anions can interact directly with suitable binding sites of the polymer, which leads to a salting-in effect.

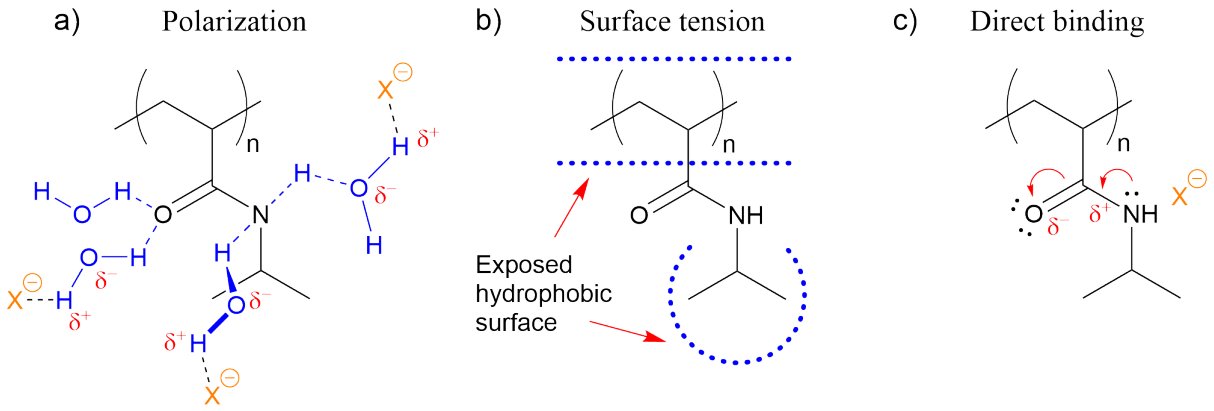

Figure 2.8.: Interactions of ions with the hydration shell and surface of PNIPAM. (a) Polarization effect of strongly hydrated anions on the hydration shell leading to a salting-out effect. (b) Surface tension effect created by the interference of strongly and weakly hydrated anions with the hydration shell surrounding the hydrophobic moieties leading to a salting-out effect. (c) Direct binding of weakly hydrated anions to the partially positively charged moieties on the polymer backbone leading to a salting-in effect. Adapted from Ref. [20].

Pegram and Record [118–122] hypothesized that the origin of the influence of salts on the coil-to-globule transition of polymers in solution stems from the affinity of ions towards different surfaces. As weakly hydrated anions prefer to accumulate at air-liquid interfaces, they are believed to also have a high affinity for hydrocarbon molecular surfaces leading to a salting-in effect. In contrast, strongly hydrated anions prefer to be excluded from interfaces. Cations are able to interact with electron rich functional groups, such as amide groups, which is why preferential accumulation/exclusion of individual ions at different surfaces occurs. The interplay between these phenomena determines the overall solubility and the ions are classified accordingly. Heyda et al. [113] conducted simulations of the dependence of the cloud-point of PNIPAM on the salt-concentration in aqueous solution. They proposed two different interaction mechanisms according to the type of ion. For strongly hydrated ions, the excluded-volume mechanism describes the repulsion from the polymer surface, which leads to an ion-depleted volume around the polymer. Therefore, the salting-in or -out effect is dependent on the change in the salt-accessible volume and the stabilization of the conformational state of the polymer. However, weakly hydrated ions prefer to directly interact with the polymer surface dependent on the conformational state of the polymer. At low salt concentrations weakly hydrated ions tend to interact with the coil state, rather than the globule state, and *vice versa* at high concentrations. Thus, the preferential absorption of the ions to either the coil or globule state of the polymer governs the salting-in or -out effect.

2.3. Polymers in Thin Film Geometry

While polymer systems in solution are quite well understood, as outlined in the preceding sections, their lack of mechanical stability limits practical applications. In contrast, bulk materials – while exhibiting increased mechanical stability – have reduced responsiveness to external stimuli, which hampers the ability to make use of their functionality. Combining the advantages of polymer solutions and bulk materials in terms of mechanical stability and fast response behavior, polymers in thin film geometry have emerged as a valuable class of sample architectures [8,30]. However, it has to be noted that due to the fixed geometry, the presence of interfaces, and the increased concentration of the polymer, several properties differ from polymer solutions. The solubility of polymers in solution can be compared to their swelling ability in thin film geometry, where the solvent molecules are taken up into a polymer-rich matrix. Practically, this can be achieved by immersing the polymer film in a solvent or by exposing the polymer thin film to a saturated solvent vapor atmosphere. Again the quality of the solvent in terms of its goodness determines the likeliness of it being incorporated into the film. Besides the still applicable Flory–Huggins theory described in Section 2.1, the swelling ability of polymer thin films is determined by the Flory–Huggins interaction parameter χ and the diffusion rate. The diffusion process is dependent on the diffusion of the solvent molecules into the polymer matrix as well as on the conformational change of the polymer chains. Starting from a dry polymer thin film, the solvent molecules have to initially penetrate into the polymer matrix, thereby filling up empty voids and the excluded free volume between polymer chains. The hydration of the polymer chains and the further uptake of solvent molecules then leads to a reorientation of the polymer chains and to an expansion of the film. For chemically cross-linked polymers, Flory–Rehner theory [123] describes the dependence of the total free enthalpy ΔG on the free enthalpy of mixing ΔG_m and the free enthalpy of elastic deformation ΔG_{el} as

$$\Delta G = \Delta G_m + \Delta G_{el}\,. \tag{2.13}$$

By differentiation with the number of moles of the solvent, the above expression can be expressed in terms of the chemical potential $\Delta\mu$ as

$$\Delta\mu_1 = \Delta\mu_{1,m} + \Delta\mu_{1,el}\,, \tag{2.14}$$

where $\Delta\mu_1$ is defined as $\mu_1 - \mu_1^0$ and μ_1 is the chemical potential of the solvent inside and μ_1^0 the chemical potential outside of the polymer matrix. Since the chemical potential is dependent on the osmotic pressure Π, the equation can further be reformulated into

$$\Pi_{sw} = \Pi_m + \Pi_{el}\,, \tag{2.15}$$

where Π_{sw} is the swelling pressure, Π_m is the osmotic pressure, and Π_{el} is the elastic response of the polymer. At an equilibrated swollen state, the swelling pressure becomes zero, which in turn means that the difference in chemical potentials of the solvent, i.e., inside and outside the polymer matrix, is zero.

Similar to chemically cross-linked polymers, linear polymers are also able to incorporate solvent molecules without going into solution by the help of physical interactions, which stabilize the polymer network. However, physical crosslinks such as hydrogen bonding, coordination bonding, ionic interactions, hydrophobic interactions, dipole-dipole interactions, van der Waals interactions, or chain entanglements are weak and dynamic [124]. In contrast to chemical crosslinks, which have defined junctions, physical crosslinks can rearrange and thereby release strain from the expanding polymer chains.

2.3.1. Volume Phase Transition

Upon an external stimulus a polymer network previously swollen in the presence of a solvent can exhibit a volume phase transition, which can be related to the coil-to-globule transition of polymers in solution. The volume phase transition is defined as a discontinuous change in the degree of swelling, enabling the possibility of the existence of two distinct states with different swelling degrees [29]. The response of the polymer gel to an external stimulus causes the polymer chains to collapse and to expel the solvent, resulting in a deswollen, contracted state. This process can be reversible to some extent, meaning that the polymer gel can be restored to its original swollen state. In biomedical applications this behavior is leveraged in fields such as tissue engineering [125] or controlled drug release [10,31,126] as well as in other applications such as actuators [33,127], nanoswitches [83], sensors [128], or soft robotics [129]. In the realm of thermoresponsive polymers such as PNIPMAM, a volume phase transition can be induced by changing the temperature over the volume phase transition temperature (VPTT) or by leveraging the cononsolvency effect by introducing a mixture of water and an organic cosolvent in a certain ratio. In Figure 2.9 the solvent uptake and release behavior of a polymer thin film on a substrate is schematically depicted. In general, polymer thin films are geometrically restricted on a substrate. Thus, the volume expansion during a swelling process and the contraction upon an external stimulus is mainly along the surface normal. Therefore, measurement techniques, which are able to measure the thickness of a polymer film on a substrate are suitable to investigate the volume phase transition upon different external

stimuli. Through time-resolved experiments the dynamic of the swelling and contraction behavior of the films can further be determined and studied.

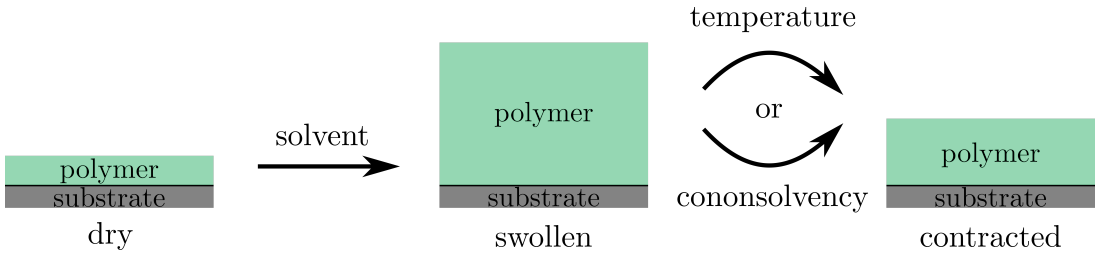

Figure 2.9.: Schematic representation of a polymer thin film on a supporting substrate going from a dry to swollen state by the addition of a solvent, followed by a contraction induced by temperature or cononsolvency.

2.4. Basic Concepts of Specular Reflectivity

The characterization of thin film samples on supporting substrates in terms of the film thickness, interface roughness, and optical constants can be probed by various techniques which measure the specular reflection. When electromagnetic waves or neutrons pass from one medium to another, reflection and scattering (including diffuse scattering) can occur, depending on the properties of the materials and the nature of the interaction. The latter is described by the law of reflection, which states that the angle of reflection is equal to the angle of incidence. For an elastic scattering process, the energy of the incident wave and thus the wavelength is conserved in the reflected wave. In Figure 2.10 possible scattering phenomena from a surface are illustrated.

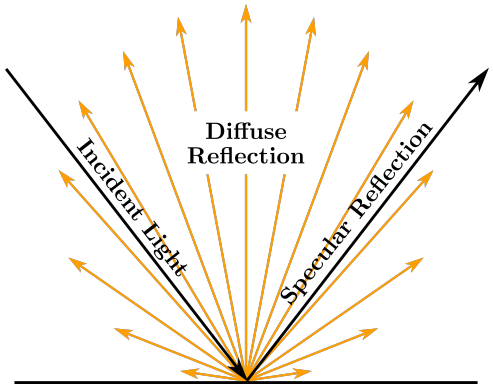

Figure 2.10.: Illustration of diffuse scattering (orange) and specular reflection (black) from a surface. The lengths of the vectors for the diffusely scattered light are according to Lambert's cosine law [130].

For diffuse scattering, the angular distribution of the radiant (reflected) intensity can be described according to Lambert's cosine law as

$$I = I_0 \cos(\theta)\,, \tag{2.16}$$

where I is the radiant intensity, I_0 is the maximum intensity obtained along the surface normal and θ is the angle between the direction of radiation and the surface normal. This law states that for an ideal diffusely reflecting surface the intensity is directly proportional to the cosine of the angle between the detector and the surface normal [130].

2.4.1. Reflection from an Ideal Surface

In general, according to the wave-particle dualism, a quantum mechanical particle can also be described by a wave. An incident wave described by wave function ψ_i can either be scattered diffusely or in specular reflection at a homogeneous interface between two heterogeneous media. In contrast to diffuse scattering, for specular reflection the reflected angle θ_r and the incident angle θ_i are identical. Furthermore, dependent on the angle of incidence the wave can be split into a reflected (ψ_r) and a transmitted (refracted) part (ψ_t), which is shown in Figure 2.11 [131–133].

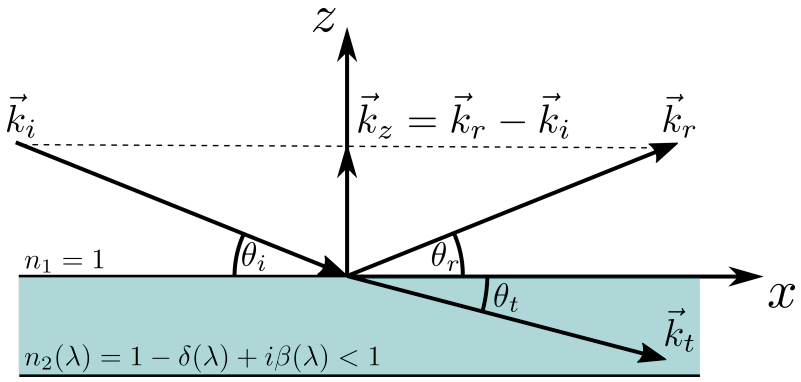

Figure 2.11.: Reflectance and transmittance of incident waves at an ideal interface between two heterogenouse media with refractive indices $n_1 = 1$ and $n_2 < 1$. The incident wave is characterized by the wave vector $\vec{k_i}$ at an incident angle θ_i. Likewise the reflected and transmitted waves are characterized by $\vec{k_r}$, θ_r and $\vec{k_t}$, θ_t, respectively [131–134].

The wave functions $\psi(\vec{r})$ of the incident (i), reflected (r), and transmitted (t) waves are hereby given as

$$\psi_i(\vec{r}) = a_i \exp(i\vec{k_i} \cdot \vec{r}) \,, \tag{2.17}$$

$$\psi_r(\vec{r}) = a_r \exp(i\vec{k_r} \cdot \vec{r}) \,, \tag{2.18}$$

$$\psi_t(\vec{r}) = a_t \exp(i\vec{k_t} \cdot \vec{r}) \,, \tag{2.19}$$

where a_n are the amplitudes, $\vec{r}$ is the position, and $\vec{k_n}$ are the corresponding wave vectors. The wave vector describes the direction of propagation of the wave and is oriented perpendicular to the wave front, while the magnitude is inversely proportional to the wavelength λ. The relationship between the orientations of the incident and the transmitted waves is described by Snell's law given as [132,133,135]

$$\frac{\sin(\theta_i)}{\sin(\theta_t)} = \frac{n_2}{n_1} \,, \tag{2.20}$$

where θ_i and θ_t are the angles of incidence and transmittance and n_1, n_2 are the refractive indices of the respective media. The largest angle for which refraction still occurs is known as the critical angle θ_c, which is described by Snell's law as

$$\sin(\theta_c) = \frac{n_2}{n_1} \qquad \text{with} \quad n_2 < n_1 \,. \tag{2.21}$$

Consequently, in the case of $n_2 < n_1$, incident angles smaller than the critical angle lead to total external reflection. While at the critical angle the reflected wave travels along the surface as an evanescent wave, for angles larger than the critical angle refraction occurs [134]. The described scattering processes are shown in Figure 2.12, where the relationship between the orientations of the incident and the transmitted waves according to Snell's law is depicted.

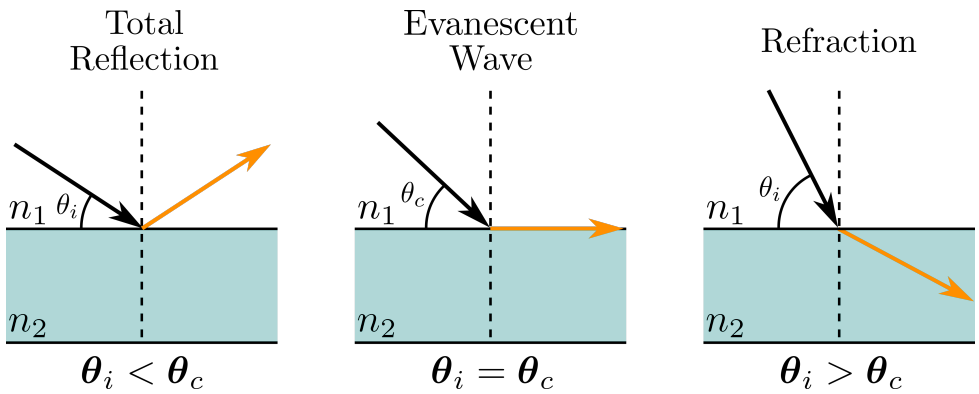

Figure 2.12.: The relationship between the orientations of the incident and the transmitted waves according to Snell's law. For $\theta_i < \theta_c$ total external reflection occurs, at $\theta_i = \theta_c$ the wave propagates along the surface, and for $\theta_i > \theta_c$ refraction occurs.

For X-rays and neutrons the refractive index of a medium is a complex quantity given by [132,133,136–139]

$$n(\lambda) = 1 - \delta(\lambda) + i\beta(\lambda)\,, \tag{2.22}$$

$$\delta_{\text{xray}}(\lambda) = \frac{\lambda^2}{2\pi} r_e \rho_e\,, \quad \delta_{\text{neutron}}(\lambda) = \frac{\lambda^2}{2\pi} N b\,, \tag{2.23}$$

$$\beta_{\text{xray}}(\lambda) = \frac{\lambda}{4\pi}\mu\,, \qquad \beta_{\text{neutron}}(\lambda) = \frac{\lambda}{4\pi} N \alpha_a\,, \tag{2.24}$$

where r_e is the Thompson scattering length of the electron (classical electron radius), ρ_e is the electron density, N is the number of atoms per unit volume, b is the coherent scattering length, μ is the linear absorption coefficient, and α_a is the cross section for absorption of neutrons. The refractive index is therefore dependent on the dispersion coefficient δ and the complex absorption coefficient β. Since typically the values for δ and β are small on the order of 10^{-6} for X-rays and neutrons, these effects can be neglected and the refractive index is $n \lesssim 1$, which means that air/vacuum is optically more dense than matter resulting in a higher phase velocity in matter for X-rays and neutrons [132,138,140].

The terms $r_e\rho_e$ for X-rays and Nb for neutrons are known as the scattering length density (SLD) which describes the scattering power of a material [133,139]. Since X-rays scatter at the electron shells, the SLD is dependent on the electron density ρ_e. In contrast, neutrons are scattered at the nuclei and the scattering power is dependent on the nuclear scattering lengths b, which itself depends on the specific neutron-nucleus interactions including spin-coupling and magnetic interactions and are therefore isotope-dependent. From the chemical composition of a material the SLD can be calculated as [131,133]

$$SLD = \frac{\sum_i n_i b_i}{V_m} \qquad \text{with} \qquad V_m = \frac{M}{\rho_{\text{bulk}} N_A}\,. \tag{2.25}$$

The SLD can be expressed by summing up the scattering length contributions b_i times the number of individual atoms n_i of a species i divided by the molecular volume V_m of the compound. The molecular volume consists of the molar mass M, the density of the material in bulk ρ_{bulk}, and Avogadro's number N_A. Since the SLD is directly connected to the refractive index, a large difference in SLD values of two materials leads to a higher contrast between the individual components. A higher contrast is important for distinguishing the presence of different materials [134]. Since the scattering ability of X-rays is dependent on the electron density of a given atom, high contrast can be achieved between elements with significantly different atomic numbers. In contrast, in neutron experiments the SLDs of the elements vary randomly but differs between isotopes [136,141,142]. For example, for ^{1}H and ^{2}H the neutron scattering lengths differ greatly, which allows to use

deuteration as a contrast variation method in neutron experiments, e.g., a protonated polymer in D_2O. While a strong difference in the coherent neutron SLDs between ^1H and ^2H achieves a high contrast, it has to be noted that in experiments with ^1H containing materials strong incoherent scattering contributions of ^1H lead to an attenuation of the neutron beam and to a larger background contribution [133,135,136,139].

After having established the condition for refraction and the dependence of the SLD on the refractive index, the intensity of the reflected and transmitted waves remains to be determined. Based on Equations 2.17–2.19, the reflectivity R is defined as the absolute square of the amplitude a_r and hence the reflectivity is the ratio of reflected and incident intensity. The respective coefficients for the polarization components perpendicular (r_s, t_s) and parallel (r_p, t_p) to the plane of incidence are expressed by the Fresnel equations as [135,140,141]

$$r_s = \frac{n_1 \sin(\theta_i) - n_2 \sin(\theta_t)}{n_1 \sin(\theta_i) + n_2 \sin(\theta_t)}\,, \tag{2.26}$$

$$t_s = \frac{2n_1 \sin(\theta_i)}{n_1 \sin(\theta_i) + n_2 \sin(\theta_t)}\,, \tag{2.27}$$

$$r_p = \frac{n_2 \sin(\theta_i) - n_1 \sin(\theta_t)}{n_2 \sin(\theta_i) + n_1 \sin(\theta_t)}\,, \tag{2.28}$$

$$t_p = \frac{2n_1 \sin(\theta_i)}{n_2 \sin(\theta_i) + n_1 \sin(\theta_t)}\,. \tag{2.29}$$

The total amplitude a_r consists of the average of the r_s and r_p contributions. As stated above, for angles below the critical angle θ_c, only total external reflection occurs and the reflectivity is 1. Consequently, for angles larger than the critical angle ($\theta_i > \theta_c$), refraction occurs and therefore a reduction of the reflectivity is observed. In the asymptotic limit for large angles of incidence, the reflectivity reduces to

$$R_F \approx \left(\frac{2\theta_i}{\theta_c}\right)^{-4}\,, \tag{2.30}$$

meaning that the behavior of the reflectivity for very large angles relative to the critical angle is governed by a θ_i^{-4} decay. Therefore reflectivity measurements close to the critical angle offer enhanced intensity and are suitable for detection. Under ideal conditions the above discussed reflectivity R_F is also known as the Fresnel reflectivity [133,140,141,143].

Another way to express the reflectivity is as a function of the scattering transfer vector $\vec{q}$ defined as $\vec{k}_i - \vec{k}_r$. In the case of specular reflection where the incident and the reflected angles are equal, $\vec{q}$ is oriented normal to the surface, i.e., q_z or $\vec{k}_z$ as shown in Figure 2.11. Since the direction of $\vec{q}$ determines the direction of structural information gain, specular reflection provides information vertically through the medium. The momentum transfer vector $\vec{q}$ is defined as

$$\vec{q} = q_z = \frac{4\pi}{\lambda} \sin(\theta_i) \,, \tag{2.31}$$

and is mainly dependent on the wavelength λ and the incident angle θ_i [132,135,140].

2.4.2. Reflection from a Nonideal Surface

In real systems rough surfaces and buried interfaces of multilayer systems cause deviations from the ideal behavior. In addition to specular reflection, nonspecular (diffuse) scattering contributions, caused by surface or interfacial roughness, lead to a reduction of the reflectivity. The resulting reflectivity can be described by the Fresnel reflectivity R_F from Equation 2.30 multiplied with a correction term, e.g., such as a Debye–Waller-type correction [131,134,135,138] yielding

$$R(q_z) = \left(\frac{2q_z}{q_c}\right)^{-4} \left| \int \rho'(z) \exp(iq_z z) dz \right|^2 \,, \tag{2.32}$$

where – in the case of XRR – $\rho'(z)$ describes the average value of the electron density profile normal to the interface. Likewise, for NR $\rho'(z)$ describes the profile of the scattering length. Consequently, this links the description of roughness directly to the SLD and therefore also to the refractive index. In general, $\rho'(z)$ is not experimentally observable, thus the roughness is expressed by assuming a Gaussian profile of the interface, as visually motivated in Figure 2.13, as

$$\rho'(z) = \frac{1}{\sqrt{2\pi w^2}} \exp\left(-\frac{z^2}{2w^2}\right) \,, \tag{2.33}$$

where w^2 is the mean square interface width. By Fourier transformation of the above expression, it can be shown, that the reflectivity is decreasing with an increasing scattering vector q_z [132,133,135,140,141,143].

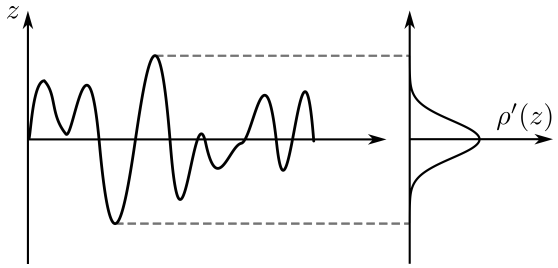

Figure 2.13.: Contour line profile of a rough interface with the resulting Gaussian distribution of the density gradient $\rho'(z)$ [132,133,135,140,141,143].

2.4.3. Multilayer Systems

To account for multiple interfaces in layered systems the individual scattering contributions of each layer have to be considered. In the optical formalism approach, the reflectivity of a multilayer system can be described by the sum of the reflection coefficients at each interface, each described by the Fresnel equations 2.26. This approach is only suitable for interfaces with negligible diffuse scattering, since diffuse scattering contributions are ignored. However, in some nonideal systems the fraction of diffuse scattering originating from rough interfaces can be accounted for by a Debye–Waller-type correction as shown in Equation 2.32. Note that the Debye–Waller-type correction does not apply to interfaces with too much roughness. In the presence of a second interface, as exemplarily shown in Figure 2.14, elastic reflection from both interfaces leads to a superposition of the reflected waves by either constructive or destructive interference [132,137,138,140].

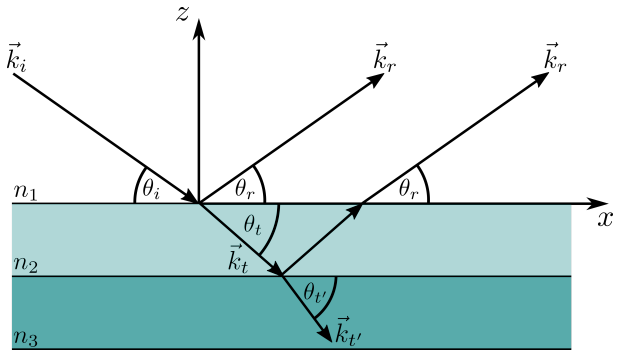

Figure 2.14.: Reflectance and transmittance of incident waves at the interfaces of a multilayer system with refractive indices n_1, n_2, and n_3. The incident wave is characterized by the wave vector $\vec{k_i}$ at an incident angle θ_i. Likewise the reflected and transmitted waves are characterized by $\vec{k_r}$, θ_r and $\vec{k_t}$, θ_t, respectively [132,137,138,140].

For a multilayer system, the interference of the reflected waves depends on the difference of the optical paths determined by the layer thickness d and the incident angle θ_i. The conditions for constructive and destructive interference are given as

$$2nd\sin(\theta_i) = m\lambda\,, \tag{2.34}$$

$$2nd\sin(\theta_i) = (m + 1/2)\lambda\,, \tag{2.35}$$

respectively, where m is an integer value. Thus, the reflection pattern is dominated by a periodic evolution of the reflectivity with the incident angle θ_i. These modulations are known as Kiessig fringes and their spacing Δq is given by

$$\Delta q = \frac{2\pi n_j}{d_j}\,. \tag{2.36}$$

According to the above equation, the spacing between the fringes gives information about the layer thickness d_j of a given layer j. Other parameters influencing the shape of the reflectivity pattern include the density difference between two layers. The amplitude of the oscillations is dependent on the magnitude of the density difference and the relative phase is dependent on the sign of said density difference. Furthermore, the critical edge at q_c, i.e., the q_z value at the critical angle θ_c, is determined by the SLD and therefore by the refractive index n. On top of that, rough surfaces and buried interfaces lead to a damping in the interference fringes at large q_z. In Figure 2.15 the influence of the thickness, the SLD, and the roughness for a single polymer layer on top of a silicon substrate with its native SiO_2 layer is shown.

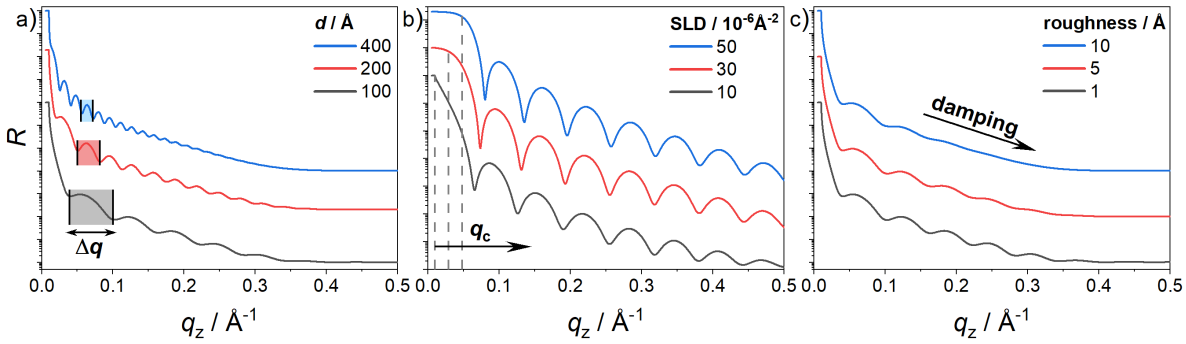

Figure 2.15.: Exemplary neutron reflectivity curves for varying parameters. (a) Thickness d variation influencing the fringe spacing. (b) SLD variation influencing the position of the critical edge. (c) Roughness variation causing damping at higher q_z values.

2.4.4. Data Evaluation

Reflectivity patterns are usually evaluated by using models to fit the measured data. However, a given data set can in principle be fit by an infinite number of models [140]. Therefore, it is emphasized to construct a model close to the real system with care and to keep the number of adjustable parameters limited. Most commonly, Parrat's multilayer model approach [144] is used to describe a reflectivity curve based on known physical properties influencing the scattering ability of each layer. The model is built recursively from the bottom up and assumes the bottom layer to be an infinitely thick substrate. The reflection coefficient of the j-th layer is calculated from the $j-1$-th layer according to the optical Fresnel formalism. Therefore, each layer is characterized by its thickness, SLD or refractive index, and roughness. The latter can be accounted for by a correction factor as described in the preceding section. Once an appropriate model has been chosen, it is fit to the N_{exp} experimental data points R_{exp} by minimization of the mean square error $\chi^2 = 1/N_{\mathrm{exp}} \sum (R_{\mathrm{exp}} - R_{\mathrm{calc}})^2/\sigma^2$ by means of least squares fits. Here, σ is the experimental uncertainty of the measured reflectivity. Due to the complex structure of the fit function a well-chosen initial guess is important to converge to an appropriate minimum. To enhance the probability of converging to the global minimum, global optimization algorithms such as differential evolution can be used [145].

To describe the reflectivity curve of a polymer film on top of a silicon substrate, as shown in Figure 2.16, a model consisting of at least a semi-infinite front and backing medium, i.e., substrate and air, with fixed SLDs and the polymer film itself has to be applied. This model is typically referred to as one-layer model.

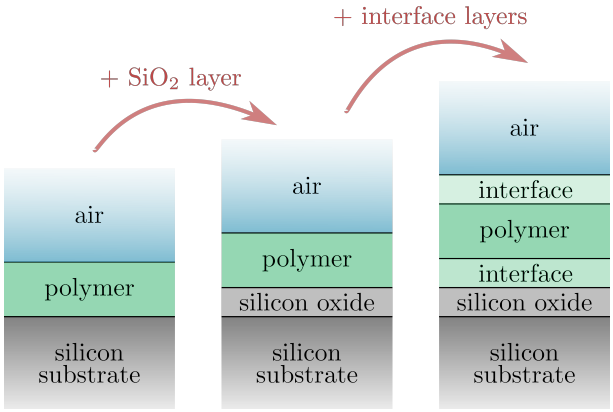

Figure 2.16.: Different models for the reflectivity pattern of a polymer film on a Si substrate. The simplest model includes only the polymer film between semi-infinite Si substrate and air layers (left). To account for oxidation of the substrate a silicon oxide layer can be added (center). To describe deviations for the polymer bulk interface layers can be included (right).

Due to oxidation processes silicon bares a native silicon oxide layer, which also has to be accounted for in the model. Furthermore, deviations from polymer bulk properties may occur at the interfaces towards either the substrate or the surrounding environment. The differing nature of the behavior of the polymer at an interface is commonly described by adding an additional interface layer. Interface layers might also be needed in case of depletion or accumulation of material at the interfaces. Thereby, information about the distribution of material vertically through the film is obtained from the fits.

3. Characterization Methods

To enable the investigation of the response behavior of PNIPMAM thin films towards different vapor atmospheres in the presence of salts, different characterization methods are selected. To follow the macroscopic change and the interactions on a molecular level, *in situ* measurement methods are utilized. Additionally, the combination of X-ray and neutron measurements is exploited to obtain a comprehensive understanding of the film composition. In the following sections each measurement technique is introduced and the measurement principle of the instrument is explained.

3.1. Spectral Reflectance

Spectral reflectance (SR) is a non-destructive measurement technique to determine the thickness and refractive index of a single or multilayer film on a reflective substrate. Light in the visible range with multiple wavelengths is directed onto the sample at normal incidence, i.e., $\theta_i = 90°$. In Figure 3.1 the described measurement configuration for a polymer film on a substrate is shown.

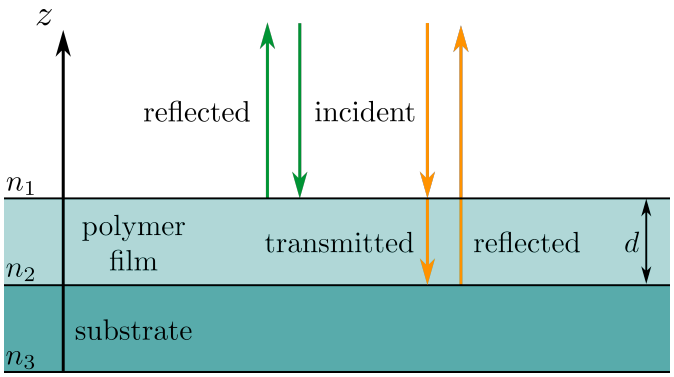

Figure 3.1.: Measurement principle of spectral reflectance at normal incidence for a polymer film with thickness d on a substrate. The incident light is either reflected at the air-polymer interface (green) or at the polymer-substrate interface (orange).

Due to the light impinging normal onto the sample, a phase shift of 180° occurs at each interface since $n_3 > n_2 > n_1$. Thus, the conditions for constructive or destructive interference from Equations 2.34 and 2.35 simplify to

$$2nd = m\lambda\,, \tag{3.1}$$

$$2nd = (m + 1/2)\lambda\,. \tag{3.2}$$

Hence, interference only depends on the thickness d and the refractive index n of the polymer. Furthermore, the Fresnel reflection coefficients r_s and r_p given in Equations 2.26 can be reformulated to

$$r_s = \frac{n_1 - n_2}{n_1 + n_2}\,, \tag{3.3}$$

$$r_p = \frac{n_2 - n_1}{n_1 + n_2}\,. \tag{3.4}$$

For spectral light the definition of the refractive index n changes in comparison to the definition given in Section 2.4 due to the different wavelength range of the photons. The refractive index n is still a complex quantity consisting of the real refractive index n_0 and the extinction or absorption coefficient κ as

$$n = n_0 + i\kappa\,. \tag{3.5}$$

The consequence of the complex nature of the refractive index can be understood by inserting Equation 3.5 into the wave function of the reflected wave given in Equation 2.18, simplified for normal incidence. Separation of the real and the imaginary parts yields

$$\begin{aligned}
\psi_r(z) &= a_r \exp(ik_r z)\,, && \text{with} \quad k_r = \frac{2\pi}{\lambda_0} n \\
&= a_r \exp\left(i\frac{2\pi}{\lambda_0} n z\right)\,, && \text{with} \quad n \;= n_0 + i\kappa \\
&= a_r \exp\left(i\frac{2\pi}{\lambda_0} n_0 z\right) \exp\left(-\frac{2\pi}{\lambda_0}\kappa z\right)\,,
\end{aligned} \tag{3.6}$$

where λ_0 is the vacuum wavelength. Since the complex exponential can be expressed according to the Euler identity, n_0 defines the oscillations of the reflectivity. Contrary, the presence of the extinction coefficient κ in the decaying exponential leads to an exponential reduction of the reflectivity.

In the special case of a thin layer on a substrate and an incident angle of $\theta_i = 90°$, the reflectance consists only of the perpendicular component r_s and can be expressed as

$$R = \left|\frac{r_1 + r_2 \exp(-i\beta)}{1 + r_1 r_2 \exp(-i\beta)}\right|^2 \quad \text{with} \quad \beta = \frac{4\pi n_2 d}{\lambda}\,. \tag{3.7}$$

Based on the above equation, the dependence of the reflectance curve on the polymer thickness d with varying wavelengths λ is exemplarily shown in Figure 3.2.

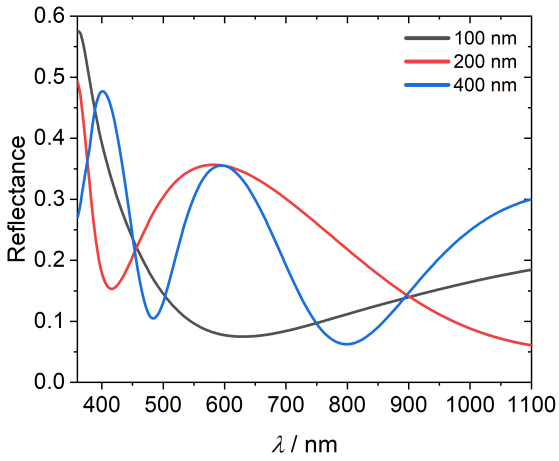

Figure 3.2.: Dependence of the reflectance curve on the polymer thickness d with varying wavelengths λ.

Measurement Principle SR measurements are conducted by focusing white light perpendicular onto a thin film sample and detecting the reflected light. A schematic illustration of a SR measurement setup is shown in Figure 3.3.

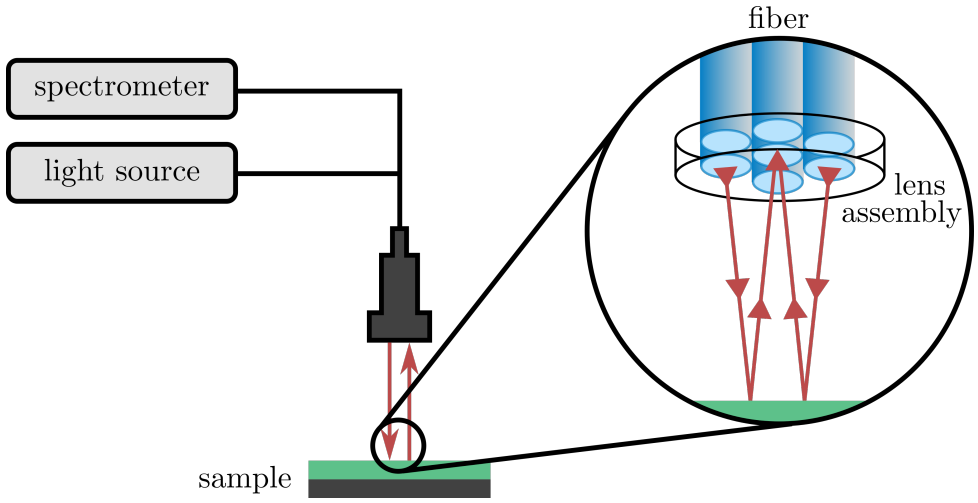

Figure 3.3.: Schematic illustration of the SR measurement setup and detailed depiction of the optical fiber channels. White light coming from the light source is focused perpendicular onto the sample. The reflected light is then guided through the optical fiber and is analyzed by the spectrometer.

The setup consists of a light source, an optical fiber, and a spectrometer. The optical fiber serves two purposes: 1) It carries the light from the source and illuminates the sample and 2) it carries the reflected light to the spectrometer. This is realized by different channels consisting of individual fibers as shown in Figure 3.3. The reflected light can be separated into the individual wavelengths by either a prism or by channels specific for only a subset of wavelengths before being detected.

Instrument SR measurements are performed by the use of a Filmetrics F20 Thin Film Measurement System (Filmetrics Inc., KLA, San Diego, USA), consisting of a Filmetrics F20-UV Thin Film Analyzer, optical fibers, and a light source (halogen lamp 360-1100 nm, deuterium lamp 180-1100 nm). The light from the preheated light source is focused onto the sample with a diameter of roughly 2 mm from a distance of 10 cm from the sample to the lens assembly on the lid of the neutron chamber described in Section 4.1.1 and shown in Figure 4.2. After the light passes through a CaF_2 window – subsequently being reflected by the sample – the reflected light is analyzed by using the robust thickness fit algorithm within the FILMeasure software. Prior to a measurement the intensity of the raw signal, measured on a bare silicon wafer is maximized by normal alignment of the light path to the sample surface as well as by adjusting the vertical distance between the sample and the light source. Additionally, to account for substrate and background contributions, a spectrum of a bare silicon wafer and of an absorber are taken and subtracted from the spectrum of the sample. To determine the film thickness from a recorded reflectance spectrum, a user supplied initial guess of the film thickness is varied within a given range by the fit algorithm until high fidelity is reached. For the fit procedure a multilayer model consisting of a silicon substrate, a SiO_2 layer, a polymer layer, and air is applied. For the *in situ* measurements the spectra are recorded every 10 s to monitor the thickness evolution of the thin films.

3.2. X-Ray Reflectivity

X-ray reflectivity (XRR) is a surface sensitive, non-invasive measurement technique used to study thin films, multilayer systems, and buried interfaces. XRR is thereby able to characterize films in the region from ≈1 nm to several hundred nanometers. XRR measured at small angles, for which the underlying theory is described in Section 2.4, yields the thickness, the SLD, and the roughness of individual layers by applying a model on the experimental reflectivity data. Typically copper is used as a metal target, which produces characteristic radiation known as Cu Kα (λ = 1.5418 Å) and Cu Kβ (λ = 1.39223 Å), depending on the originating shell of the relaxing electron. Due to spin-orbit coupling,

the Cu Kα line is in principle separated into Cu $K\alpha_1$ ($\lambda = 1.54059$ Å) and Cu $K\alpha_2$ ($\lambda = 1.54443$ Å), causing a doublet emission line which, however, may not be resolvable by the instrument [146]. Unwanted lines can in general be filtered out by absorbing metals or monochromators. Due to the electromagnetic wave nature of X-rays, the photons are scattered at the electron shell of an atom. Therefore the scattering ability is proportional to the electron density and consequently follows a trend along the periodic system of elements. According to Equation 2.22, this changes the refractive index and therefore also the SLD. Hence this describes the origin of contrast in X-ray experiments, if two materials exhibit a difference in electron density. Due to the monochromatic nature of X-ray photons used in practical applications, the incident angle has to be varied in order to obtain reflectivities in a varying q_z-range according to Equation 2.31.

Measurement Principle In practice there are different measurement setups to measure XRR, such as the Bragg-Brentano or the parallel beam geometry [147]. In the parallel beam geometry a collimating optic is used to generate a parallel X-ray beam with a high intensity at the sample surface. A schematic illustration of the measurement assembly is shown in Figure 3.4 [147].

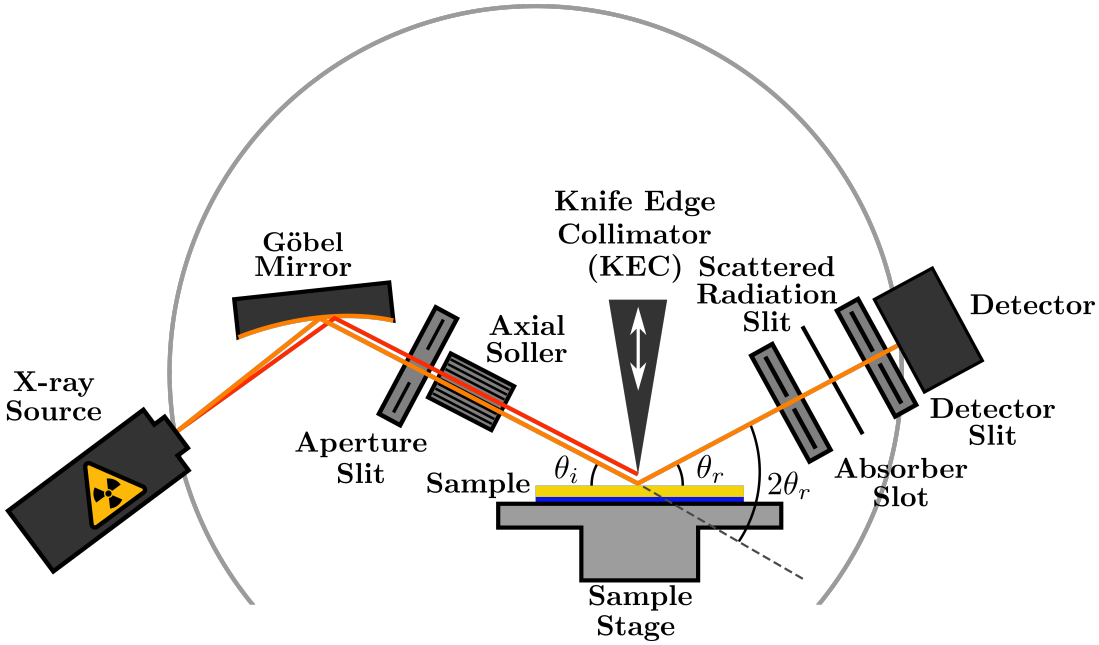

Figure 3.4.: Schematic illustration of the parallel beam geometry for XRR measurements. The X-ray beam coming from the X-ray source is parallelized by a Göbel mirror before being focused onto the thin film sample with an equal incident and reflected angle ($\theta_i = \theta_r$). By introducing different slits, an absorber, a soller, and a knife edge collimator (KEC), detector oversaturation is prevented and the beam is shaped and focused [147].

The divergent X-rays coming from the X-ray source are parallelized using a curved mirror, known as a Göbel mirror. Furthermore, since the Göbel mirror is wavelength dependent, the amount of Cu Kβ radiation is reduced. By the use of an aperture slit, the resulting parallel beam width is adjusted and thus the length of the sample that is irradiated. To account for the axial divergence of the beam an axial soller is additionally placed in front of the sample, which is mounted on a sample stage. For the purpose of alignment, the sample stage is motorized to adjust the height and the tilt. A knife edge collimator (KEC) is placed directly on top of the sample, which ultimately defines the illumination footprint on the sample and prevents overillumination as well as direct beam contributions at very small incident angles. After reflection at the sample, additional slits are placed into the beam path in front of the detector to define the beam before detection. For a scintillation detector, incident X-rays are converted to ultraviolet or visible light, which is multiplied by a photomultiplier tube. The resulting photons are then converted to the recorded electrical signal.

Instrument For the XRR measurements a D8 Advance diffractometer (Bruker, Billerica, USA) operated in the parallel beam geometry at a voltage of 40 kV and a current of 40 mA is used. The instrument is equipped with a copper anode to emit X-rays with a wavelength of $\lambda_{\mathrm{Cu\ K\alpha}} = 1.54$ Å. By the use of slits, the monochromatic, vertically collimated beam is focused on a sample of minimum 2×2 cm^2 size. For an incident angle of θ, the detector is located at 2θ relative to the incident beam, i.e., at the specular position as also shown in Figure 3.4. The scans are performed in the coupled $\theta/2\theta$ configuration in a typical range of $2\theta = 0.04°$ to $4.00°$ with a step size of $0.002°$, while each step is measured for 2 s. For the incident beam a divergence slit with a slit size of 0.05 mm is placed in front of the axial soller before the sample. For the receiving slits, placed behind the sample, 0.1 mm and 0.05 mm slits for the scattered-radiation slit and the detector slit are chosen, respectively. Furthermore, a KEC is placed above the sample. Prior to a measurement, the X-ray source is heated up, followed by a direct beam measurement to determine the position of the incident X-ray beam. Furthermore, to adjust the height and in order to align the sample surface parallel to the incident beam, a z-scan and a rocking scan are performed. During this alignment procedure a copper foil of 0.1 mm thickness is placed in the absorber slot between the two receiving slits to reduce the count rate of the primary beam on the detector. The raw data is treated by normalization of the intensity as well as by reformulation of the intensity in terms of q_z. The measured reflectivity curves are analyzed using either the Motofit plugin [148] for IGOR PRO 6.37 (Wavemetrics, Portland) or the algorithms implemented in the Python program *refnx* [149]. In Table 3.1 the calculated X-ray SLD values of the materials used in this thesis are shown.

Table 3.1.: X-ray SLD values of the materials used in this thesis.

	D_2O	H_2O	C_3H_6O	$Mg(ClO_4)_2$	$Mg(NO_3)_2$	$NaClO_4$	PNIPMAM
SLD / 10^{-6} Å^{-2}	9.45	9.47	7.36	18.71	19.62	21.03	10.37

3.3. Time-of-Flight Neutron Reflectivity

Similar to XRR, neutron reflectivity (NR) is a non-invasive surface sensitive technique to probe the thickness, SLD, and roughness of thin layered films [134,150]. The wavelengths of neutrons used for the experiments in this thesis are typically in the range of $2 - 27$ Å. In contrast to X-rays discussed in Section 3.2, neutrons are scattered at the nuclei either elastically, i.e., without the change in energy, or inelastically, i.e., with a change in energy. For reflectivity, elastic scattering is essential for coherent interference patterns. The scattering ability of a nucleus is described by the neutron scattering length density, which varies apparently random with the atomic number and the isotope. This, however, can be leveraged in the investigation of macromolecules in a medium, since ^{1}H and ^{2}H have significantly different coherent scattering lengths, i.e., -3.74 fm and 6.67 fm, respectively [151,152]. Therefore, the contrast can be varied by deuteration of either the macromolecule itself or the surrounding medium. This is contrary to XRR, for which the scattering lengths of the different isotopes are almost identical. However, ^{1}H also has a particularly large incoherent scattering contribution leading to diffuse scattering at the nuclei, which results in strong background contributions especially at high q_z values in reflectivity measurements.

Measurement Principle NR measurements can either be performed in dispersive mode with a monochromatic neutron beam or in time-of-flight (ToF) mode using a wavelength band of neutrons. By the use of a chopper system, which is able to separate neutrons according to their wavelength, both modes of operation can be realized [153,154]. In the case of dispersive NR experiments, the angle of the incident beam has to be varied, as described for XRR in Section 3.2, to obtain a broad q_z-range, whereas in the ToF mode a wavelength band is used. The wavelength λ of a neutron is related to its velocity v by the de Broglie relationship $v = {}^{h}/_{m\lambda}$, where m is the neutron mass (1.675×10^{-27} kg) and h is Planck's constant (6.626×10^{-34} Js). A pulsed neutron beam of different wavelengths is realized by a rotating double disc chopper system, where the selected wavelength band is defined by the chopper opening. For a known distance l between the chopper system and the detector, the wavelength of a neutron arriving at the detector can be obtained from the time of flight t according to $\lambda = {}^{th}/_{ml}$, where it is assumed that elastic scattering occurs and thus that the neutrons do not change their velocity. However, the mass of the

neutrons leads to a deviation from the theoretically predicted angle due to gravitational effects depending on the velocity of the neutrons, which has to be accounted for [155].

In ToF mode a variation in the scattering transfer vector q is achieved by a variation of wavelengths, which however in practical application is accompanied with variations $\Delta\lambda$ in the wavelength λ as well as with variations $\Delta\theta$ in the incident angle θ_i. Therefore, the error propagation in q is given by

$$\left(\frac{\Delta q}{q}\right)^2 = \left(\frac{\Delta\lambda}{\lambda}\right)^2 + \left(\frac{\Delta\theta}{\theta}\right)^2 . \tag{3.8}$$

An increased divergence of the incoming angle and/or of the wavelength increases the neutron flux on the sample but reduces the resolution $\Delta q/q$ in q. The divergence of the neutron beam is defined by a combination of the opening of the collimation slits, the choppers, and the detector resolution. Additionally, neutrons scattered at a non-flat surface also contribute to the divergence of the reflected beam. For this, corrections to account for divergence in order to increase the resolution without sacrificing flux have been proposed [156].

Instrument The static and kinetic ToF-NR measurements are conducted at the D17 instrument at the Institute Laue-Langevin (ILL) in Grenoble, France. The D17 instrument, which is schematically shown in Figure 3.5, is a versatile reflectometer which can be operated in ToF mode as well as in monochromatic mode with both polarized or non-polarized neutrons [153,154].

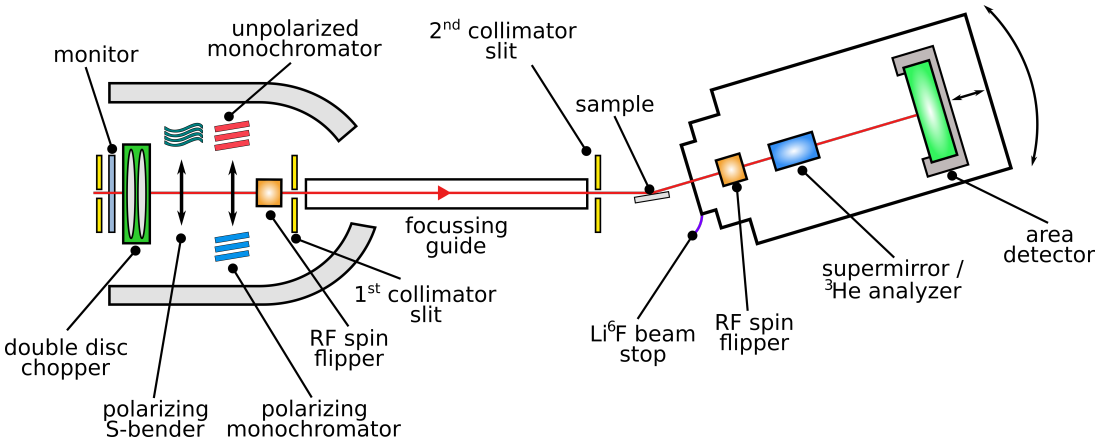

Figure 3.5.: Schematic layout of the D17 instrument at ILL. Neutrons are guided through a double disc chopper to chop the neutrons into a defined wavelength band. By collimator slits and a focussing guide the neutrons are focused onto the sample. The reflected neutrons are detected and analyzed according to their time of flight. Adapted from Ref. [154].

The reflectometer is designed in a horizontal scattering geometry, which as a consequence requires a vertical position of the sample. Due to the high white beam neutron flux of 9.6×10^9 $ns^{-1}cm^{-2}$ and a low instrumental background, reflectivities down to 10^{-7} are measurable. The ToF mode is realized by pulsing neutrons through a double chopper system with variable inter-chopper distance ($1 - 11$ cm) and projected sector opening ($0 - 45°$). Since the usable wavelengths of the neutrons is between 2 and 30 Å, the chopper period is set just above the ToF (58 ms) of the 30 Å neutrons. Neutrons with wavelengths higher than 30 Å are reflected out in the focusing guide and in practical applications the maximum of the wavelength band is limited to 27 Å due to intensity constraints. The ToF mode enables the measurement of reflectivity curves in a broad q_z range without the necessity to move the sample or the detector. The two-dimensional detector has an area of 473×250 mm^2 with a spatial resolution of 2.2×5.2 mm^2 and can be placed between 1.0 and 3.1 m from the sample. To reduce scattering contributions from air, the whole detector is placed in a vacuum tank. In addition, to enable high temporal resolution for kinetic measurements, the coherent summation method by Cubitt et al. [156,157] is used which permits the use of divergent beams without a loss of resolution.

In this thesis, ToF-NR measurements are conducted with a wavelength band range between 2 and 27 Å, a sample-detector distance of 3.1 m, and a spectral resolution of $\Delta\lambda/\lambda = 10\%$. Static measurements at equilibrated states of the thin film sample are performed at two incident angles ($\theta_i = 0.5°$ for $10 - 15$ min and $\theta_i = 2.5°$ for $20 - 30$ min) which are summed up to obtain a large q_z range. Kinetic measurements are likewise conducted at one out of two incident angles ($\theta_i = 1.0°$ for 5 s and $\theta_i = 1.5°$ for 5 s), however in this case not to increase the q_z range, but instead to prevent detector damage due to higher count rates originating from a varying scattering ability of the system throughout the measurement. The sample size of 7×7 cm^2 is chosen according to the beam area of 6×50 mm^2 and the samples are placed into the custom-built neutron chamber described in Section 4.1.1. The resulting reflectivity curves are analyzed using either the Motofit plugin [148] for IGOR PRO 6.37 (Wavemetrics, Portland) or the algorithms implemented in the Python program *refnx* [149]. In Table 3.2 the calculated coherent neutron SLD values of the materials used in this thesis are shown.

Table 3.2.: Coherent neutron SLD values of the materials used in this thesis.

	D_2O	H_2O	C_3H_6O	$Mg(ClO_4)_2$	$Mg(NO_3)_2$	$NaClO_4$	PNIPMAM
SLD / 10^{-6} Å^{-2}	6.39	-0.56	0.27	4.23	5.50	4.48	0.74

3.4. Fourier-transform Infrared Spectroscopy

Fourier-transform infrared spectroscopy (FTIR) is a measurement technique for the identification of functional groups of a compound and can consequently be used to investigate the chemical structure of a material. As in all spectroscopic methods, a transition can only take place when the frequency of the incident photon matches the energy gap between two states. In the mid-infrared region the transition is typically in the range of 4000–400 cm^{-1}. In this region of the electromagnetic spectrum, molecular vibrations with matching vibrational frequencies are excited. In the quantum mechanical picture, the energy levels of the vibrational states – approximated by an harmonic oscillator – are obtained as the solution of the Schrödinger equation [158–160]

$$E_v \Psi_v = \left(-\frac{\hbar^2}{2m_r} \frac{d^2}{dx^2} + \frac{1}{2} k x^2 \right) \Psi_v \,, \tag{3.9}$$

where Ψ_v is the vibronic wave function, E_v is the energy of the vibrational state with quantum number v, $\hbar$ is the reduced Planck constant, m_r is the reduced mass of the involved atoms, and k is the spring constant according to Hooke's law. Accordingly, E_v is given as

$$E_v = (v + 1/2)\hbar \sqrt{\frac{k}{m_r}} \,, \tag{3.10}$$

and the energy of a transition ΔE between two neighboring states v and $v+1$ is therefore given by

$$\Delta E = E_{v+1} - E_v = \hbar \sqrt{\frac{k}{m_r}} \,. \tag{3.11}$$

To determine whether or not a transition is allowed, the transition has to have a non-zero transition dipole moment $\mu_{v \to v'}$ for a particular mode Q, which is defined as

$$\mu_{v \to v'} = \int_{-\infty}^{\infty} \Psi_{v'}^*(Q) \hat{\mu}(Q) \Psi_v(Q) dQ \,. \tag{3.12}$$

Here, $\hat{\mu}$ is the dipole moment operator in terms of mode Q, which can be expanded in a Taylor series. Inserting the first two terms of the expansion into the expression for $\mu_{v \to v'}$, the transition dipole moment can be approximated as

$$\mu_{v \to v'} = \mu(Q=0) \int_{-\infty}^{\infty} \Psi_{v'}^*(Q) \Psi_v(Q) dQ + \left. \frac{d\mu(Q)}{dQ} \right|_{Q=0} \int_{-\infty}^{\infty} \Psi_{v'}^*(Q) Q \Psi_v(Q) dQ \,. \tag{3.13}$$

Here, the first term describes the overlap integral between the corresponding wave functions. Due to the orthogonality of the wave functions for different quantum numbers v, this term is necessarily zero. The second term consists of the change of the dipole moment $\mu(Q)$ along the mode Q, which becomes non-zero if the dipole moment changes along the mode. The remaining integral can be shown to be different from zero only if the transition occurs between neighboring vibrational states. Therefore, the selection rules for a transition to be allowed (IR-active) are that the dipole moment has to change and that $\Delta v = \pm 1$ must apply. Furthermore, Equation 3.11 shows that the vibrational transition is dependent on k, i.e., the spring constant according to Hooke's law between atoms participating at the vibration, which corresponds to the bond strength. Accordingly, ΔE increases with the bond strength and with a smaller reduced mass, i.e., with lighter involved vibrating atoms. However, due to the charged nature of the electrons and nuclei comprising atoms, the description of a harmonic oscillator is not sufficient, due to neglected repulsive and attractive forces. The deviations can better be described using the Morse potential, yielding the anharmonic oscillator approximation. In Figure 3.6 the potentials for both oscillator types are depicted graphically with the first few resulting energy levels.

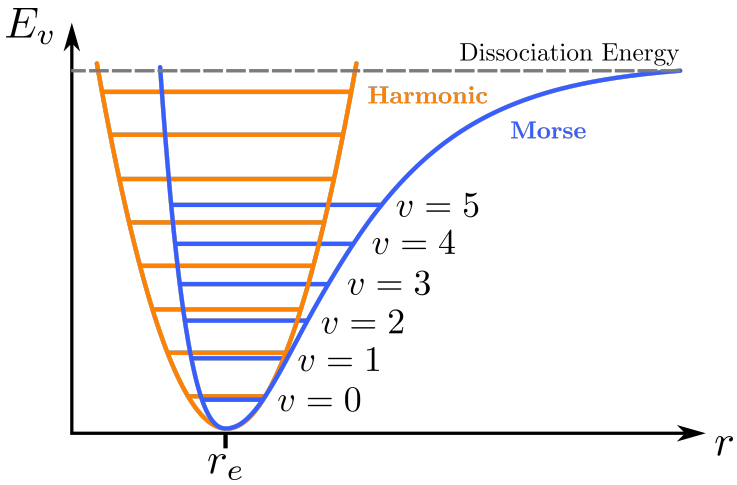

Figure 3.6.: Graphical representation of the harmonic and Morse oscillator. The potential energy of the harmonic oscillator and the corresponding vibrational states are shown in orange, whereas the anharmonic description is shown in blue. The dashed line represents the dissociation energy and r_e the equilibrium bond length [158–160].

Molecular bond strengths exhibit strong dependence on the bond length when oscillating around their equilibrium bond length r_e, which is not captured by the harmonic potential. On the one hand, due to repulsive forces between the atoms at very short distances, the energy increases rapidly for $r \to 0$. On the other hand, stretching the bond far above r_e results in bond dissociation after a certain internuclear distance is reached. Both effects

are accurately accounted for by the anharmonic Morse potential. As a consequence, the density of the vibrational states is increased towards the dissociation energy, which is in contrast to the harmonic oscillator for which all states are equidistant.

In general, a molecular system with n atoms has $3n$ degrees of freedom of motion according to the three Cartesian coordinates of each atom. Therefore, after subtracting the translational and rotational degrees of freedom, the number of vibrational modes n_v for a non-linear molecule is given as [161]

$$n_v = 3n - 6\,. \tag{3.14}$$

In addition to stretching modes, which can be described with the (an)harmonic oscillator approximation, additional vibrational modes can result. All vibrational modes for a AX_2 system are shown in Figure 3.7, where atom A is indicated in black and atoms X are represented in blue.

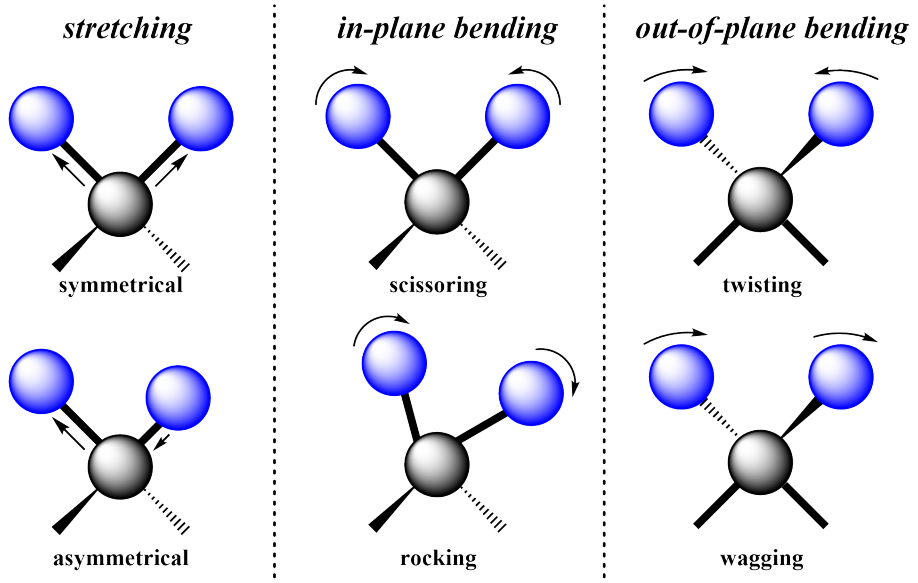

Figure 3.7.: Schematic representation of the vibrational modes for a AX_2 system [161] categorized into stretching, in-plane bending, and out-of-plane bending vibrations. Atom A is indicated in black and atoms X are represented in blue.

The different vibrational modes can be separated into three different main vibration types: Stretching, in-plane bending, and out-of-plane bending. Depending on the symmetry of the underlying vibrations, the modes can further be subcategorized into symmetric or asymmetric stretching, scissoring or rocking for in-plane bending, and twisting or wagging for out-of-plane bending. As the vibrational frequency of an oscillation is directly proportional to the bond strength and the masses of the participating atoms, FTIR can

consequently resolve the substituents of a chemical compound. Furthermore, in *in situ* experiments, in which an experimental parameter is varied over time, e.g., relative humidity or temperature, evolving interactions between functional groups of different compounds can be resolved.

2D Correlation Analysis In the context of *in situ* measurements the varying part of the spectrum is sometimes referred to as the dynamic spectrum [162]. The dynamic spectrum contains the response of a system towards an external stimulus, which is also referred to as a perturbation in the following context. In 2D FTIR correlation analysis the sequentially collected dynamic spectra under the influence of a certain perturbation are subjected to a mathematical procedure generating the 2D correlation spectra. When the perturbation evolves over time, the mathematical treatment can be done in terms of time [163,164]. Thus, the correlation spectrum $X(\nu_1, \nu_2)$ is obtained as

$$X(\nu_1, \nu_2) = \langle I(\nu_1, t) \cdot I(\nu_2, t') \rangle \,, \tag{3.15}$$

where $I(\nu_i, t)$ is the spectrum at wavenumber ν_i and time t. Here, $\langle \cdot \rangle$ denotes the correlation function, which in the context of 2D FTIR correlation analysis is chosen as

$$X(\nu_1, \nu_2) = \Phi(\nu_1, \nu_2) + i\Psi(\nu_1, \nu_2) \,, \tag{3.16}$$

where Φ constitutes the real part and is known as the synchronous 2D correlation intensity, whereas Ψ constitutes the imaginary part and is known as the asynchronous 2D correlation intensity. The synchronous correlation spectrum represents simultaneous or coincidental changes of spectral intensity variations at different wavenumbers ν_1 and ν_2 and can be obtained as

$$\Phi(\nu_1, \nu_2) = \frac{1}{m-1} \sum_{j=1}^{m} I(\nu_1, t_j) I(\nu_2, t_j) \,. \tag{3.17}$$

Here, it should be noted that the time is discrete as spectra are obtained one after another. Likewise, the asynchronous 2D correlation spectrum represents sequential or successive changes of spectral intensities at ν_1 and ν_2 and is given as

$$\Psi(\nu_1, \nu_2) = \frac{1}{m-1} \sum_{j=1}^{m} I(\nu_1, t_j) \sum_{k=1}^{m} N_{jk} I(\nu_2, t_k) \,, \tag{3.18}$$

where N_{jk} are elements of the Hilbert–Noda transformation matrix defined as [163,164]

$$N_{jk} = \begin{cases} 0 & \text{if} \quad j = k \\ {}^{1}\!/_{\pi(k-j)} & \text{otherwise} \end{cases} . \tag{3.19}$$

Correlation is then usually analyzed by plotting the synchronous (Figure 3.8a) and asynchronous (Figure 3.8b) parts of dynamic spectra [165,166].

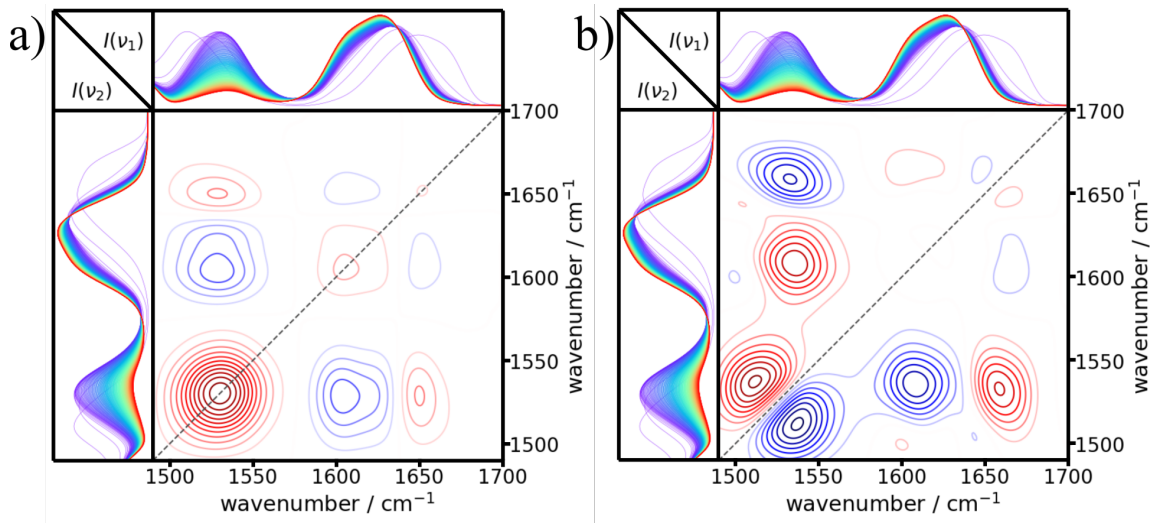

Figure 3.8.: Exemplary (a) synchronous and (b) asynchronous 2D FTIR correlation spectra of a PNIPMAM film swelling in a D_2O vapor atmosphere (perturbation) over time in the wavenumber range between 1490 and 1700 cm^{-1} for the amide I (1650 cm^{-1}) and the amide II (1510 cm^{-1}) bands. In the contour plot, areas colored in red indicate positive correlation and areas colored in blue indicate negative correlation. Reprinted with permission from Ref. [167]. Copyright 2023 American Chemical Society.

In order to evaluate the resulting correlation plots specific rules have to be considered. For synchronous correlation $\Phi(\nu_1, \nu_2)$ the peaks occurring on the diagonal line are referred to as autopeaks, which according to Equation 3.17, always have a positive sign (indicated in red). Strong autopeaks develop if a signal changes its intensity greatly under the influence of a perturbation. In contrast, peaks occurring at the off-diagonal are referred to as crosspeaks, which indicate simultaneous or coincidental changes of two signals observed at two positions ν_1 and ν_2. If the sign of a crosspeak is positive, represented in red in Figure 3.8, the intensities of the two signals are either increasing or decreasing concurrently. Whereas, if the sign is negative, represented in blue in Figure 3.8, one of the signals is increasing while the other one is decreasing in intensity. In contrast to the synchronous correlation plots, the asynchronous correlation $\Psi(\nu_1, \nu_2)$ yields information about sequential changes of signals at two different wavenumbers ν_1 and ν_2. Due to the definition of the Hilbert–Noda transformation matrix in Equation 3.19, the asynchronous spectra does not show autopeaks and possesses only crosspeaks. Crosspeaks only develop, if the intensities of the signals are changing either delayed or accelerated with respect to each other. If the intensity of signal ν_1 occurs primarily before signal ν_2 the sign of the crosspeak is positive, whereas the sign is negative if the change occurs after ν_2. However,

the order of events is reversed if the respective crosspeak in the synchronous correlation plot is negative. In general, a perturbation can not only change the intensity of a signal but also the peak position, which leads to a smearing out of the correlation peaks and further complicates the analysis of the 2D FTIR correlation plots.

In summary, 2D FTIR correlation analysis enables the elucidation of the influence of a perturbation on the signal intensities and the order of changes. By matching the individual signals to their originating moieties in the molecule, a comprehension of the underlying sequence of functional group participation can be gained. On the example of the hydration of a polymer acting as the perturbation, the step-wise hydration mechanism of the involved functional groups can be deduced.

Measurement Principle Compared to a conceptually simpler dispersive IR spectrometer, where each wavelength is measured and detected individually, a Michelson interferometer used in FTIR devices allows to measure different wavelengths at the same time [168,169]. This has the advantage that not only the measurement time but also the signal-to-noise ratio is reduced, due to the more accurate underlying measurement principle. The working principle of a Michelson interferometer used in FTIR devices is shown in Figure 3.9.

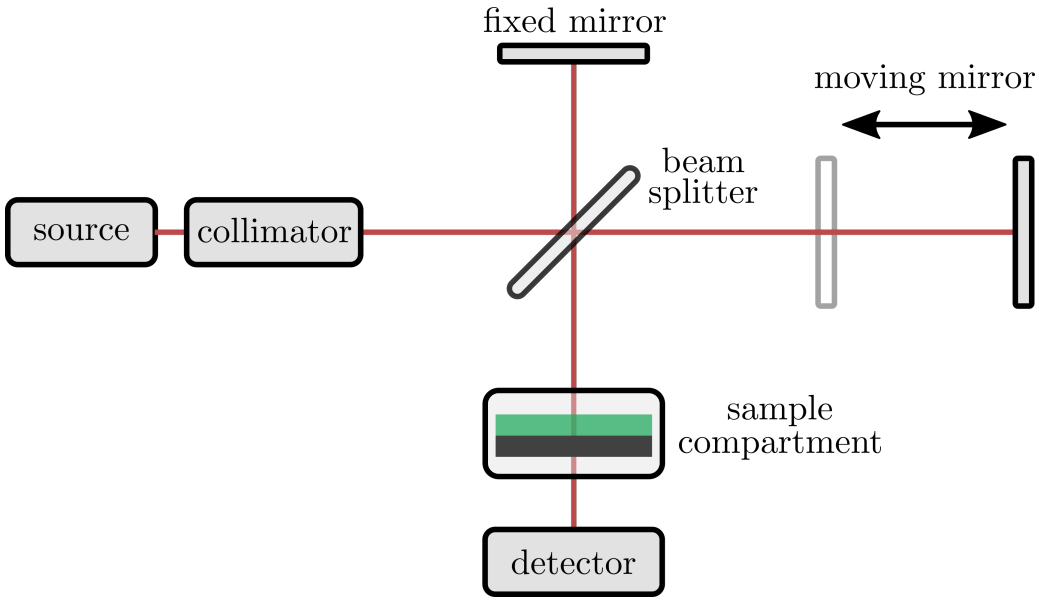

Figure 3.9.: Schematic assembly of a Michelson interferometer used in FTIR devices [168,169]. Light coming from the source is collimated before hitting on a beam splitter, after which the split beam is guided to a fixed and a moving mirror. The reflected waves pass through the sample before being detected.

A Michelson interferometer used in FTIR devices consists of an IR source, a collimator, a beam splitter, two mirrors, a laser, a sample compartment, and a detector. The IR beam is usually generated by a black-body-like source and is guided towards a beam splitter, which is a partially transmissive mirror that splits the beam into two parts. One part is reflected by 90° to a fixed perfect mirror, while the other part is transmitted to a moving perfect mirror, which is moving at a constant velocity. The reflected beams are then recombined at the beam splitter and due to the difference of the optical path lengths and the resulting phase shift of the beams, constructive and destructive interference occurs. The resulting combined beam is then guided to the sample compartment, and finally to the detector. Simultaneously, the beam of the reference laser follows the same beam path for calibration.

The superposition $I(x)$ of the recombined beams can be expressed in terms of the path length x as

$$I(x) = I_0[1 + \cos(2\pi\nu x)]\,, \tag{3.20}$$

where I_0 is the intensity of the incident beam and ν is the wavenumber. To obtain the intensity over a range of optical path lengths, the position of the moving mirror is adjusted and the intensity measured for each position. Therefore, the intensity can also be expressed in terms of the position δ of the moving mirror as

$$I(\delta) = I_0[1 + \cos(2\pi\nu\delta)]\,. \tag{3.21}$$

Plotting $I(\delta)$ as a function of δ is known as the interferogram. To obtain the intensity dependent on the wavenumber, a Fourier transformation of $I(\delta)$ is performed as

$$I(\nu) = \int_{-\infty}^{\infty} I(\delta)\exp(i2\pi\delta\nu)\,d\delta\,. \tag{3.22}$$

which yields the FTIR spectrum. Since this requires precise knowledge of the mirror position δ, simultaneously the interferogram of the reference laser is evaluated to obtain a precise value for δ. Finally, to account for background contributions, e.g., from the supporting substrate, a reference spectrum is subtracted from the sample spectrum. The overall data processing from the interferogram to the final FTIR spectrum is shown in Figure 3.10.

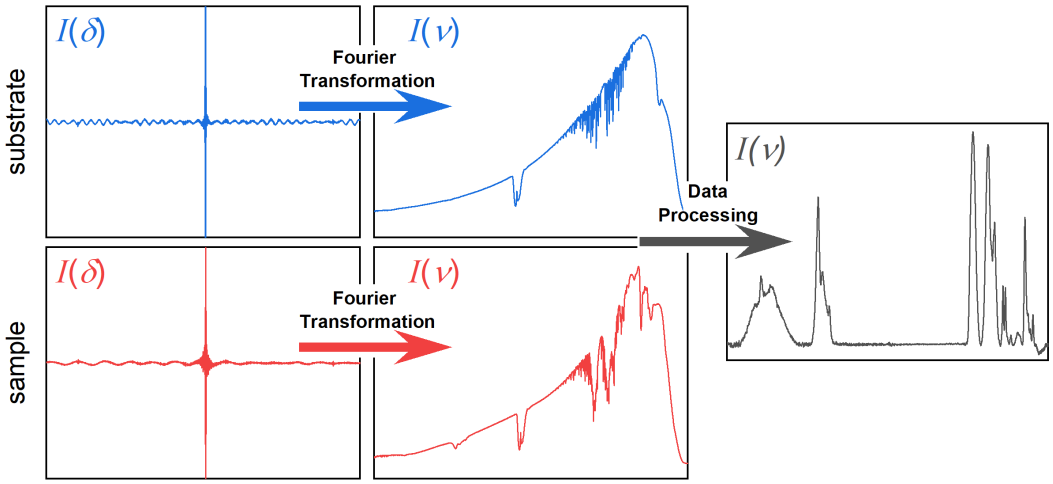

Figure 3.10.: Data processing of the interferogram of the substrate (blue) and the sample (red) by Fourier transformation followed by subtraction of the substrate spectrum, baseline correction and atmospheric compensation.

Instrument For the *in situ* FTIR measurements an Equinox 55 (Bruker Corporation, Billerica, USA) FTIR spectrometer equipped with a Michelson interferometer and a deuterated triglycine sulfate (DTGS) detector is used. To reduce the amount of IR-active species originating from ambient air in the beam pathway, the spectrometer is continuously flushed with dry and CO_2-filtered air. The 1×1 cm^2 samples are placed into the custom-made copper chamber as described in Section 4.1.2. The spectra are collected at a constant temperature of 23 °C by summation of 125 scans with a resolution of 2 cm^{-1} and within a typical wavenumber range of 4000–400 cm^{-1}. Before an *in situ* experiment is started, a silicon substrate is measured as reference with the same settings as stated above. For each solvent vapor atmosphere, spectra are conducted until an equilibrated state is reached, i.e., until no more changes in peak positions or intensities occur. Afterwards, baseline correction (concave rubber band method) and atmospheric compensation (further reduction of atmospheric H_2O and CO_2 molecules) are carried out for each spectrum in the Opus v6.0 software. The solvent uptake behavior is followed by numerical integration of characteristic signals, while the peak positions are determined by Gaussian fits.

4. Flexible Sample Environment

For the investigation of the polymer films under different solvent vapor atmospheres, a specifically designed and flexible sample environment is used. All parts of the flexible sample environment are custom-built at the Technical University of Munich in the group of Prof. P. Müller-Buschbaum by Tobias Widmann and Dr. Lucas P. Kreuzer (Sections 4.1.1 and 4.2) [170] and by Prof. Alfons Schulte (Section 4.1.2). By connecting the gas flow system to one of the designed measurement chambers, different solvent vapor atmospheres can be created in the surrounding of a sample, enabling to follow the film's response with *in situ* SR, ToF-NR, and FTIR experiments. The neutron and the FTIR chamber are temperature controllable and are designed according to the instrument requirements. In the following sections, first the measurement chambers will be addressed followed by a detailed description of the gas flow system.

4.1. Measurement Chambers

For the investigation of stimuli-responsive thin films, it is important to control and stabilize environmental conditions to reduce interference of different film responses originating from different external influences. Therefore, specifically designed, custom-built measurements chambers are used. First, the spherical neutron chamber will be presented in Section 4.1.1 followed by a description of the FTIR chamber in Section 4.1.2.

4.1.1. Neutron Chamber

For the *in situ* SR and ToF-NR measurements a custom-built spherical chamber, suitable for neutron experiments is used [170]. The chamber consists of an AlSi10Mg alloy and is 3D printed to facilitate the fabrication of unique and modular components to adapt to the requirements of an experiment. Furthermore, the neutron chamber is designed to stabilize and control thermodynamic conditions in the surrounding of a sample. It offers the flexibility to introduce various stimuli, such as temperature, light or solvent vapor atmospheres. In addition, by exploiting the modularity of the chamber design, simultaneous SR measurements during the ToF-NR experiments can be performed. In Figure 4.1 the neutron chamber is shown in the wireframe model and in a 3D visualization.

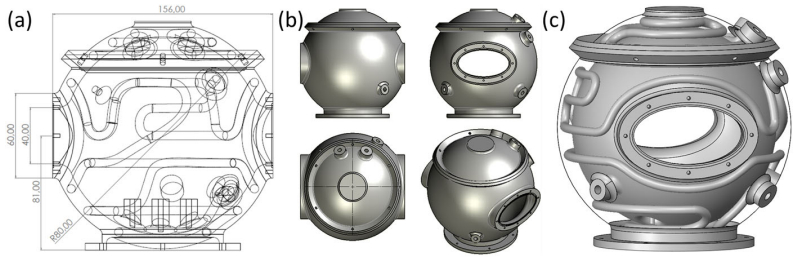

Figure 4.1.: (a) Side view of the wireframe model of the neutron chamber. Labels denote the chamber measures in mm. (b) Chamber from different perspectives: side (top left), front (top right), top (bottom left), and isometric (bottom right). (c) 3D visualization of the fluid channels embedded in the chamber walls. Reprinted with permission from Ref. [170].

The spherical chamber has a volume of 1.4 L with an inner diameter of 140 mm and is able to incorporate a sample size of up to 7 × 7 cm^2, either vertically or horizontally, which is optimal for neutron experiments. The chamber features elliptical aluminum windows with a thickness of 0.1 mm as an entry and exit for the neutron beam, allowing incident and exit angles up to 5 °. Additionally, a 2.4 m long fluid channel system with a diameter of 6 mm, centered within the 10 mm thick walls can be connected to a thermal bath system, which enables optimized heat transfer. The edgeless, spherical design facilitates experiments at high humidity, as condensation is greatly reduced. Furthermore, by the implementation of a SHT31 sensor (Sensirion AG, Staefa, Switzerland) to measure the temperature and the relative humidity close to the sample, the changing surrounding environment can be tracked. Through a gas in- and outlet, the gas flow system can be easily connected to the neutron chamber and the out-coming vapor is guided through a washing bottle filled with water. Furthermore, the neutron chamber can be coupled to a SR device as shown in Figure 4.2.

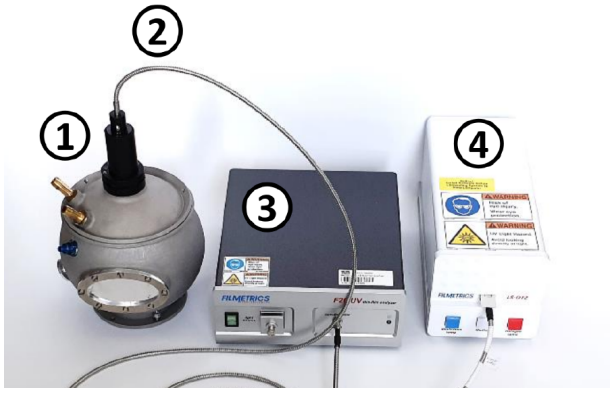

Figure 4.2.: Neutron chamber coupled with a SR device equipped with a 1) cable mounting support, 2) a optical fiber cable, 3) a spectrometer, and 4) a light source. Adapted from the dissertation of Dr. Lucas P. Kreuzer [171].

The SR device is connected to the neutron chamber by a mounting support which allows for an precise alignment of the optical fiber cable. The white light passes through a CaF_2 window centered on the chamber lid and is focused on the sample with a diameter of roughly 2 mm and at a distance of 10 cm.

4.1.2. FTIR Chamber

Since the *in situ* FTIR measurements are conducted in transmission mode, different requirements as in the preceding section are posed, not only for the chamber but also for the sample. On the one hand, to reduce the signal-to-noise ratio thicker and non-flat films in the µm regime are necessary. On the other hand, on top of being temperature controllable, an enclosed environment has to be generated to be able to perform experiments during the vapor flow. To enable these types of measurements in transmission mode, the FTIR chamber is equipped with two IR transmissive ZnS windows, which close the sample compartment with the help of a sealing ring. The custom-built FTIR measurement chamber is schematically depicted in Figure 4.3

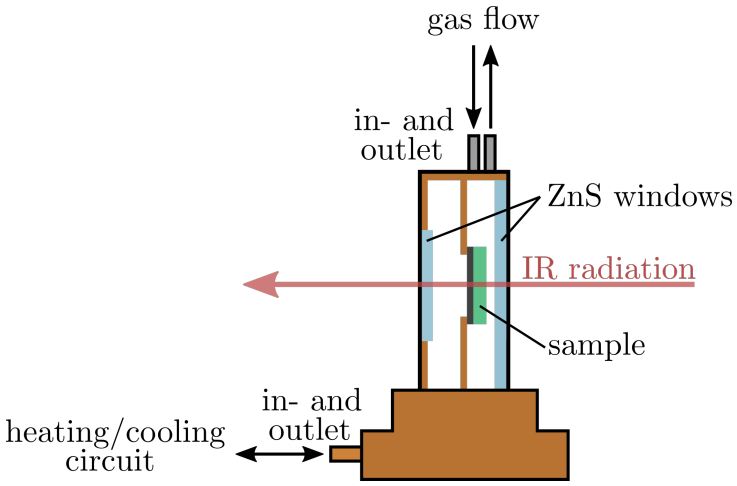

Figure 4.3.: Schematic depiction of the FTIR chamber consisting of two ZnS windows, a sample compartment, and an in- and outlet for the gas flow as well as the heating/cooling circuit.

The copper chamber can incorporate sample sizes up to 1×1 cm^2 which can be mounted between the two IR transmissive ZnS windows. The bottom part of the chamber features a temperature controllable unit consisting of a copper block with an in- and outlet for a heating/cooling circuit. Due to the good thermal conductivity of copper, the top part containing the sample is tempered as well, which is monitored with a sensor to track the temperature and the relative humidity in vicinity to the sample. The different saturated solvent vapors are guided into the chamber by cannulas pierced through a sealing ring acting as in- and outlets. The described chamber equipped with a sample, the sensor,

and the cannulas is shown in Figure 4.4a, whereas Figure 4.4b shows the measurement chamber mounted in an Equinox 55 FTIR instrument.

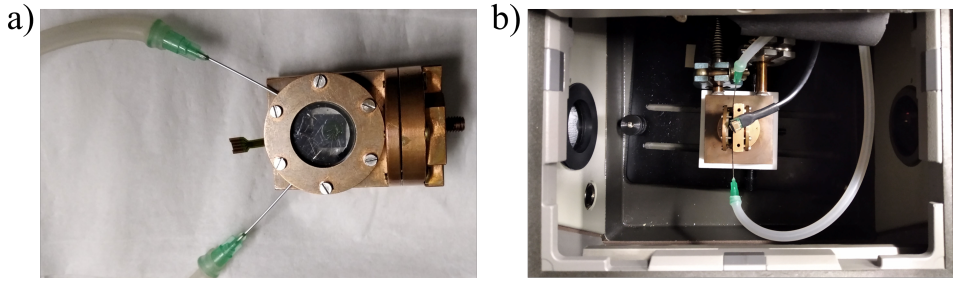

Figure 4.4.: (a) Image of the custom-built FTIR measurement chamber in the frontal view equipped with a sample, a sensor, and the gas in- and outlet. (b) FTIR chamber mounted in an Equinox 55 FTIR instrument.

4.2. Gas Flow System

To generate the aforementioned saturated solvent vapor atmospheres in the different measurement chambers, a custom-built gas flow system is used, which is schematically depicted in Figure 4.5 [170,172].

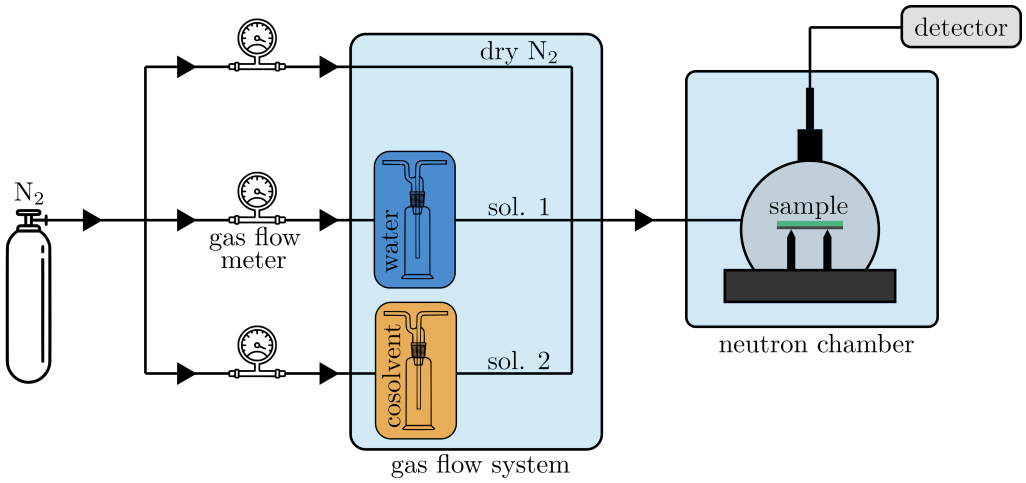

Figure 4.5.: Schematic representation of the gas flow system coupled to the neutron chamber. The blue boxes indicate the temperature controlled units and the black arrows the direction of the gas flow.

To generate a stable and controlled vapor flow of different solvents, three gas flow meters (F-201CV-1K0, Bronkhorst High-Tech B.V.Ak Ruurlo, Netherlands) are used, which are calibrated for nitrogen gas at 2 bar and 20 °C. By the use of the provided FlowDDE

software the gas flow meters can be regulated individually to a flow rate between 0 and 1 $Lmin^{-1}$. In total, the three gas flow meters can then be operated either individually or in conjunction. One flow channel was designed to provide a pure and steady nitrogen gas flow in the measurement chamber, which can be used to dry a sample or to adjust the environment to a desired humidity. The two other gas flow meters guide a defined nitrogen stream into washing bottles (Neubert-Glas GbR, Geschwenda, Germany), which are filled with the solvent (mixture) of interest. Thereby, the nitrogen gas saturates with the solvent and is then guided into the measurement chamber. By addressing more than one gas flow meter, mixtures of solvent atmospheres can be realized. Specifically, this allows to generate atmospheric conditions, which are suitable for the investigation of the solvent uptake behavior and the cononsolvency effect of polymer thin films, which requires precise control of the solvent vapor ratio. To allow for a proper mixing of the vapor components, the three streams are merged into one before entering a measurement chamber. The released vapor flow is guided through an exhaust tube to a large washing bottle to purge the vapor from potentially hazardous substances before releasing it into the surrounding atmosphere. To avoid condensation inside the measurement chamber due to temperature differences between the chamber and the introduced vapors, it is important to equalize the temperatures. This is realized by a refrigerated heating circulator (FP50-HL, JULABO Labortechnik GmbH, Seelbach, Germany), which is tempering the gas flow system and the measurement chamber as well as the connection between them. To confirm the uniformity of the temperature of the gas flow setup and the measurement chamber, a temperature SHT31 sensor (Sensirion AG, Staefa, Switzerland) is used.

5. Sample Preparation

5.1. Materials

In the following sections, the materials used throughout this thesis, the substrate treatment procedure, and the film deposition methods are presented.

5.1.1. PNIPMAM

Poly(*N*-isopropylmethacrylamide) (PNIPMAM) is a homopolymer bearing hydrophilic amide groups and hydrophobic alkyl groups. PNIPMAM is thermoresponsive and exhibits an LCST around 44 °C in aqueous solution [37–41]. The chemical structure of PNIPMAM is shown in Figure 5.1.

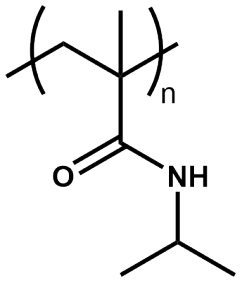

Figure 5.1.: Chemical structure of poly(*N*-isopropylmethacrylamide) (PNIPMAM).

The homopolymer PNIPMAM is synthesized and characterized by Dr. Dirk Schanzenbach at the Chair of Applied Polymer Chemistry of Prof. Dr. André Laschewsky at the University of Potsdam. PNIPMAM is synthesized by conventional radical polymerization with azo-bis-isobutyronitrile (AIBN) in THF at 60 °C [40]. By size exclusion chromatography (SEC) the number average molar mass of $M_{n,\mathrm{SEC}} = 11,300$ g/mol and the dispersity of Đ = 2.0 are obtained. The homopolymer is used as received without further treatment and stored under cool, dark and dry conditions.

5.1.2. Salts

The different salts used to tune the response behavior of PNIPMAM thin films under different vapor atmospheres are presented in the following.

$NaClO_4$ (ACS reagent, $\geq$ 98.0%, Sigma Aldrich Chemie GmbH (Taufkirchen, Germany)) is a white, hygroscopic salt with a molar mass of 122.44 g/mol, a density of 2.52 g/mL, and a solubility of 2096 g/L in water at 20 °C. The salt has a rhombic crystal system and is thermally stable to up to 490 °C.

$Mg(ClO_4)_2$ (ACS reagent, Sigma Aldrich Chemie GmbH (Taufkirchen, Germany)) is a white, hygroscopic salt with a molar mass of 223.21 g/mol, a density of 2.60 g/mL, and a solubility of around 1000 g/L in water at 35 °C. It is thermally stable to up to 250 °C.

$Mg(NO_3)_2 \cdot 6\,H_2O$ (p.a. ACS, $\geq$ 98%, Carl Roth GmbH + Co. KG (Karlsruhe, Germany)) is a white, hygroscopic salt with a molar mass of 256.4 g/mol, a density of 1.46 g/mL at 20 °C, and a water solubility of 420 g/L at 25 °C. It shows a monoclinic crystal structure and melts around 89 °C.

5.1.3. Solvent Vapor Atmospheres

Different vapor atmospheres in the surrounding of a sample are realized by using the flexible sample environment described in Chapter 4. A continuous flow of nitrogen is streamed into a gas washing bottle filled with a given solvent to produce a solvent saturated nitrogen vapor, which is subsequently guided into one of the measurement chambers described in Sections 4.1.1 and 4.1.2, where the thin film sample is located.

D_2O (99.95%, Deutero GmbH (Kastellaun, Germany)) is used as a solvent to induce the water uptake process of the responsive thin films. D_2O has two main advantages over the use of H_2O. On the one hand, D_2O provides a higher contrast against protonated PNIPMAM in neutron experiments and on the other hand, D_2O is additionally suitable for FTIR measurements. The IR signals of D_2O are at lower wavenumbers than those of H_2O. This results in less signal overlap between the solvent and the polymer. Furthermore, due to the heavier deuterium nucleus, exchange processes such as H/D exchange at the protic amide group of the polymer can be studied. However, due to the presence of H_2O in the ambient air, D_2O readily undergoes H/D exchange, requiring fresh D_2O for each measurement.

The volatile solvent acetone (C_3H_6O, ACS reagent, ≥99.5%, Sigma Aldrich Chemie GmbH (Taufkirchen, Germany)) is used in combination with D_2O to create cononsolvency conditions for the polymer PNIPMAM. The cononsolvency effect induces a macroscopic film contraction of a previously swollen PNIPMAM thin film, which can be followed by *in situ* measurements. Furthermore, the carbonyl group of acetone, which shows a pronounced stretching vibration signal in FTIR, can be used to study interaction mechanisms at the molecular level.

5.1.4. Substrate

Boron-doped silicon wafers with a thickness of 525 ± 25 µm, a diameter of 100 mm, and a resistivity of $10 - 20$ Ωcm (Si-Mat (Kaufering, Germany)) are used as substrates for all prepared samples studied in this thesis. The polished side exposes a (100) crystal orientation and has a roughness of 0.5 nm. Depending on the type of measurement, the round silicon wafers are cut into 1×1 cm^2 pieces for FTIR, 2×2 cm^2 pieces for SR and XRR, and 7×7 cm^2 pieces for ToF-NR experiments.

Silicon substrates offer the possibility to measure FTIR in transmission and SR in reflection mode due to their properties of being transparent for infrared light but reflective for ultraviolet and visible light. While the silicon substrate is in principle transparent to neutrons, the presence of an unpolished side causes neutrons to be at least partially reflected, allowing NR measurements. However, the surface properties of the substrate, such as impurities and surface chemistry, affect the quality of the films produced and their behavior. Therefore, further treatment of the silicon wafer is necessary.

Substrate Cleaning Procedure To clean the surface of the silicon wafers from any organic contaminants and to modify the surface chemistry by creating a hydrophilic SiO_2 surface layer, an acid bath cleaning process followed by oxygen plasma treatment is performed. For the preparation of the acid bath, deionized water (54 mL, 18.2 MΩcm^{-1}, Milli-Q Plus purification system from Merck Millipore (Burlington, USA)) and H_2O_2 (84 mL, 30% aq., Carl Roth GmbH + Co. KG (Karlsruhe, Germany)) are mixed before H_2SO_4 (198 mL, 95-98%, Carl Roth GmbH + Co. KG (Karlsruhe, Germany)) is slowly added. The piranha bath is heated to 80 °C before the silicon substrates are immersed for 15 min. The silicon substrates are then rinsed with deionized water and dried under a continuous nitrogen flow before being exposed to the oxygen plasma. For the oxygen plasma treatment the substrates are placed in the center of a plasma oven (Nano Plasma Cleaner from Diener Electronic (Ebhausen, Germany)). An atmosphere with a pressure of 0.4 mbar O_2 is generated and the plasma treatment is induced by applying a power of

250 W for 10 min. This procedure allows to obtain a hydrophilic surface of the silicon substrate, which is suitable for the formation of attractive polymer-substrate interactions and therefore for the quality of the thin films in terms of homogeneity and uniformity. It should be noted that for the preparation of the FTIR samples, the 1 × 1 cm^2 silicon substrates are treated only with the oxygen plasma protocol and not with the acid bath.

5.2. Fabrication of PNIPMAM Films

The polymer films are fabricated by either using the spin-coating or the drop casting technique. To address the requirements of the applied characterization method, homogeneous and thin films with a low surface roughness are fabricated by using the spin-coating method, while thicker and rougher samples are obtained by using the drop casting method. Both deposition techniques are briefly introduced in the following.

5.2.1. Spin-coating

Spin-coating is a common technique to fabricate uniform thin films from a solution on a flat substrate [173]. Hereby, a solution is deposited on either a spinning (dynamic spin-coating) or a stationary (static spin-coating) substrate. The equilibrium between the centripetal force and the surface tension of the solution, as well as the simultaneous evaporation of the solvent, is used to achieve a uniform coverage of the substrate surface. In general, the film thickness obtained depends on the concentration of the solution, the solvent evaporation rate, the spin speed, the acceleration speed, and the spin-coating time [174].

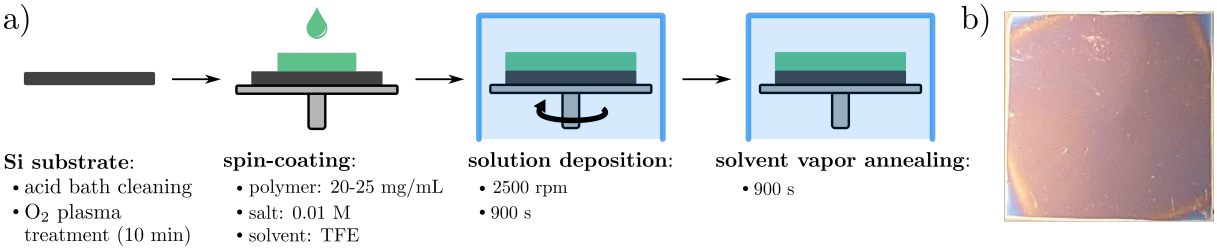

Figure 5.2.: (a) Schematic overview of the spin-coating deposition protocol and (b) image taken of a spin-coated PNIPMAM thin film on a silicon substrate.

The spin-coating protocol used throughout this thesis is shown in Figure 5.2a and an image of a spin-coated PNIPMAM thin film on a silicon substrate is shown in Figure 5.2b. Static spin-coating is performed on a Delta6 RC TT spin-coater (Süss Microtec Lithography GmbH (Garching, Germany)) to fabricate the polymer thin films for the SR, XRR and ToF-NR investigations. For this purpose, stock solutions of the

homopolymer PNIPMAM (50 mg/mL) as well as of the individual salts (0.02 M) are prepared in 2,2,2-trifluoroethanol (TFE, CF_3CH_2OH, ReagentPlus, ≥99%, Sigma Aldrich Chemie GmbH (Taufkirchen, Germany)). From these, either salt-free PNIPMAM or salt-containing PNIPMAM solutions are prepared with a typical polymer concentration ranging between 20 and 25 mg/mL and a salt concentration of 0.01 M. All solutions are filtered by using hydrophobic poly(tetrafluoroethylene) (PTFE) filters (pore size: 0.45 µm, Carl Roth GmbH + Co. KG (Karlsruhe, Germany)) prior to spin-coating. For the 2 × 2 cm^2 sample size, a typical solution volume of 275 µL and for the 7 × 7 cm^2 sample size, a volume of 2 mL is deposited on a pre-cleaned silicon substrate. The samples are then spin-coated with a rotational speed of 2500 rpm for 900 s. Throughout the spin-coating process and for an additional 15 min, the samples are covered under a crystallizing dish (volume: 500 mL, diameter: 115 mm, height: 65 mm, Schott Duran (Germany)) to create a saturated solvent atmosphere. This method helps to slow down the solvent evaporation of the volatile TFE, which prevents uneven layer formation and thus improves the overall thin film quality.

5.2.2. Drop Casting

Drop casting is a simple and fast technique to obtain polymer films in the µm range with a thickness gradient that are suitable for FTIR experiments. A solid film is formed by dropping a solution onto a flat substrate followed by evaporation of the solvent. The obtained film quality and thickness depend mainly on the volume and concentration of the deposited solution and the wetting ability of the substrate. However, it remains a challenge to control the film thickness and uniformity of the films.

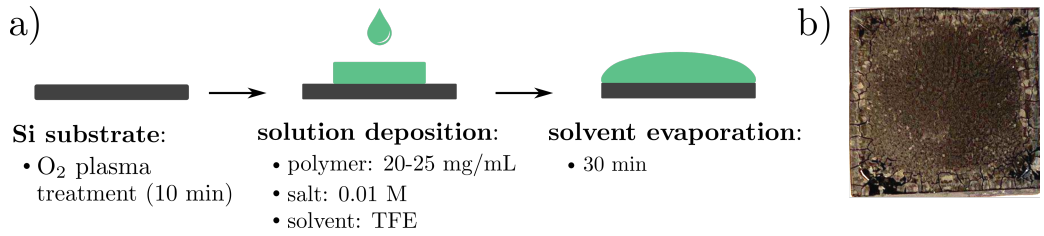

Figure 5.3.: (a) Schematic overview of the drop casting deposition protocol and (b) image taken of a drop casted PNIPMAM thin film on a silicon substrate.

The drop casting protocol used throughout this thesis is shown in Figure 5.3a and an image of a drop casted PNIPMAM thin film on a silicon substrate is shown in Figure 5.3b. All FTIR samples are fabricated using the drop casting technique because the increased thickness and inhomogeneity of the films are advantageous for transmission mode FTIR measurements. This property allows to improve the signal-to-noise ratio as well as to

reduce interference effects due to multiple light reflections within the sample. 1×1 cm^2 oxygen plasma treated silicon substrates are drop cast with a polymer solution with a typical volume of 40 µL after a waiting time of 25 min.

6. Effect of Magnesium Salts with Chaotropic Anions on the Swelling Behavior

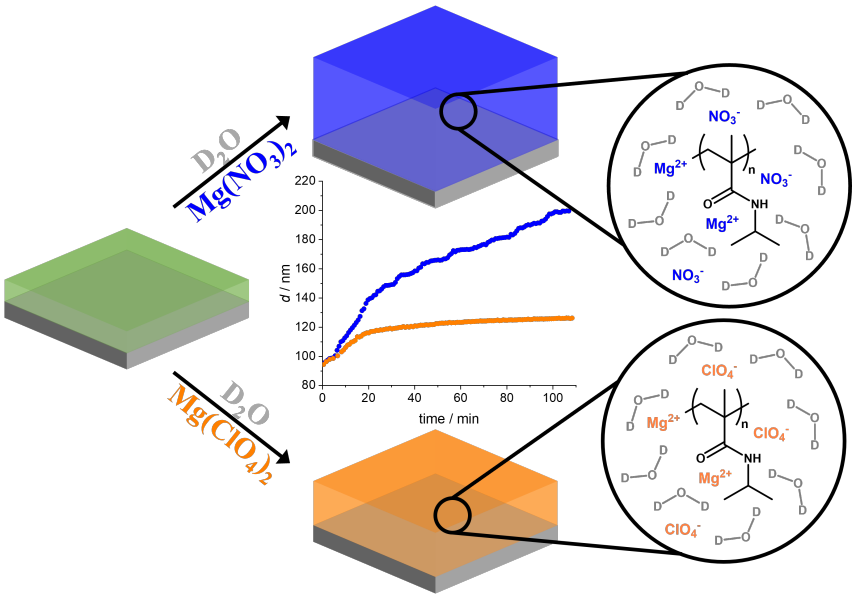

This chapter is based on and reprinted with permission from J. Reitenbach, C. Geiger, P. Wang, A. Vagias, R. Cubitt, D. Schanzenbach, A. Laschewsky, C. M. Papadakis, P. Müller-Buschbaum, Effect of Magnesium Salts with Chaotropic Anions on the Swelling Behavior of PNIPMAM Thin Films, *Macromolecules* 2023, 56, 567-577; DOI: 10.1021/acs.macromol.2c02282. Copyright 2023 American Chemical Society. The raw ToF-NR data is provided by the ILL under DOI: 10.5291/ILL-DATA.9-11-2057.

Poly(*N*-isopropylmethacrylamide) (PNIPMAM) is a stimuli-responsive polymer, which in thin film geometry exhibits a volume phase transition upon temperature increase in water vapor. The swelling behavior of PNIPMAM thin films containing magnesium salts in water vapor is investigated in view of their potential application as nanodevices. Both the extent and the kinetics of the swelling ratio as well as the water content are probed with *in situ* time-of-flight neutron reflectivity (ToF-NR). Additionally, *in situ* Fourier-

transform infrared spectroscopy (FTIR) provides information about the local solvation of the specific functional groups, while 2D FTIR correlation analysis further elucidates the temporal sequence of solvation events. The addition of $Mg(ClO_4)_2$ or $Mg(NO_3)_2$ enhances the sensitivity of the polymer and therefore the responsiveness of switches and sensors based on PNIPMAM thin films. It is found that $Mg(NO_3)_2$ leads to a higher relative water uptake and therefore achieves the highest thickness gain in the swollen state.

6.1. Introduction

Stimuli-responsive polymers open a wide field of applications due to their unique properties [11,12,32,175,176]. For most applications, the polymers require a certain mechanical stability while exhibiting a fast response to the stimuli. This balance between stability and responsiveness can be achieved by using thin films [8,177] and is especially needed when designing nanodevices such as nanoswitches or gas sensors [178–182]. The response of thin films fabricated from stimuli-responsive polymers is shown to derive often from a conformational change, which can be achieved by temperature [14,28,183], light [1,184], ionic strength [6,185], pressure [5], pH [2,186], or by changing the environment [3,187]. An example for a thermoresponsive polymer is poly(*N*-isopropylmethacrylamide) (PNIPMAM), which features a lower critical solution temperature in water at about 44 °C [34,40]. Moreover, PNIPMAM films are capable of temperature-modulated swelling under the influence of surrounding water vapor and exhibit cononsolvency behavior in various water-organic solvent mixtures [83–85]. These properties make PNIPMAM a promising candidate for application in nanodevices, such as nanoswitches or humidity sensors [57,188]. To explore the possibility to tune the swelling capability, the addition of inorganic salts to PNIPMAM thin films is studied. It is hypothesized that the effect of using salt additives may follow the Hofmeister series, which is an empirically found series for cations and anions and describes the ability of ions to induce salting-in or salting-out of proteins in aqueous solution [117]. Later, it was found that other properties such as reaction rates [189], strength of diffusion coefficients [116], colloidal stability [190], and coil-to-globule transitions of thermoresponsive polymers [115] also often follow the Hofmeister series. Until now, the origin of the Hofmeister trend is not yet well understood [23,27,191]. It was found that the effects of the Hofmeister salts are in general more pronounced for anions than for cations [192,193]. The typical order for the anion series, going from kosmotropic to chaotropic, is ${CO_3}^{2-} > {SO_4}^{2-} > {S_2O_3}^{2-} > {H_2PO_4}^{-} > F^{-} > Cl^{-} > Br^{-} \approx {NO_3}^{-} > I^{-} > {ClO_4}^{-} > SCN^{-}$ [24,117,192]. The species to the left of Cl^{-} are referred to as kosmotropes, and those to the right as chaotropes. These terms were originally used to describe the supposed ability of an ion to modify the hydrogen bond network of water. The kosmotropes

are strongly hydrated in water and believed to be water structure makers, which lead to a salting-out effect of macromolecules. In contrast, chaotropes are weakly hydrated and are believed to be water structure breakers, which lead to salting-in. Recent work casts doubt on the idea that the Hofmeister series follows the water network making and breaking properties of salts [20,27,109,117,194–196]. A hypothesis was proposed that direct ion-macromolecule interactions are the major cause of this phenomenon. It was found that the transition temperature of thermoresponsive polymers in aqueous solutions, such as for poly(*N*-isopropylacrylamide) PNIPAM, which is a structural analogue to PNIPMAM and only differs in the absence of a methyl group in the polymer backbone, is greatly influenced by the addition of salts [20,21,115,194]. Depending on the nature of the salt, different interactions occur between the ion pairs and PNIPAM. First, the ions polarize hydrogen-bonded water molecules at the amide group. Second, they can raise the surface tension of the polymer-water interface. Third, the ions can bind directly to the amide moiety [20,21,117]. In any case, salts containing kosmotropic ions increase the miscibility gap of PNIPAM-water mixtures, whereas such containing strongly chaotropic ions tend to decrease the gap.

In the present work, the effect of either added magnesium perchlorate or magnesium nitrate on the swelling behavior of PNIPMAM thin films on silicon substrates in D_2O vapor is investigated by time-of-flight neutron reflectivity (ToF-NR) and Fourier-transform infrared spectroscopy (FTIR). Both salts are strongly hygroscopic, show comparable high solubilities in water (0.4-0.5 M at 25 °C) [197], and dissolve also reasonably well in many polar organic solvents, such as lower alcohols or amides. Moreover, the thin film preparation remains a one-step process and both anions show characteristic signals in the IR spectrum. A 2D FTIR correlation analysis is used to elucidate the hydration mechanism and the order of solvation events. X-ray reflectivity (XRR) measurements are conducted before and after the swelling to get information about potential vertical salt diffusion. This detailed analysis of the underlying mechanism behind the response behavior and the sensitivity of polymer film-based devices is essential for the rational design of tunable polymeric nanoswitches and humidity sensors.

6.2. Results and Discussion

To study the influence of $Mg(ClO_4)_2$ and $Mg(NO_3)_2$ salts on the swelling behavior of PNIPMAM thin films in D_2O vapor atmosphere, the fabricated thin films are exposed to the following experimental protocol. First, the thin films are dried under a continuous nitrogen gas flow for at least 90 min to minimize the number of residual H_2O molecules

inside the films. Subsequently, the films are exposed to a D_2O vapor flow to induce the swelling of the films for 110 min in the case of the ToF-NR measurements and for 20 h in the case of the FTIR measurements. During the experiment the temperature is kept constant at 23 °C. Static ToF-NR measurements provide a detailed vertical polymer and solvent distribution for the dry and the swollen states. Whereas, kinetic ToF-NR measurements track the evolution of the film thickness and the volume fraction of D_2O inside the films during the solvent uptake. Because of their high electron density, the salts scatter X-rays strongly and therefore make XRR measurements a sensible choice. Thus, XRR measurements are performed before and after the swelling experiment under ambient conditions to compare the distribution of the ions vertically throughout the films and to characterize the reversibility of the swelling process. The hydration shell formed around the characteristic functional groups of PNIPMAM and the ions are investigated by analyzing the shifts of the peak positions of *in situ* FTIR spectroscopy measurements. Furthermore, the swelling process is characterized by analyzing the evolution of the integral of the H_2O and the D_2O signals. 2D FTIR correlation analysis is performed to obtain the sequence of the hydration processes of the functional groups. D_2O is chosen rather than H_2O for a higher contrast in the ToF-NR measurements between the solvent and the polymer and because D_2O prevents the overlap between the H−O bending vibration of H_2O and the amide I signal of PNIPMAM in FTIR experiments.

6.2.1. Investigation of Equilibrium States

ToF-NR measurements in the equilibrium states, i.e., dry and swollen states, are carried out for the PNIPMAM thin films containing $Mg(ClO_4)_2$ or $Mg(NO_3)_2$ at two incident angles to measure reflectivity data in a large q_z range (Figure 6.1). Detailed fit results are summarized in Table 6.1.

Table 6.1.: Film thickness d and bulk SLDs obtained from the fits of the static ToF-NR measurements for the $Mg(ClO_4)_2$- and the $Mg(NO_3)_2$-containing PNIPMAM thin films in the dry and swollen state.

PNIPMAM + $Mg(ClO_4)_2$	d / nm	bulk SLD / 10^{-6} Å^{-2}
dry	93.3 ± 0.2	0.80 ± 0.01
swollen	127.9 ± 1.5	3.29 ± 0.01
PNIPMAM + $Mg(NO_3)_2$	d / nm	bulk SLD / 10^{-6} Å^{-2}
dry	93.1 ± 0.1	0.95 ± 0.01
swollen	209.3 ± 0.8	4.22 ± 0.01

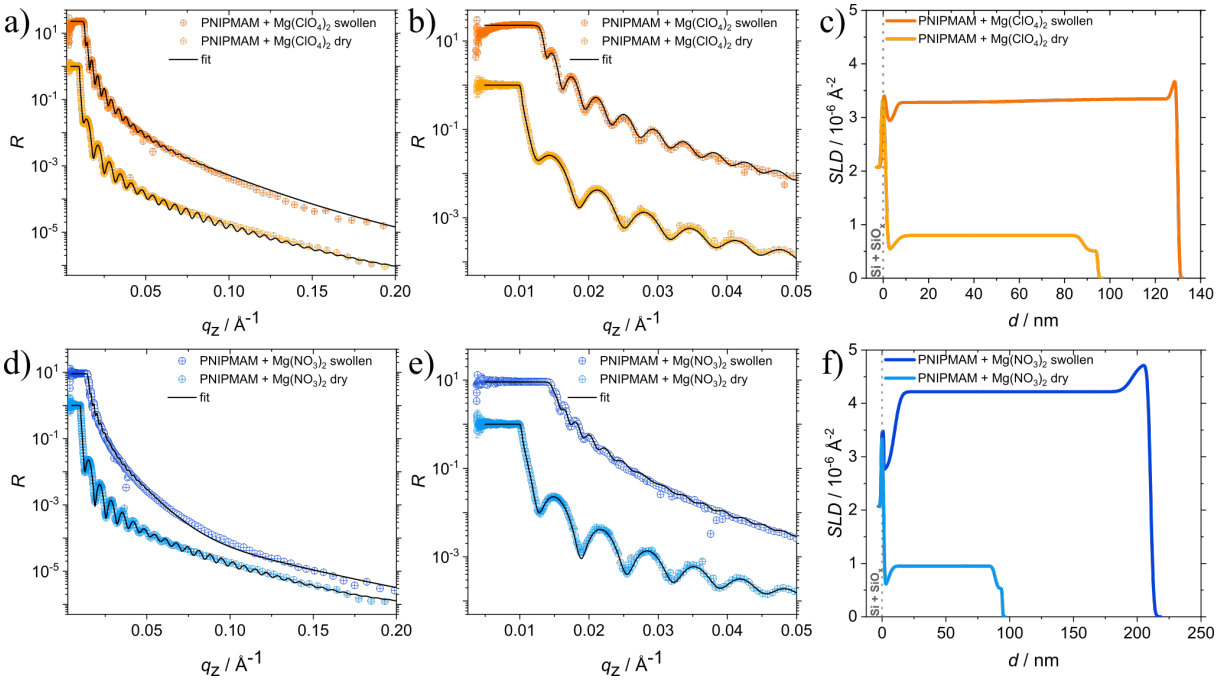

Figure 6.1.: (a,d) Static ToF-NR data (symbols) with fits (black) and (b,e) close-up of the low q_z range of the static ToF-NR curves. The data is shifted along the vertical axis for better visualization. (c,f) Resulting SLD profiles of the PNIPMAM thin films in the dry (lighter color) and the swollen states (darker color) containing $Mg(ClO_4)_2$ (orange) or $Mg(NO_3)_2$ (blue). The dashed vertical line in the SLD profiles at $d = 0$ nm indicates the surface of the silicon substrate. Reprinted with permission from Ref. [167]. Copyright 2023 American Chemical Society.

The fit for the $Mg(NO_3)_2$-containing PNIPMAM film is obtained by applying a six-layer model consisting apart from silicon with its oxide layer and the infinite air layer, of a polymer-substrate interface, a salt-containing polymer layer as bulk, and a polymer-air interface. For the $Mg(ClO_4)_2$-containing PNIPMAM film an additional layer for the bulk region was needed to describe the beating in the pattern of the NR data. For both films, the critical edge shifts toward higher q_z values for the swollen states compared to the dry states, which indicates the incorporation of D_2O. The increased thickness of the swollen films is reflected by the narrowing of the Kiessig fringes compared to the dry state. When going from the substrate to the air interface, the SLD profiles show distinct contributions from the silicon substrate, the covering oxide layer, and the salt-containing polymer thin films. The SLD profiles of the dry states of both films resemble each other closely and show that the film thicknesses are approximately 90 nm. The salt-containing polymer thin films feature a depletion layer at both interfaces, i.e., at the polymer-substrate and at the polymer-air interface. The SLD profiles of the corresponding swollen states show an overall increase in the SLD for both films, further indicating the uptake of D_2O. Different final film thicknesses are obtained for the $Mg(ClO_4)_2$- (130 nm)

and the $Mg(NO_3)_2$-containing (200 nm) PNIPMAM thin films. As indicated by the increased SLD at the polymer-air interface, a D_2O enrichment layer is formed for both films in the swollen state, whereas at the polymer-substrate interface, the SLD decreases (Figure 6.1c, f). Such a lower SLD may be caused by a lower D_2O concentration, a lower salt concentration, or a higher residual H_2O concentration. The key difference between both films is that the nitrate-containing film incorporates higher amounts of D_2O, thereby reaching a 70% higher final film thickness than the perchlorate-containing swollen polymer thin film. The film thickness and the distribution of salts throughout the PNIPMAM thin films before and after the ToF-NR swelling experiments are determined using XRR under ambient conditions. When removing the thin films from the high humidity environment, they go back to their initial state as shown by the comparison of the obtained XRR curves and the corresponding SLD profiles in Figure 6.2. The fits are performed using the six-layer model as described for the ToF-NR measurement.

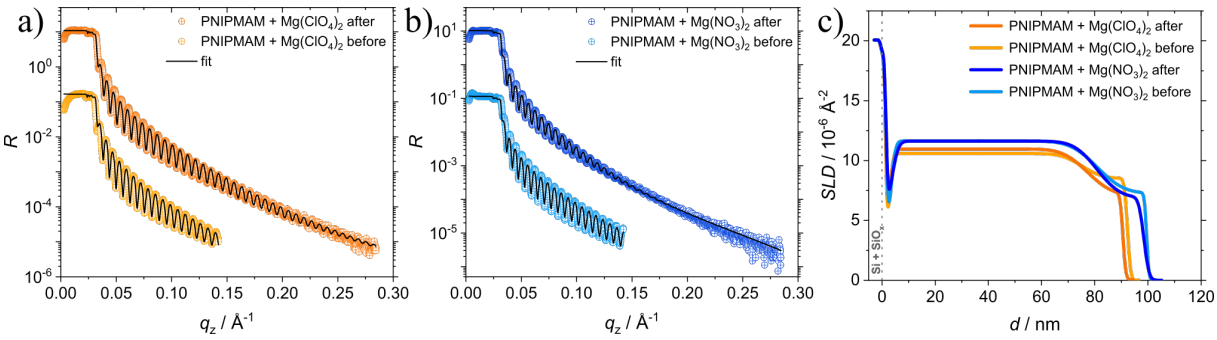

Figure 6.2.: XRR data of the ToF-NR samples before (light color) and after (dark color) the swelling experiments for the (a) $Mg(ClO_4)_2$- (orange) and the (b) $Mg(NO_3)_2$-containing polymer thin film (blue). Fits are shown as black solid lines. The XRR data are shifted along the vertical axis for better visualization. (c) X-ray SLD profiles obtained from the fits of the reflectivity data. Reprinted with permission from Ref. [167]. Copyright 2023 American Chemical Society.

For both the $Mg(ClO_4)_2$- and $Mg(NO_3)_2$-containing PNIPMAM thin films, no major changes in the SLD profile can be detected. This implies that the diffusion of water molecules into the film is not accompanied by the vertical diffusion or migration of the inorganic ions through the thin organic film and additionally confirms the reversibility of the swelling process of the salt-containing polymer thin films. The results also indicate that changes in the neutron SLD profiles in the swollen states (Figure 6.1) are mainly due to the diffusion of D_2O into the thin films and the expulsion and relocation of residual H_2O.

6.2.2. Magnesium Salt Dependent Swelling Behavior

Kinetic ToF-NR measurements are conducted for both salt-containing PNIPMAM thin films to obtain insights about the film thickness and SLD evolution, and thereby about the volume fraction $\phi(t)$ of D_2O inside the respective thin films over the swelling time t (110 min). For the kinetic ToF-NR analysis, the films are modeled with only a single layer to describe the salt-containing polymer bulk on the silicon substrate. Selected kinetic ToF-NR data with their corresponding fits are shown in Figure 6.3a,b. After the first few measurements, a different incident angle is used to prevent detector damage, which results in a slightly different observable q_z range.

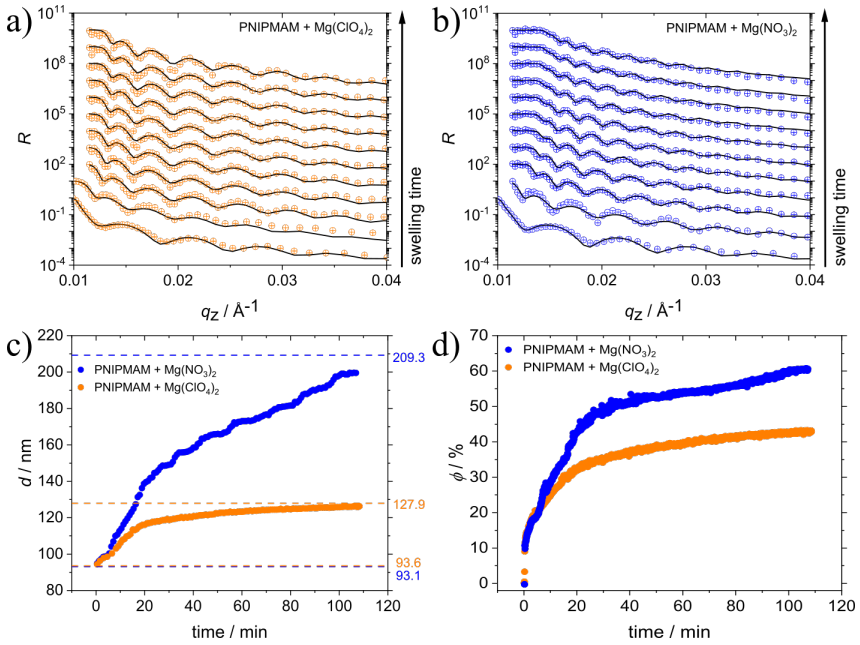

Figure 6.3.: Selected kinetic ToF-NR data (symbols) with their corresponding fits (black) of PNIPMAM thin films containing (a) $Mg(ClO_4)_2$ (orange) or (b) $Mg(NO_3)_2$ (blue) measured during the swelling experiment with D_2O. Temporal evolution of (c) the film thicknesses and (d) volume fraction $\phi(t)$ of D_2O within the films. The dashed lines in black, orange, and blue colors in panel (c) indicate the corresponding thickness d obtained from the static ToF-NR measurements for the dry and swollen states. The data shown in subfigures (a,b) are shifted along the vertical axis for better visualization. Reprinted with permission from Ref. [167]. Copyright 2023 American Chemical Society.

The kinetic ToF-NR data of both salt-containing PNIPMAM thin films show a similar behavior. The critical edges shift toward higher q_z values since the overall SLD of the system increases, and the spacing of the Kiessig fringes decreases over time due to an increase in the film thickness. These observations indicate that D_2O is incorporated into the thin films and that the thicknesses increase over time. The temporal evolution of the

film thickness (Figure 6.3c) and the D_2O volume fraction $\phi(t)$ (Figure 6.3d) are extracted from the fits of the kinetic ToF-NR data. It turns out that the nitrate-containing polymer thin film reaches a higher film thickness in the bulk layer over the same swelling time. The dashed lines highlight the results obtained from the static ToF-NR measurements for the dry and swollen states for both salt-containing PNIPMAM thin films. For the perchlorate-containing films, the initial and final film thickness of the static and kinetic ToF-NR measurements are in good agreement. In contrast, for the nitrate-containing films, the final thickness obtained during the kinetic measurement over 110 min does not quite reach the thickness obtained from the static measurement, which is conducted for 45 min immediately after the kinetic measurement, but is by about 10 nm short (i.e., by 10-15% of the maximum swelling increase). The latter means that an equilibrium state is not reached during the duration of the swelling experiment. The time-dependent D_2O volume fraction $\phi(t)$ as a function of swelling time t is calculated by taking the difference between the measured SLDs at a given swelling time, $SLD_{\mathrm{meas}}(t)$, and the SLD of the dry film, SLD_{dry}, divided by the difference between the SLDs of D_2O, $SLD_{\mathrm{D_2O}}$, and the dry film

$$\phi(t) = \frac{SLD_{\mathrm{meas}}(t) - SLD_{\mathrm{dry}}}{SLD_{\mathrm{D_2O}} - SLD_{\mathrm{dry}}} \,. \tag{6.1}$$

The nitrate-containing polymer thin film exhibits a higher D_2O uptake (thickness increase by about 115 nm) than the perchlorate-containing polymer thin film (thickness increase by about 35 nm) and reaches a D_2O volume fraction of more than 60% (Figure 6.3d). This difference is remarkable as both salts are strongly hygroscopic, form hexahydrates, and have nearly the same molar solubility in water at ambient temperature.

6.2.3. Interactions on Molecular Level

The molecular interactions and exchange mechanisms during the uptake of D_2O into the films are investigated using *in situ* FTIR measurements. The change in the peak areas and the shift of peak positions can elucidate the hydration mechanism of the polymer and, possibly, of additional compounds. However, the analysis of FTIR data can be challenging due to the presence of overlapping signals originating from different functional groups. Furthermore, because FTIR has sample requirements different from those of the reflectivity measurements, thicker films and longer measurement times are used, as explained in Section 5.2.2. Therefore, a detailed analysis of the FTIR spectra is fundamental. In Figure 6.4, the normalized FTIR spectra, which are conducted during the swelling process, are plotted for a PNIPMAM thin film free of salt (Figure 6.4a), for a PNIPMAM

thin film containing $Mg(ClO_4)_2$ (Figure 6.4b), and for a PNIPMAM thin film containing $Mg(NO_3)_2$ (Figure 6.4c).

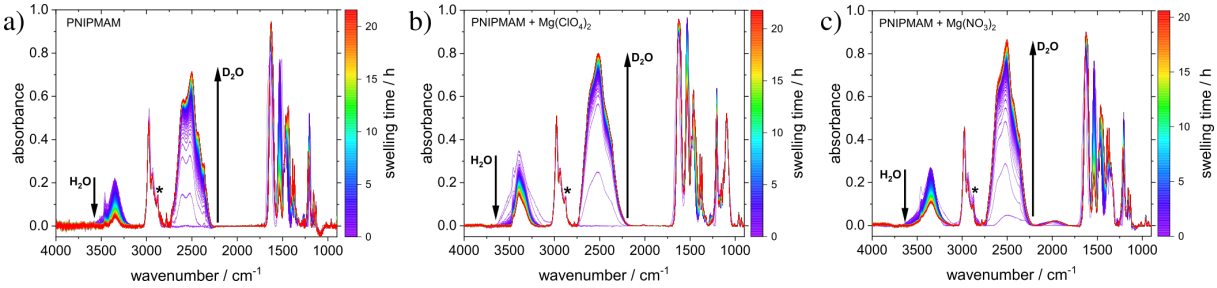

Figure 6.4.: *In situ* FTIR spectra (color scale purple to red) measured during the swelling process in D_2O vapor of (a) a pure PNIPMAM thin film, (b) a PNIPMAM thin film containing $Mg(ClO_4)_2$, and (c) a PNIPMAM thin film containing $Mg(NO_3)_2$. The spectra are normalized by setting the symmetric stretching vibration of the isopropyl group ($\nu_{sym}(C-H_3)$, marked with an asterisk (*)) of the dry state of all systems to an absorbance of 0.14. Black arrows demonstrate the evolution of the peaks of the D−O and H−O stretching vibrations over time. Reprinted with permission from Ref. [167]. Copyright 2023 American Chemical Society.

After drying the films in a nitrogen gas flow for at least 90 min, D_2O vapor is introduced into the sample environment, which induces the swelling process. For all sample types, this is reflected by an increase in the signal of the D−O stretching vibration at around 2500 cm^{-1}. On the contrary, the H−O stretching vibration at around 3370 cm^{-1} simultaneously decreases, indicating that residual H_2O molecules leave the film and are replaced by D_2O molecules. This behavior is also reflected by the evolution of the peak areas of the corresponding ν(D−O) and ν(H−O) signals over the swelling time, which are shown in Figure 6.5a and Figure 6.5b, respectively.

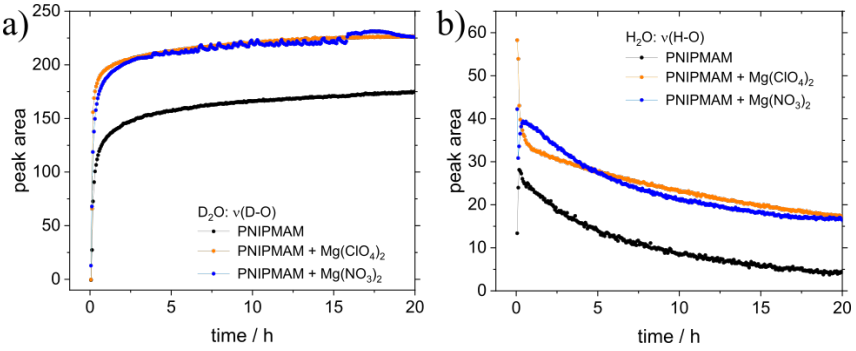

Figure 6.5.: Evolution of the peak areas of (a) the ν(D−O) and (b) the ν(H−O) signals (pure PNIPMAM film: black; $Mg(ClO_4)_2$-containing PNIPMAM film: orange; $Mg(NO_3)_2$-containing PNIPMAM film: blue) over time. Reprinted with permission from Ref. [167]. Copyright 2023 American Chemical Society.

It is noted that the water content is considerably lower for the pure PNIPMAM film (both H_2O and D_2O) than for the films containing salt. Furthermore, the peak areas in the region of the ν(H−O) signals never reach values of zero as the signals from the N−H group are also present in this spectral region. Since a different sample environment with a different configuration and thicker films is used to measure the *in situ* FTIR data, no direct comparison with the ToF-NR measurements is possible. Nevertheless, the *in situ* FTIR measurements imply that the PNIPMAM film devoid of salt takes up significantly fewer D_2O molecules than the samples containing the magnesium salts. Since the polymer bares a protic functional group, H/D exchange can occur at the N−H function of the amide group [198]. However, this phenomenon is not observed since no additional signal, i.e., the development of a N−D signal, is detected. The N−D signal would be expected at lower wavenumbers than the N−H signal (amide II) at approximately 1460 cm^{-1} as shown for PMMA-*b*-PNIPAM [187]. To investigate the hydration shells forming around the functional groups in the respective systems, the individual peak position shifts of the characteristic signals of the polymer and salts are analyzed. Figure 6.6 shows the peak position shifts during the swelling process for the amide I (1645 cm^{-1}), the amide II (1515 cm^{-1}), and the ν_{asym}(C−H_3) (2972 cm^{-1}) signals, originating from functional groups of the polymer.

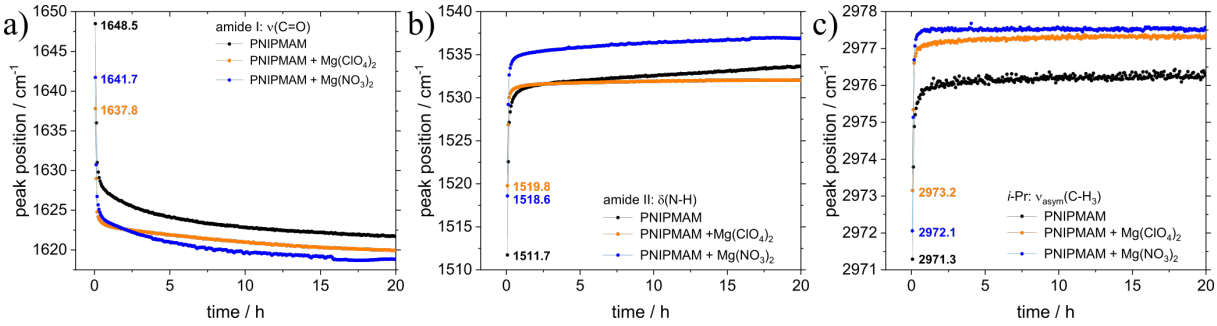

Figure 6.6.: Peak positions of (a) the amide I, (b) the amide II, and (c) the ν_{asym}(C−H_3) signals (pure PNIPMAM film: black; $Mg(ClO_4)_2$-containing PNIPMAM film: orange; $Mg(NO_3)_2$-containing PNIPMAM film: blue) over time. The initial peak positions of the dry films are highlighted by displaying the values in the respective colors. Reprinted with permission from Ref. [167]. Copyright 2023 American Chemical Society.

The comparison of the initial peak positions of the amide I and the amide II signal in the dry states for all investigated films reveals a shift of these signals when adding the different magnesium salts. This finding suggests the formation of ion-polymer complexes at the amide group, which may be explained by weak coordination bonds and/or by ion-dipole interactions between the polymer carbonyl group and the Mg^{2+} ions [199–204]. Furthermore, a peak shift is observed for the hydrophobic isopropyl group shown exemplarily for

the $\nu_{asym}(C-H_3)$ signal with <5 cm^{-1}, which is considerably smaller than the ones observed for the amide signals. The overall evolution of the peak position of the amide I signal shows a shift of about 30 cm^{-1} toward lower wavenumbers during the swelling time in D_2O vapor. This trend reveals that a hydration shell, formed by hydrogen bonds between the amide groups and D_2O molecules, builds up during the swelling process. Since the amide II signal is a deformation band and not a stretching vibration, the opposite direction of the peak position shifts is obtained during hydration. The peak positions of the signal of the hydrophobic isopropyl group shift by 5-7 cm^{-1} toward higher wavenumbers, indicating the formation of a hydration shell around the hydrophobic groups as well. It is assumed that this shift originates from a reduced amplitude of the vibration due to the compact hydration shell forming around this functional group. To conclude, similar trends of the peak areas and peak positions for the pure PNIPMAM and the salt-containing PNIPMAM thin films are observed and the polar as well as the nonpolar groups get hydrated when the films are exposed to water vapor. Both anions of the magnesium salts are IR-active, which gives *a priori* the possibility to obtain information about the hydration behavior of the anions of the salts dispersed in the films as well. However, the investigation of the nitrate anion ($\nu_{asym}(NO_3^-) \approx 1325$ cm^{-1}) is hampered by the fact that its IR signals overlap with signals from the polymer. Still, the asymmetric stretching vibration of the perchlorate anion around 1093 cm^{-1} can be clearly distinguished from the signals arising from the polymer itself. Figure 6.7 illustrates the evolution of the peak position of the $\nu_{asym}(ClO_4^-)$ signal over the swelling time.

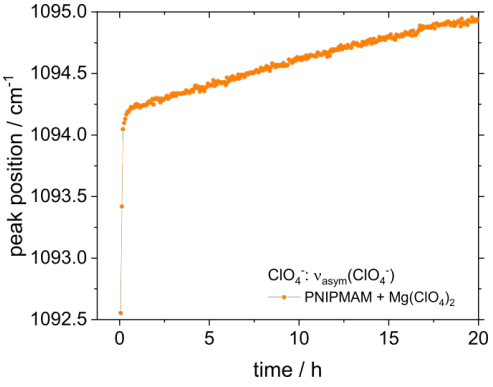

Figure 6.7.: Evolution of the peak position of the asymmetric stretching vibration of the ClO_4^- anion over time. Reprinted with permission from Ref. [167]. Copyright 2023 American Chemical Society.

Over the swelling time, a shift by 2-3 cm^{-1} toward higher wavenumbers is observed, indicating that a hydration shell of D_2O molecules is forming around the ClO_4^- anion. As shown previously, the peak area of the $\nu(D-O)$ signal suggests that an equilibrium swollen state is reached at the end of the swelling time (see Figure 6.5). However, the peak posi-

tion of the ClO_4^- group has not yet reached its threshold, meaning that, most likely, the anion has not reached yet the equilibrated hydration state. To obtain further insights into the hydration mechanism and the sequence of solvation events and to resolve overlapping signals, 2D FTIR correlation analysis is performed, which is explained in Section 3.4 and in more detail in the literature by Noda [165,205]. Different from polymers in solution, polymer thin films in combination with the custom-built flexible sample environment described in Section 4, enables to elucidate the hydration mechanism by gradual addition of the solvent by the generation of a solvent vapor atmosphere. First, the sequence of events of the hydration of the hydrophobic moieties, such as the isopropyl group at the side chain of the polymer and the polymer backbone, is investigated by analyzing the synchronous as well as the asynchronous 2D FTIR correlation plots, which are shown in Figure 6.8 for the pure PNIPMAM film. Here, only the first 10 spectra taken in the interval from 0 to 35 min are considered because the most significant changes occur in this time frame. Correlation plots with the complete spectra series are provided in Figure A.2.

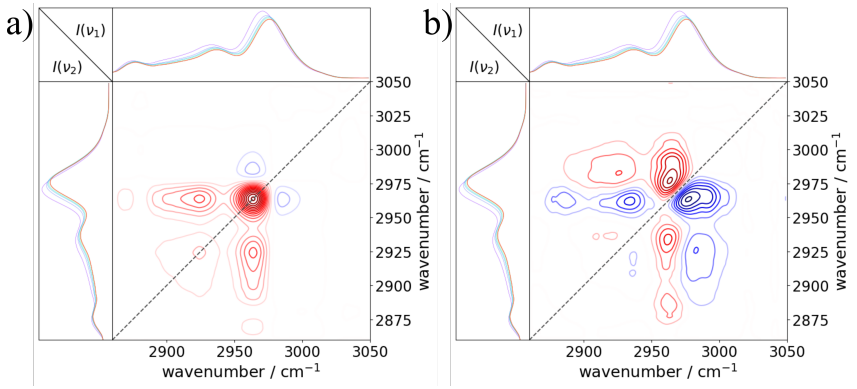

Figure 6.8.: (a) Synchronous and (b) asynchronous 2D FTIR correlation plots of the pure PNIPMAM film in the wavenumber range between 2860 and 3050 cm^{-1} for the signals of $\nu_{asym}(C-H_2)$, $\nu_{asym}(C-H_3)$, and $\nu_{sym}(C-H_3)$ originating from the isopropyl group of the side chain and the polymer backbone for the first 10 spectra taken in the interval from 0 to 35 min. Areas colored in red indicate positive correlation, and areas colored in blue indicate negative correlation. Reprinted with permission from Ref. [167]. Copyright 2023 American Chemical Society.

The synchronous 2D FTIR correlation plot reveals that the $\nu_{asym}(C-H_3)$ signal at approximately 2970 cm^{-1} shows a strong autopeak, which implies that during the hydration of this functional group, a large difference in the signal intensity is observed. For the methylene signal $\nu_{asym}(C-H_2)$ of the polymer backbone at around 2930 cm^{-1}, the autopeak is less pronounced. The crosspeak of these signals has a positive sign, meaning that the intensities of both signals are either increasing or decreasing together. By investigating the asynchronous correlation plot, a negative correlation at this position (2970 and 2930 cm^{-1}) is observed. Therefore, the intensity change of the $\nu_{asym}(C-H_2)$ vibra-

tion occurs predominantly after the change of the $\nu_{asym}(C-H_3)$ vibration, which in turn means that the isopropyl group in the side chain is hydrated before the polymer main chain. This order of hydration is in agreement with observations for PNIPAM in solution during temperature changes. Conceptually, heating is associated with dehydration of the polymer while cooling leads to a rehydration [206]. Therefore, the process of D_2O uptake can be compared qualitatively to a cooling process. Based on the correlation plots of the salt-containing films, the order of hydration is not affected by the addition of salt (see Figures A.1 and A.2).

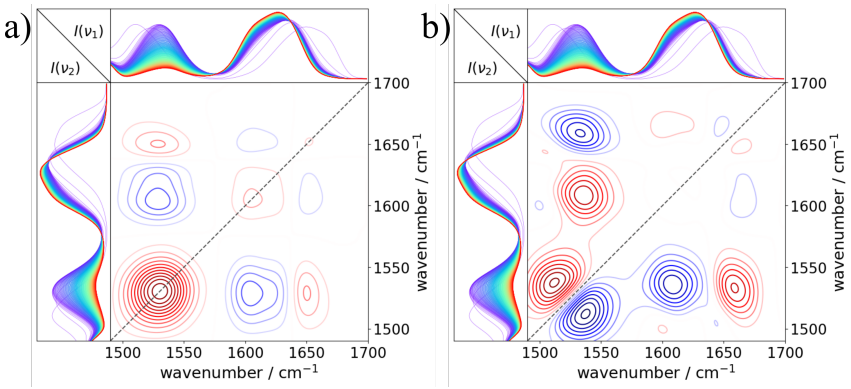

Figure 6.9.: (a) Synchronous and (b) asynchronous 2D FTIR correlation plots of the pure PNIPMAM film in the wavenumber range between 1490 and 1700 cm^{-1} for the amide I and the amide II signals. Areas colored in red indicate positive correlation, and areas colored in blue indicate negative correlation. Reprinted with permission from Ref. [167]. Copyright 2023 American Chemical Society.

By analyzing the 2D FTIR correlation plots of the signals coming from the polar amide groups, as shown in Figure 6.9 for the pure PNIPMAM film, it becomes evident that both signals show strong autopeaks, with the autopeak stemming from the amide II band being more pronounced (Figure 6.9a). The crosspeak in the synchronous correlation plot between the amide I and the amide II signals at 1650 and 1510 cm^{-1}, respectively, is negative, meaning that the amide I signal is increasing while the amide II signal is decreasing. The crosspeak at the same position in the asynchronous correlation plot (Figure 6.9b) has a positive sign, signifying that the amide I signal is changing before the amide II signal. On closer inspection of the amide I signal, it is seen that during the hydration a shoulder at lower wavenumbers is appearing. This is also seen in the correlation plots as a splitting of the amide I signal. Based on investigations for PNIPAM in solution, this shoulder is believed to represent the intermolecular polymer solvent C=O···D−OD hydrogen bond, while the peak at higher wavenumbers is attributed to the inter- and intramolecular C=O···H−N hydrogen bonds of the amide groups with each other [207,208]. This observation reveals that the amide-based polymer-polymer interactions are replaced

with interactions with the solvent during the hydration. This is also true for the salt-containing PNIPMAM films. To further assign an order of hydration events, the amide I and amide II signals are correlated with the signals coming from the hydrophobic groups of the side chain as well as the polymer backbone. In Figure 6.10, the synchronous and the asynchronous correlation plots are shown for the pure PNIPMAM film.

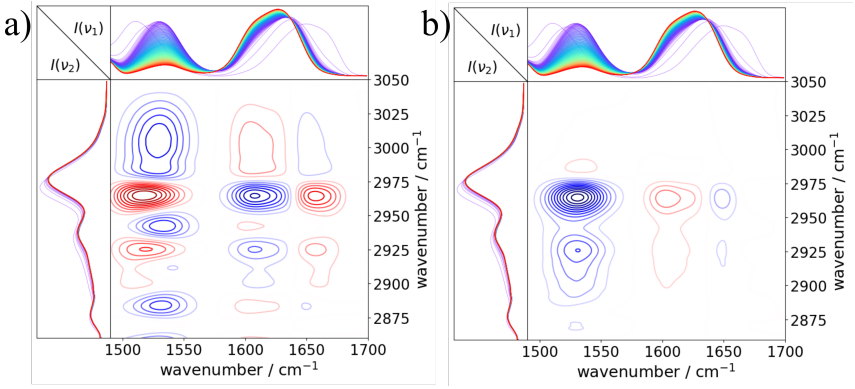

Figure 6.10.: (a) Synchronous and (b) asynchronous 2D FTIR correlation plots of the pure PNIPMAM film in the wavenumber range between 1490 and 1700 cm^{-1} and between 2860 and 3050 cm^{-1} for the amide I, amide II, $\nu_{asym}(C-H_3)$, $\nu_{asym}(C-H_2)$, and $\nu_{sym}(C-H_3)$ signals. Areas colored in red indicate positive correlation, and areas colored in blue indicate negative correlation. Reprinted with permission from Ref. [167]. Copyright 2023 American Chemical Society.

The synchronous correlation plot shows positive correlation peaks between the amide II and the $\nu_{asym}(C-H_3)$ signals as well as between the amide II and the $\nu_{asym}(C-H_2)$ signals (1635, 2973, and 2930 cm^{-1}), whereas the asynchronous correlation plot at these positions shows negative correlation peaks. This means that the N−H functional group of the amide is hydrated after the hydrophobic moieties. The sequence is the same for the carbonyl group (amide I). Therefore, an unambiguous hydration order can be deduced: $\nu_{asym}(C-H_3) > \nu_{asym}(C-H_2) >$ amide I $>$ amide II. Interestingly, aprotic and nonpolar alkyl groups appear to be hydrated before the protic and polar amide functional groups. A possible explanation for this behavior is that in order for the amide functional groups to be solvated, the isopropyl groups as well as the hydrophobic backbone of the polymer need to be hydrated before the amides to become accessible to the solvent. This hypothesis is supported by the observation that the shoulder in the amide I signal, corresponding to the amide-solvent interactions, only develops after a certain time delay, which is the initial onset time that is needed for the hydration of the hydrophobic groups. In other words, the steric hindrance by the alkyl groups and the fact that amide-amide hydrogen bonds are energetically favorable causes the amide groups to be hydrated last. To investigate the role of the salts especially of their IR-active anions on the hydration process, signals

of the asymmetric stretching vibration of the ClO_4^- group are correlated with the polar amide groups as well as with the hydrophobic groups. The corresponding synchronous and asynchronous correlation plots are shown in Figure 6.11 of the $Mg(ClO_4)_2$-containing PNIPMAM film. Again, only the first 10 spectra from the spectra series are taken into account because the significant changes occur in this time frame. Correlation plots with the whole spectra series are provided in Figure A.5.

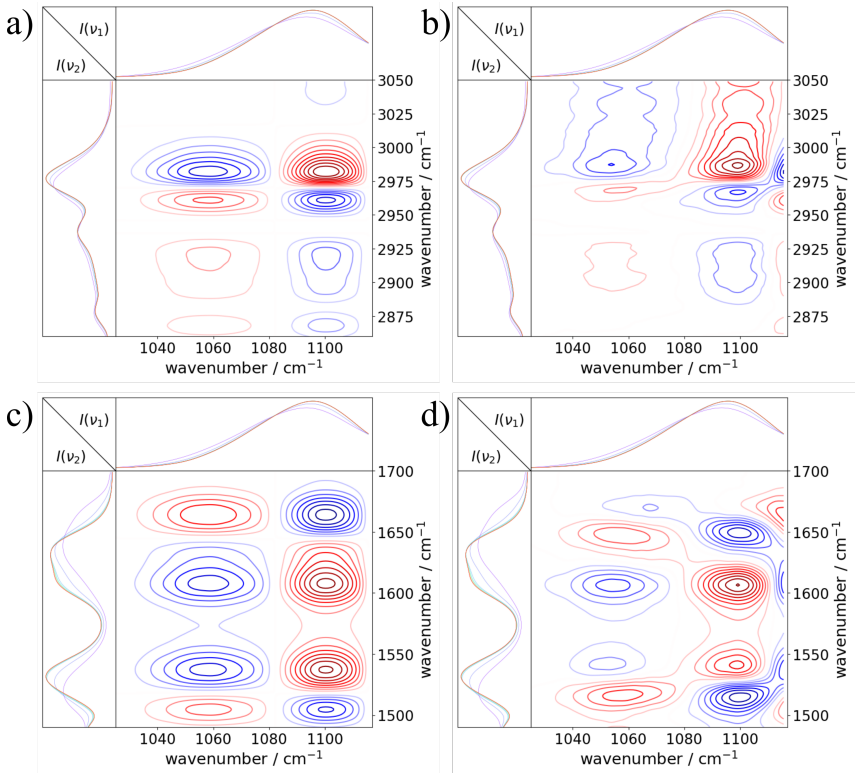

Figure 6.11.: (a,c) Synchronous and (b,d) asynchronous 2D FTIR correlation plots of the $Mg(ClO_4)_2$-containing PNIPMAM film in the wavenumber range between 1030 and 1130 cm^{-1} and between 2860 and 3050 cm^{-1} (top) as well as well as between 1030 and 1130 cm^{-1} and between 1490 and 1700 cm^{-1} (bottom) for the $\nu_{asym}(ClO_4^-)$, $\nu_{asym}(C-H_3)$, $\nu_{asym}(C-H_2)$, $\nu_{sym}(C-H_3)$, amide I, and amide II signals for the first 10 spectra taken in the interval from 0 to 35 min. Areas colored in red indicate positive correlation, and areas colored in blue indicate negative correlation. Reprinted with permission from Ref. [167]. Copyright 2023 American Chemical Society.

The synchronous and asynchronous correlation plots reveal that the sign of the correlation peaks between the $\nu_{asym}(ClO_4^-)$ signal and the $\nu_{asym}(C-H_3)$ and $\nu_{asym}(C-H_2)$ signals is positive. This indicates that the perchlorate anion is solvated before even the alkyl groups. The same is true for the amide functional group. Thus, the hydration order is $\nu_{asym}(ClO_4^-) > \nu_{asym}(C-H_3) > \nu_{asym}(C-H_2) >$ amide I $>$ amide II. The situation is the same for the nitrate-containing PNIPMAM film. However, the analysis of the $Mg(NO_3)_2$-

containing PNIPMAM film is complicated by the fact that the signal coming from the asymmetric stretching vibration of the nitrate is overlapping with symmetric deformation bands from the alkyl groups. The corresponding correlation plots are provided in Figure A.6.

To conclude, with the aid of 2D FTIR correlation analysis, the stepwise hydration mechanism of PNIPMAM thin films is elucidated. This highlights the attractiveness of using polymer thin films for mechanistic studies. This is the case because the response of the polymer to solvation can be monitored *in situ* by gradual addition of solvent vapor. Furthermore, the influence of salts on the hydration mechanism can be investigated by using IR-active ions with distinct signals in the spectra. As discussed above, first, the ions, which reside in-between the polymer chains, are solvated followed by the hydrophobic alkyl groups from the polymer side chain and backbone. After the polymer network is loosened up by the initial uptake of water molecules, the previously sterically hindered amide groups become solvated. Combining the findings from the ToF-NR and the FTIR analysis, the mechanism can be subdivided into two stages. In the first stage, a high initial uptake of water molecules is observed, which is accompanied by a strong increase in film thickness. Mechanistically, this is associated with the hydration of the ions and the formation of a water shell around the hydrophobic alkyl groups, which renders the amide groups solvent-accessible. In the second stage, the initial water network slowly rearranges into a thermodynamically favored equilibrium state, which is reflected by the fact that the film approaches a limited thickness.

6.3. Conclusion

PNIPMAM thin films containing magnesium salts with chaotropic anions are investigated for their potential application as nanoswitches or humidity sensors. The reversibility of the switching, which is essential for applications, is confirmed by XRR measurements before and after the swelling experiments. Furthermore, it is shown that the addition of magnesium salts greatly enhances the final swelling ratio, which indicates that the salts can be used to modulate the sensitivity of such switches and sensors. Although both anions are monovalent chaotropes, which are more weakly hydrated than kosmotropes, we find that magnesium nitrate leads to a higher water uptake and therefore a higher film thickness is reached in the swollen state. This is in accordance with the empirical observation that nitrate is less chaotropic and therefore better hydrated than perchlorate. By investigating the *in situ* FTIR spectra, the extent and kinetics of hydration of the functional groups of the polymer as well as the solvation of the ions is elucidated. Moreover, the sequence

of hydration events is determined through 2D FTIR correlation analysis. First, the ions are solvated, which leads to an initial drastic increase in film thickness. This is followed by the hydrophobic alkyl groups of the polymer. Only once the hydrophobic moieties are hydrated, the amide groups become solvent-accessible, which finally leads to the formation of the equilibrium swollen state through a slow rearrangement of the polymer chains. The latter is reflected by the fact that only after several hours, the equilibrium thickness is reached. Finally, in light of future applications, the addition of salts provides an environmentally friendly and simple to realize modification for fine tuning the sensitivity and response behavior of nanoswitches and sensors.

7. Salt-Mediated Tuning of the Cononsolvency Response Behavior

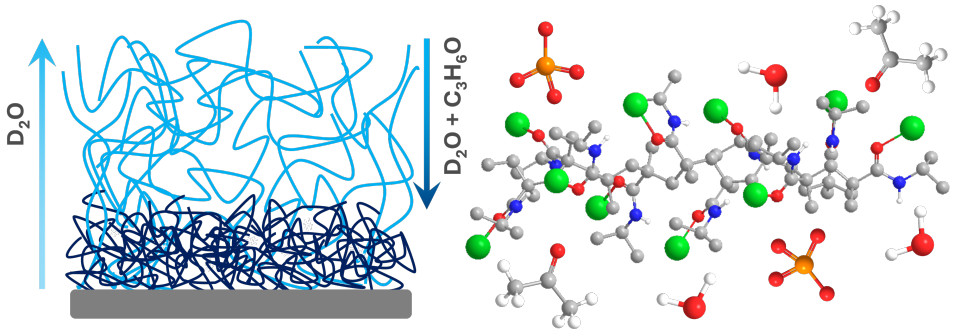

This chapter is based on and reprinted with permission from J. Reitenbach, P. Wang, L. F. Huber, S. A. Wegener, R. Cubitt, D. Schanzenbach, A. Laschewsky, C. M. Papadakis, P. Müller-Buschbaum, Salt-Mediated Tuning of the Cononsolvency Response Behavior of PNIPMAM Thin Films, *Macromolecules* 2024, 57, 10635-10647; DOI: 10.1021/acs.macromol.4c02053 licensed under CC BY 4.0. The raw ToF-NR data is provided by the ILL under DOI: 10.5291/ILL-DATA.9-11-2093.

The development of tuning parameters to influence the response behavior of polymer-based nanodevices is investigated by the addition of $NaClO_4$ or $Mg(ClO_4)_2$ to adjust the swelling degree of poly(*N*-isopropylmethacrylamide) (PNIPMAM) thin films under different vapor atmospheres. By leveraging the cononsolvency effect of the polymer in a mixed vapor of water and acetone, a contraction of the preceding water-swollen films is induced. The relation between the macroscopic and the molecular processes is elucidated by static and time-resolved time-of-flight neutron reflectivity, as well as by *in situ* Fourier-transform infrared spectroscopy. It is found that the addition of $NaClO_4$ strongly enhances the film thickness response for swelling and contraction, which, therefore, allows the tuning of the film toward stronger responses. Mechanistically, D_2O-amide bonds are formed during the swelling and become perturbed upon vapor exchange. Thereby, the D_2O-amide interactions are reduced continuously, while acetone-amide interactions develop, accompanied by increasing amide-amide interactions during the film contraction.

7.1. Introduction

Amidst the various types of stimuli-responsive materials [7,12,209], thermoresponsive polymers have attracted particular attention [36,210–212]. Characteristically, the temperature-induced changes in their hydrophilicity can be translated into a coil-to-globule transition that dramatically affects their water solubility and aggregation behavior. Mostly, two different scenarios are exploited. Either the polymer becomes soluble with increasing temperature, for which the related transition is characterized by an upper critical solution temperature (UCST), or the polymer becomes insoluble at higher temperatures, and the resulting phase transition is characterized by a lower critical solution temperature (LCST) [15,213,214]. The driving force behind the thermoresponsivity of polymers reflects the thermodynamical preference of interactions between the polymer and the solvent molecules compared to the sum of interactions between the polymer chains and between the solvent molecules themselves [42,58,215]. Besides depending on the intrinsic features of the polymer, such as molar mass, tacticity, and end groups, the transition temperature can be modified by additives that modulate the inter- and intramolecular interactions [27,216–218]. In certain cases, adding an organic cosolvent, which is also a good solvent for the polymer, can lead to a variation of the LCST with a distinct minimum at a certain composition of the solvent mixture [3,59,86,219]. At a given temperature, a miscibility gap is observed for a certain range of compositions of the solvent mixture. This intriguing phenomenon is known as the cononsolvency effect, for which the detailed origins are still under debate [3,9,219]. The theories put forward range from explanations based on intrinsic properties to preferential interactions between specific constituents of the system [60,71,75,87,89,92,93,220–222]. In addition to theoretical studies and computer simulations, experimental investigations allow to obtain insights into influencing factors, and a number of different polymers, cosolvents, and sample architectures have been investigated [84,86,187,221,223–229]. To further leverage the cononsolvency effect in devices, polymers in thin film geometry are attractive candidates due to their fast response, mechanical stability, and easy fabrication compared to polymers in solution or polymer brushes [8,177]. Most of the reported cases concern polymers in aqueous media and have been carried out on the same polymer, namely, poly(*N*-isopropylacrylamide) (PNIPAM). Structurally related to the well-studied PNIPAM is poly(*N*-isopropylmethacrylamide) (PNIPMAM), which in aqueous solution not only shows LCST-type II behavior like PNIPAM but also exhibits a cononsolvency effect in a number of solvent mixtures [40,81–86,229]. Furthermore, in thin film geometry, PNIPMAM is amorphous and has a high water-uptake ability, and due to the additional methyl group on the backbone, PNIPMAM thin films feature a higher glass transition temperature and are more resistant to hydrolysis [86]. In previous studies, it was found

that for diblock copolymer thin films consisting of a short poly(methyl methacrylate) (PMMA) and a PNIPAM [187] or a PNIPMAM block [83] strong deviations in the response behavior toward different vapor atmospheres occur, despite the difference in only a methyl group in the polymer backbone. For the PMMA-*b*-PNIPMAM thin films, an overall stronger increase in film thickness upon water vapor atmosphere exposure was obtained as well as a pronounced, abrupt contraction under exchange to a water-acetone vapor atmosphere. Since hydrogel-based devices rely on detection mechanisms that have to adapt to the volume or weight of the thin polymer film, a fast and strong response to an external trigger is crucial [128]. To circumvent the laborious tailored synthesis of new polymers, which specifically meet the requirements imposed by the respective application, the ability to modify the response behavior of already established polymers, such as simple homopolymers, will be very valuable. It is known that specific ion effects impact various phenomena, such as solvent interactions or the LCST of thermoresponsive polymers [20,21,113,216,230]. In this regard, the addition of salts in the fabrication process of polymer thin films should provide an easy route to tuning the response behavior of polymer thin films.

In the present study, the cononsolvency behavior of PNIPMAM homopolymer thin films is modulated with the addition of two different perchlorate salts, namely, $NaClO_4$ and $Mg(ClO_4)_2$. As demonstrated previously [167], adding a Mg salt with a chaotropic anion enables the modification of the swelling behavior of PNIPMAM thin films in a D_2O vapor atmosphere. In the present study, $NaClO_4$ and $Mg(ClO_4)_2$ are chosen on the one hand to be able to make comparisons to the previous study and to, on the other hand, have a more chaotropic cation in the form of Na^+. Therefore, here the influence of the cation is analyzed, and the investigation of tuning not only the swelling but also the collapse response is motivated. The cononsolvency effect of PNIPMAM hydrogel films is induced by switching from a pure D_2O vapor atmosphere to a mixed D_2O-acetone vapor atmosphere with a volume-to-volume ratio of 9:1, which is known to induce the cononsolvency effect in PNIPMAM-based diblock copolymers [83,85]. The evolution of the thickness and the solvent content inside the thin films is investigated by time-of-flight neutron reflectivity (ToF-NR). In addition, *in situ* Fourier-transform infrared spectroscopy (FTIR) measurements are conducted to obtain insights into the solvation processes of the individual components. The sequence of solvation events is further determined by the analysis of selected IR bands to provide further understanding of the complex kinetic processes during water uptake and cosolvent-induced water release.

7.2. Results and Discussion

To study the solvent vapor mixture-induced contraction of PNIPMAM-based thin films with the addition of different salts, namely, $NaClO_4$ or $Mg(ClO_4)_2$, time-of-flight neutron reflectivity (ToF-NR) and Fourier-transform infrared spectroscopy (FTIR) measurements are combined. Before the ToF-NR samples are subjected to the vapor flow protocol, X-ray reflectivity (XRR) and grazing incidence small-angle X-ray scattering (GISAXS) measurements are conducted to confirm a uniform vertical and lateral distribution of the salts inside the polymer film. For the *in situ* measurements, the films are dried for 1.5 h under a constant nitrogen flow to remove already incorporated H_2O, followed by a solvent-vapor-induced swelling process in a D_2O vapor atmosphere (4 h for ToF-NR; 15 h for FTIR) until an equilibrated state is reached. The contraction of the polymer films is triggered by subsequently exposing the films to a D_2O-acetone vapor atmosphere at a 9:1 volume-to-volume ratio (1.5 h for ToF-NR; 5 h for FTIR). During the whole experiment the temperature is kept constant at 23 °C. Static ToF-NR measurements are conducted at the equilibrated dry, swollen, and collapsed states, while the time-resolved measurements are measured in between each static measurement, giving access to the thickness and solvent content evolution. FTIR investigations help to comprehend the underlying molecular interactions contributing to the overall solvation mechanism. The corresponding results are discussed in the following, starting with the data collected by XRR measurements.

7.2.1. Distribution of Salts inside PNIPMAM Thin Films

XRR measurements are conducted of the as-prepared salt-containing PNIPMAM thin films at ambient conditions to investigate the vertical distribution of the components through the film after deposition. GISAXS measurements further provide information about the lateral salt distribution. From fits to the reflectivity curves, information about the film thickness, the scattering length density (SLD) profile, and the roughness of the films is obtained. It is noteworthy that due to the different scattering processes of X-rays compared to neutrons, materials have different SLD values in the respective measurements. On the one hand, XRR allows for a more thorough investigation of the vertical salt distribution inside the polymer films due to the enhanced contrast between the polymer and the introduced salts. On the other hand, NR allows us to investigate more thoroughly the vertical distribution and incorporation of deuterated solvent molecules inside a film since neutron SLDs are highly sensitive to isotope substitution. Figure 7.1 shows the measured XRR patterns of the $Mg(ClO_4)_2$- (orange) and $NaClO_4$-containing

(green) PNIPMAM thin films with their corresponding fits (black) as well as the derived SLD profiles. Detailed fit results are provided in Table 7.1.

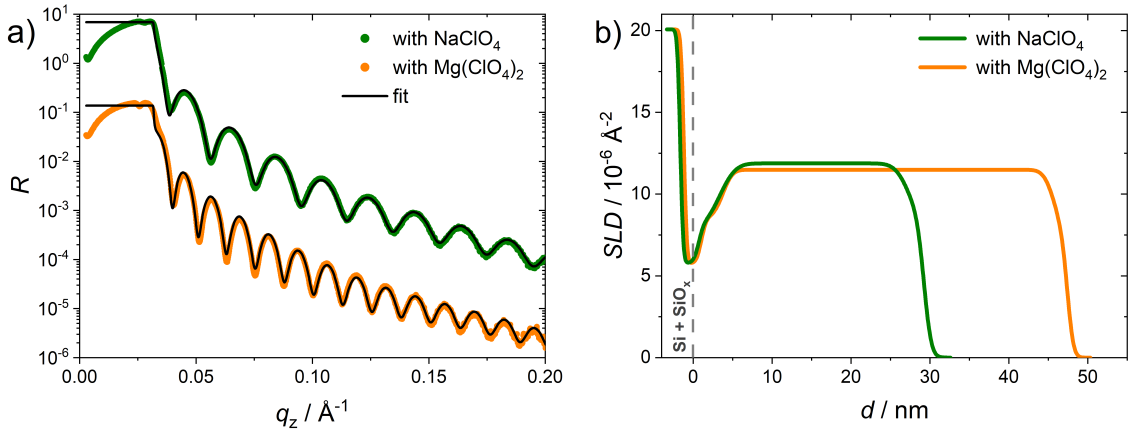

Figure 7.1.: (a) XRR reflectivity curves of the $Mg(ClO_4)_2$- (orange) and $NaClO_4$-containing (green) PNIPMAM thin films with their corresponding fits (black) and (b) derived SLD profiles. Reprinted with permission from Ref. [231], licensed under CC BY 4.0.

Table 7.1.: Film thickness d / Å, SLD / 10^{-6} Å^{-2} and roughness / Å obtained from the fits of the XRR measurements for the as-prepared $Mg(ClO_4)_2$- and $NaClO_4$-containing PNIPMAM thin films at ambient condition. For the PNIPMAM + $Mg(ClO_4)_2$ and the PNIPMAM + $NaClO_4$ sample the following parameters for the SiO_2 layer are used: d = 15.00 Å, SLD = 5.77 × 10^{-6} Å^{-2}, roughness = 5 Å.

PNIPMAM + $Mg(ClO_4)_2$	**layer structure**	**d / Å**	**SLD / 10^{-6} Å^{-2}**	**roughness / Å**
as-prepared	polymer-air interface	14.9 ± 1.1	6.74 ± 0.52	6.0 ± 1.9
	polymer bulk layer	422.3 ± 7.8	11.49 ± 0.09	6.6 ± 2.0
	polymer-substrate interface	27.1 ± 0.5	8.54 ± 0.08	9.8 ± 0.5
PNIPMAM + $NaClO_4$	**layer structure**	**d / Å**	**SLD / 10^{-6} Å^{-2}**	**roughness / Å**
as-prepared	polymer-air interface	17.0 ± 1.3	7.64 ± 0.23	7.1 ± 1.1
	polymer bulk layer	242.3 ± 5.9	11.88 ± 0.18	7.1 ± 2.2
	polymer-substrate interface	26.5 ± 1.1	7.89 ± 0.15	12.9 ± 1.1

Both XRR reflectivity curves show pronounced Kiessig fringes even in the high q_z range, which implies the smoothness of the prepared films and therefore confirms the suitability of the salt-containing samples for ToF-NR investigation. Furthermore, from fits to the XRR data with a six-layer model consisting of, apart from a silicon layer with its native oxide layer for the substrate as well as infinite air at the top of the sample, a polymer-substrate interface, a polymer bulk layer, and a polymer-air interface, SLD profiles are

observed (Figure 7.1b). Besides the difference in the observed film thickness, the profiles show that the shapes of the curves resemble each other. In the bulk region, a homogeneous vertical distribution of the individual salts in the polymer matrix is present, while at the interfaces, the decreased SLD values suggest either a depletion of material or the presence of already incorporated H_2O from the surrounding environment.

In addition to the information about the vertical material distribution obtained by XRR, GISAXS measurements provide information about the lateral distribution of the salts inside the thin polymer film. The 2D GISAXS data (Figure B.1) and the horizontal line cuts at the Yoneda peak region of the polymer (Figure B.2) are provided in Appendix B for a salt-free, a $Mg(ClO_4)_2$-containing, and a $NaClO_4$-containing PNIPMAM thin film. The 2D GISAXS data of the salt-free PNIPMAM film show no pronounced scattering features besides a strong forward scattering in the resolution limit. The horizontal line cut taken at the Yoneda peak position of the polymer indicates a lack of characteristic lateral structures inside the polymer film. Thus, no characteristic variation in the lateral direction is observed, as expected for a homopolymer. Similarly, by comparison of the horizontal line cuts of the salt-containing films, no lateral features are discernible. The two line cuts show no deviations from the salt-free sample, which implies that the addition of salt does not introduce any lateral structures inside the PNIPMAM film. Therefore, a homogeneous lateral distribution of the salts inside the polymer films is confirmed.

7.2.2. Static Equilibrated Film States

Static ToF-NR measurements are conducted at the equilibrated dry, swollen, and collapsed state for PNIPMAM thin films containing either $NaClO_4$ or $Mg(ClO_4)_2$ (Figure 7.2). The obtained reflectivity patterns are fitted by using a six-layer model as explained for the XRR data analysis, which considers different contributions throughout the sample verticals, i.e., the polymer bulk region and the potential occurrence of interfaces, besides the layers originating from the substrate. The fit parameters for the Si substrate and its native oxide layer are kept identical for each sample throughout the whole ToF-NR data analysis. Detailed results from the fits are presented in Table 7.2.

Table 7.2.: Film thickness d / Å, SLD / 10^{-6} Å^{-2} and roughness / Å obtained from the fits of the static ToF-NR measurements for the $Mg(ClO_4)_2$- and $NaClO_4$-containing PNIPMAM thin films at the equilibrated states, i.e., dry, swollen and collapsed. The fit parameters for the Si substrate and its native oxide layer are kept identical for each sample throughout the whole ToF-NR data analysis. For the PNIPMAM + $Mg(ClO_4)_2$ sample the following parameters for the SiO_2 layer are used: d = 23.73 Å, SLD = 3.47 × 10^{-6} Å^{-2}, roughness = 7 Å. For the PNIPMAM + $NaClO_4$ the parameters of the SiO_2 layer are: d = 20.20 Å, SLD = 3.47 × 10^{-6} Å^{-2}, roughness = 7 Å.

PNIPMAM + $Mg(ClO_4)_2$	**layer structure**	**d / Å**	**SLD / 10^{-6} Å^{-2}**	**roughness / Å**
dry	polymer-air interface	–	–	–
	polymer-bulk layer	305.7 ± 1.6	1.14 ± 0.01	3.0 ± 1.2
	polymer-substrate interface	32.3 ± 1.8	0.94 ± 0.02	2.7 ± 0.7
swollen	polymer-air interface	39.1 ± 2.6	4.84 ± 0.10	4.8 ± 0.4
	polymer-bulk layer	425.8 ± 2.1	3.63 ± 0.01	18.6 ± 1.6
	polymer-substrate interface	13.4 ± 1.1	4.98 ± 0.11	3.5 ± 0.1
collapsed	polymer-air interface	–	–	–
	polymer-bulk layer	424.3 ± 0.1	2.58 ± 0.01	1.2 ± 0.5
	polymer-substrate interface	5.2 ± 0.2	5.16 ± 0.07	2.4 ± 0.1
PNIPMAM + $NaClO_4$	**layer structure**	**d / Å**	**SLD / 10^{-6} Å^{-2}**	**roughness / Å**
dry	polymer-air interface	46.6 ± 2.0	0.71 ± 0.02	3.5 ± 0.1
	polymer-bulk layer	265.3 ± 3.0	0.92 ± 0.01	10.2 ± 3.6
	polymer-substrate interface	40.6 ± 1.4	0.37 ± 0.02	15.7 ± 1.3
swollen	polymer-air interface	132.9 ± 1.3	5.01 ± 0.01	12.9 ± 0.1
	polymer-bulk layer	750.9 ± 1.9	4.55 ± 0.01	40.0 ± 1.6
	polymer-substrate interface	93.4 ± 1.3	2.59 ± 0.03	43.9 ± 1.2
collapsed	polymer-air interface	–	–	–
	polymer-bulk layer	470.8 ± 2.4	2.66 ± 0.01	15.0 ± 0.3
	polymer-substrate interface	10.8 ± 2.6	4.84 ± 0.55	3.1 ± 0.2

In Figure 7.2, changes in the position of the critical edge and the spacing between the Kiessig fringes are observed between the individual static measurements at different equilibrated states. A shift of the critical edge toward higher q_z-values and a decrease in the spacing between the modulations is observed for the D_2O swollen films compared to the dry ones. This indicates that D_2O molecules are incorporated into the films, increasing the thickness of the whole film. Comparing the reflectivity curves obtained for the swollen and collapsed films, the opposite behavior is observed, indicating that the films contract in terms of their thickness, and the movement of the critical edge indicates the exchange

to a mixture of D_2O and acetone inside the films. From fits to the reflectivity curves, SLD profiles of the PNIPMAM thin film containing either $Mg(ClO_4)_2$ or $NaClO_4$ are observed.

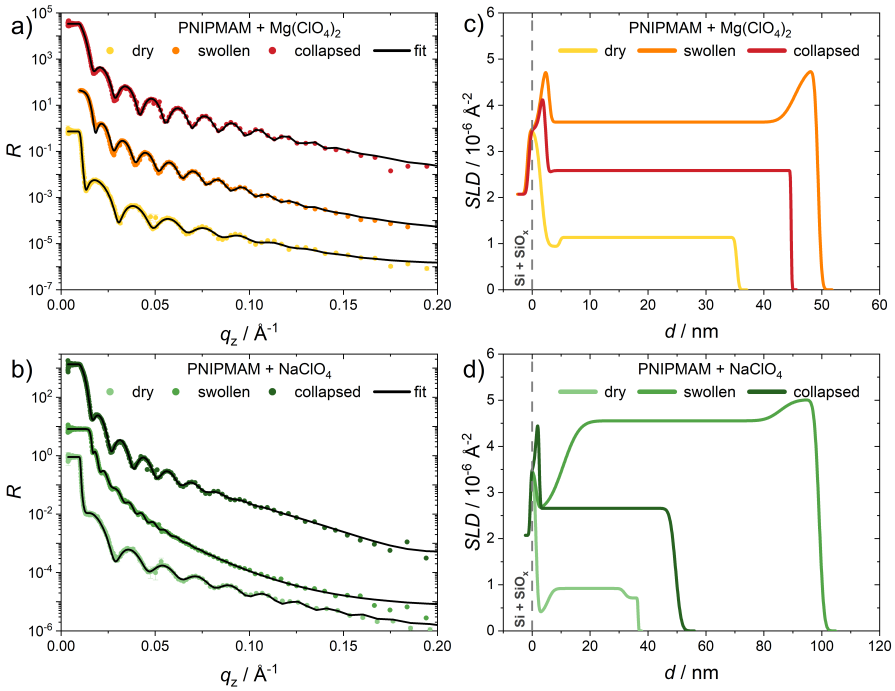

Figure 7.2.: (a,b) Static ToF-NR reflectivity curves at the equilibrated dry (light), swollen (medium), and collapsed (dark) states with their corresponding fits (black) for the $Mg(ClO_4)_2$- (orange) and $NaClO_4$-containing (green) PNIPMAM thin films as well as (c,d) derived SLD profiles. Reprinted with permission from Ref. [231], licensed under CC BY 4.0.

The curves for the dry states are similar in the regard that at the bulk region, a homogeneous vertical distribution of the polymer as well as the salt is observed, which has already been confirmed with XRR measurements. Additionally, the same deviations at the interfaces, i.e., the polymer-substrate and the polymer-air interfaces, are obtained even after drying the films under a continuous nitrogen flow. Furthermore, the SLD profiles of these samples in the dry state indicate that the film thicknesses are approximately 34 nm and within 1.5 nm of each other. Comparing the SLD profiles of the individual swollen states, an increase in film thickness and an overall increase in the SLD are revealed, which is attributed to the uptake of D_2O molecules into the films. Nevertheless, the vertical solvent distribution in the films differs: While the SLD is increased at the polymer-air interface for both systems, which can be attributed to an accumulation layer of D_2O molecules on an already water saturated thin film, different behaviors are observed at the polymer-substrate interfaces. Increased SLD values at interfaces are attributed to an enrichment of D_2O molecules, which is the case for $Mg(ClO_4)_2$-containing thin films. In the case of differing SLD behaviors at the polymer-substrate and polymer-air interfaces, the differ-

ences indicate a nonhomogeneous vertical distribution of the solvent throughout the film, as observed for the $NaClO_4$-containing PNIPMAM thin film. The change of the solvent vapor atmosphere from a D_2O to D_2O-acetone mixture leads to a decrease in the thickness and SLD of the system. Also, the D_2O enrichment layer at the polymer-air interface is depleted, while an increased SLD is still observed at the polymer-substrate interface. This indicates that the release of the solvent molecules is facilitated at the polymer-air interface due to the constant vapor flow, whereas attractive polar interactions between the solvent molecules and the hydrophilic surface of the silicon substrate prevent the escape of the solvent molecules. In particular, at the polymer-substrate interface, the native SiO_x oxide layer with its silanol groups is able to form hydrogen bonds with the D_2O molecules as well as with the amide functional groups of the polymer.

7.2.3. Kinetic Film Thickness Changes

To investigate the kinetic evolution between the equilibrated states, time-resolved ToF-NR measurements are performed, for which each reflectivity curve is measured for 5 s over 3.5 h for the swelling and 1.5 h for the collapse process. The data are fitted using a single layer to describe the salt-containing polymer films on top of a substrate. Furthermore, it is ensured that the fit parameters of the static measurements at the equilibrated dry and swollen states match the respective end points of the kinetic measurements.

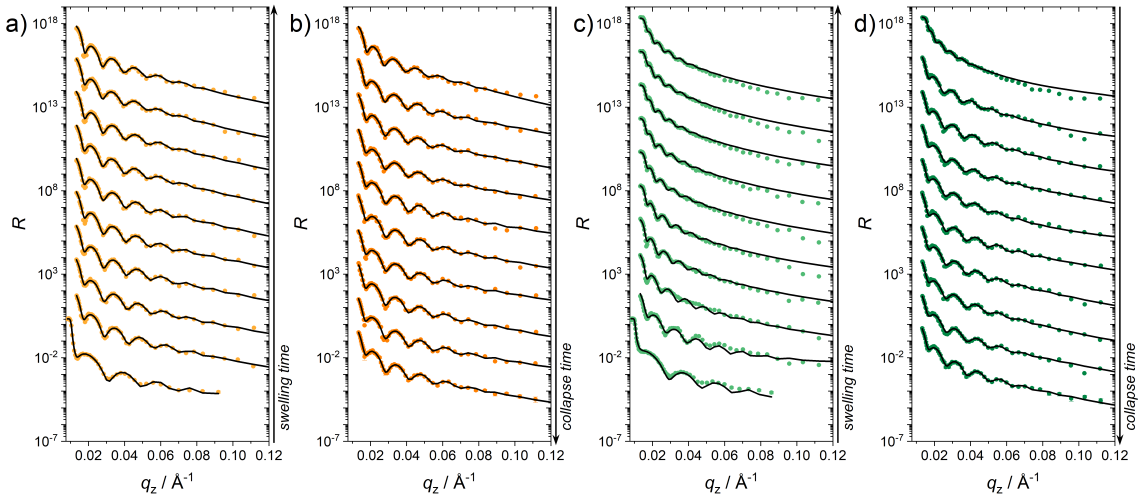

Figure 7.3.: Selected time-resolved ToF-NR reflectivity curves for (a,c) swelling (light colors) and (b,d) collapse (dark colors) processes with their corresponding fits (black) for the $Mg(ClO_4)_2$- (orange) and $NaClO_4$-containing (green) PNIPMAM thin films. Curves are shifted along the y-axis over time, where for the swelling (a,c) reflectivity curves in intervals of 21 min and for the collapse (b,d) in intervals of 9 min are shown. Reprinted with permission from Ref. [231], licensed under CC BY 4.0.

In Figure 7.3, selected reflectivity curves with the respective fits (black) are shown for the $Mg(ClO_4)_2$- (orange) and $NaClO_4$-containing (green) PNIPMAM thin films during the swelling (light color) and collapse (dark color) processes. The shift of the critical edge and the changes in the spacing of the Kiessig fringes resemble the findings of the static ToF-NR measurements. Furthermore, the analysis provides insights about the film thickness d (Figure 7.4a) and the SLD evolution (Figure 7.4b), as well as about the evolution of the solvent content ϕ (Figure 7.6).

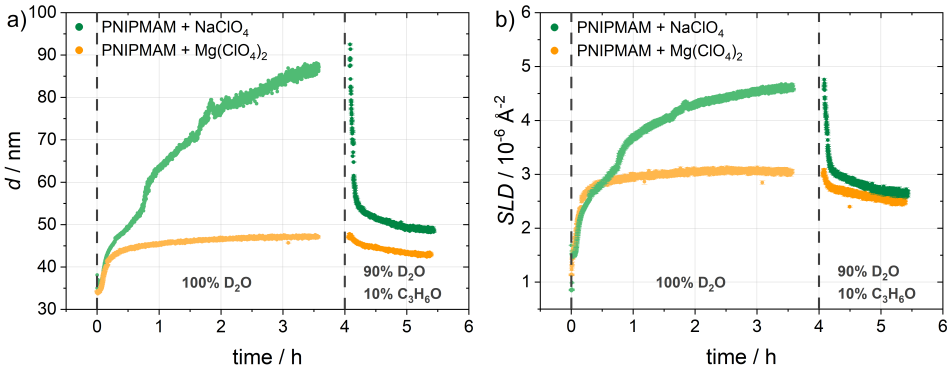

Figure 7.4.: (a) Thickness and (b) SLD evolution over time for the swelling (light colors) and collapse (dark colors) processes of the $Mg(ClO_4)_2$- (orange) and $NaClO_4$-containing (green) PNIPMAM thin films. Dashed lines indicate changes in the vapor atmosphere, i.e., from a pure D_2O vapor atmosphere (100% D_2O) to a D_2O-acetone vapor mixture atmosphere (90% D_2O and 10% C_3H_6O). Reprinted with permission from Ref. [231], licensed under CC BY 4.0.

Starting from similar initial film thicknesses in the dry states, the $Mg(ClO_4)_2$-containing PNIPMAM thin film shows a thickness increase in D_2O vapor atmosphere of 39%, whereas the $NaClO_4$-containing film reaches a much stronger thickness increase of over 177% at the same time. As demonstrated in the previous publication [167], the swelling ability of salt-containing PNIPMAM thin films can be modified by the addition of two magnesium salts with different anions, namely, $Mg(ClO_4)_2$ and $Mg(NO_3)_2$. A detailed explanation of the interpretation of the swelling behavior of salt-containing PNIPMAM thin films is given in Ref. [167], whereas the focus of this work is on the contraction behavior after the exchange of the vapor atmosphere. In summary, water molecules are predominantly incorporated at the film surface until the water molecules diffuse into the excluded free volume in the bulk region of the polymer network. As soon as a certain amount of water is incorporated, the mobility of the polymer chains increases. This leads to a rearrangement of the polymer chains and the water network, leading to increased solvent accessibility of the polymer chains. These two main processes are assumed to be the reasons for the two-step swelling process or the different slopes of thickness evolution. It is noteworthy that for the $Mg(ClO_4)_2$-containing PNIPMAM thin films, the swelling abilities

are comparable, independent of the starting film thickness ranging between 35 and 90 nm. Furthermore, this study shows that the response behavior of salt-containing PNIPMAM thin films is even more significantly enhanced by the incorporation of $NaClO_4$ compared to both Mg salts. This demonstrates that the responsiveness of PNIPMAM thin films toward a D_2O vapor atmosphere can be easily modulated by introducing specific salts. With the introduction of the D_2O-acetone vapor mixture atmosphere in a 9:1 volume-to-volume ratio, the volume phase transition behavior is triggered by the cononsolvency effect, resulting in an abrupt thickness decrease until an equilibrated state is reached. The system containing $Mg(ClO_4)_2$ contracted by 9%, whereas the one containing $NaClO_4$ contracted even by 51%. Both systems shrink to a remaining swelling ratio of around 134%, which assumes a preferential solvation state of the films independent of the type of added salt. Regarding the potential of thin film systems for applications such as soft matter-based vapor-responsive nanoswitches or gas sensors, strong and fast responses of the thin films toward a change in the surrounding environment are preferred. Here, a strong change in thickness upon the exchange from a D_2O to a D_2O-acetone vapor mixture atmosphere is observed within the first 15 min. Such a rapid contraction of a salt-free polymer thin film exposed to the same conditions was observed for PMMA-*b*-PNIPMAM thin films with an initial film thickness of 140 nm [83]. However, with this study, we demonstrate that a similarly strong response is achieved by modifying PNIPMAM homopolymer thin films by the addition of salts.

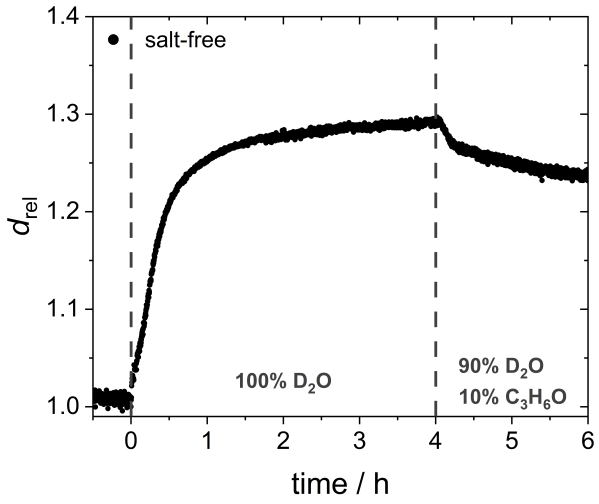

Figure 7.5.: Relative thickness d_{rel} evolution over time for the swelling and collapse process of a salt-free PNIPMAM thin film. Dashed lines indicate changes in the vapor atmosphere, i.e., from a pure D_2O (100% D_2O) to a D_2O-acetone vapor mixture atmosphere (90% D_2O and 10% C_3H_6O). Reprinted with permission from Ref. [231], licensed under CC BY 4.0.

For comparison, in Figure 7.5 the thickness evolution over time for a salt-free PNIPMAM homopolymer thin film exposed to the same conditions is shown. The thickness increase in the equilibrated swollen state is determined as 29%, and the thickness decrease for the contraction is determined as 5%.

To further investigate the influence of the observed salt dependence on the response, an analysis of the evolution of the solvent and cosolvent content over time is conducted based on the ToF-NR measurements. The volume fraction $\phi(t)$ evolution of the individual solvents inside a film is calculated as follows [187]:

$$\phi_{\text{solvmix}}(t) = \frac{SLD_{\text{meas}}(t) - SLD_{\text{dry}}}{SLD_{\text{solvmix}}(t) - SLD_{\text{dry}}} \tag{7.1}$$

The above equation considers the difference in SLDs between the measured SLD at a given time ($SLD_{\text{meas}}(t)$) and the SLD of the dry film (SLD_{dry}) divided by the SLD difference between the solvent mixture ($SLD_{\text{solvmix}}(t)$) and the dry film. The SLD of a given solvent mixture is calculated by taking into account the SLD values of each solvent and the corresponding molar fraction $x_{\text{cosolv}}(t)$ of the cosolvent:

$$SLD_{\text{solvmix}}(t) = (1 - x_{\text{cosolv}}(t))SLD_{\text{solv}} + x_{\text{cosolv}}(t)SLD_{\text{cosolv}} \tag{7.2}$$

For a pure solvent vapor atmosphere $x_{\text{cosolv}}(t)$ becomes 0, which is used to calculate the D_2O solvent content for the swelling process. In the case of the collapse process, the cosolvent molar fraction $x_{\text{cosolv}}(t)$ has to be calculated from the measured SLD and thickness values as given by the following equation:

$$x_{\text{cosolv}}(t) = \left(\left(\frac{SLD_{\text{meas}}(t) - SLD_{\text{dry}}}{\gamma(1 - \frac{d_{\text{ini}}}{d_{\text{meas}}(t)})}\right) + SLD_{\text{dry}} - SLD_{\text{solv}}\right)\frac{1}{SLD_{\text{cosolv}} - SLD_{\text{solv}}} \tag{7.3}$$

Here, d_{ini} is the initial film thickness in the dry state, while $d_{\text{meas}}(t)$ is the measured film thickness at a given time. Furthermore, the above equation weighs the relative thickness $d_{\text{ini}}/d_{\text{meas}}(t)$ by a volumetric conversion factor γ, which describes the volume change when going from bulk to solvated polymer chains, and is defined as:

$$\gamma = \frac{SLD_{\text{meas}}(t') - SLD_{\text{dry}}}{SLD_{\text{solv}} - SLD_{\text{dry}}}\frac{1}{1 - \frac{d_{\text{ini}}}{d_{\text{meas}}(t')}} \tag{7.4}$$

Since the volumetric conversion factor γ cannot be obtained from the collapse process, it has to be estimated from the swelling process. Therefore, a time point t' in the swelling process has to be chosen, at which the film thickness resembles the thickness in the equilibrated collapse state, to obtain an accurate estimation of the volumetric conversion factor for the collapse.

In Figure 7.6 the solvent contents $\phi(t)$ calculated by the above method are plotted for the $NaClO_4$- (a) and $Mg(ClO_4)_2$-containing (b) PNIPMAM thin films and are separated into the swelling process in a D_2O vapor atmosphere and the collapse process in a D_2O-acetone solvent vapor atmosphere. Additionally, the total solvent content for the collapse process is shown.

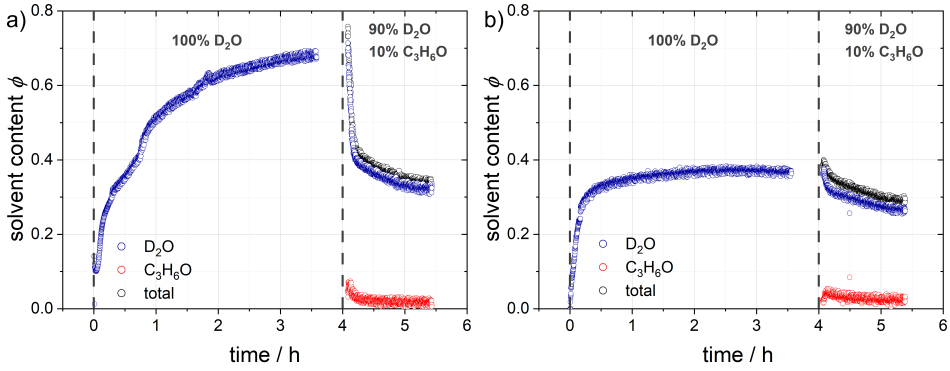

Figure 7.6.: Solvent content evolution over time for the swelling and collapse processes for the (a) $NaClO_4$- and (b) $Mg(ClO_4)_2$-containing PNIPMAM thin films. Dashed lines indicate changes in the vapor atmosphere, i.e., from a D_2O vapor atmosphere (100% D_2O) to a D_2O-acetone solvent vapor atmosphere (90% D_2O and 10% C_3H_6O). D_2O content is indicated in blue, acetone content in red, and the total solvent content in black. Reprinted with permission from Ref. [231], licensed under CC BY 4.0.

The PNIPMAM thin film containing $Mg(ClO_4)_2$ reaches a D_2O volume fraction of about 37% in the swollen state, whereas the $NaClO_4$-containing film reaches a value of 69%. In the case of the cononsolvency-induced contraction of the films, as the solvent vapor mixture is introduced into the system, the D_2O content inside the film immediately decreases, whereas the acetone content first increases before being again released from the film. The maximum amount of acetone uptake peaks at 5% for the $Mg(ClO_4)_2$-containing film and at 7% for the $NaClO_4$-containing film. After a delay of 15 min, the acetone content decreases and stabilizes at about 2% for both systems.

7.2.4. Molecular Interactions

Due to the variety of participating functional groups, the observed volume phase transitions are governed by the interactions of the individual species. Not only do the interactions arise from electrostatic interactions, mainly originating from the contained ions, but also equally as important from the formation of hydrogen bonds between the polymer and the solvent molecules. Consequently, the magnitude of these interactions represents a sensitive probe for the progress of the volume phase transition, which can be quantified using FTIR. Since the vibrational frequency is dependent on the bond strength of the constituting atoms, the shifts of the peak positions can be used to elucidate the relative bond strength variation over time. Collected FTIR spectra during the swelling and collapse processes are shown in Figure 7.7 for both salt-containing systems.

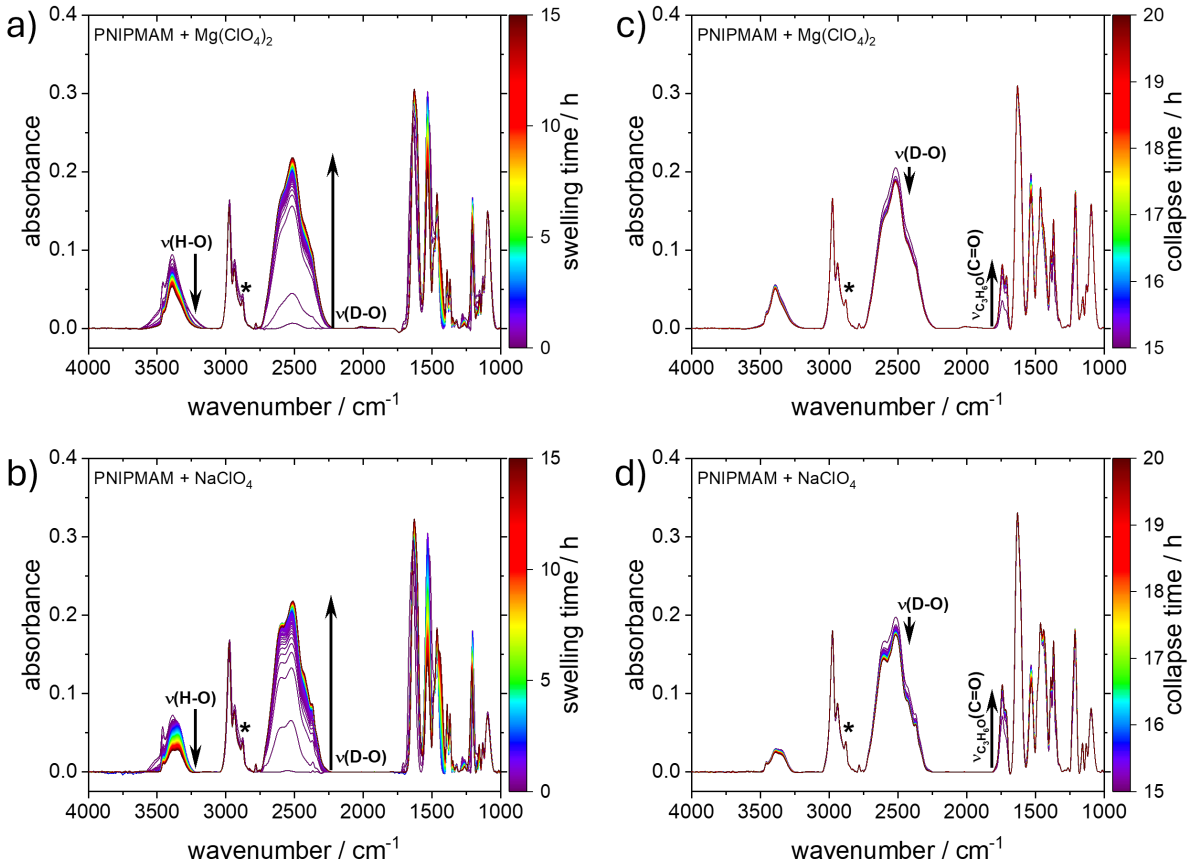

Figure 7.7.: FTIR spectra measured during the (a,b) swelling and (c,d) collapse of a PNIPMAM film containing either $Mg(ClO_4)_2$ (top row) or $NaClO_4$ (bottom row). Normalization is done by reweighting the intensity of the $\nu_{sym}(C-H_3)$ signal in the dry state to an absorbance of 0.05. Black arrows indicate the intensity trends of the signals originating from solvent molecules over time. Reprinted with permission from Ref. [231], licensed under CC BY 4.0.

Following the discussion of the solvent contents determined by ToF-NR, the FTIR spectra confirm the overall observation that during the swelling D_2O is incorporated into the film, while during the collapse D_2O is ejected out of the system accompanied by the uptake of acetone. It should be noted that the signal at ≈3360 cm^{-1}, which is attributed to the stretching vibration of H_2O, indicates the presence of residual water, which is substituted by D_2O over the course of the experiment. To further quantify the extent of interaction changes during the transitions, the shifts of the amide I, amide II, and $\nu_{asym}(ClO_4^-)$ peaks are shown in Figure 7.8.

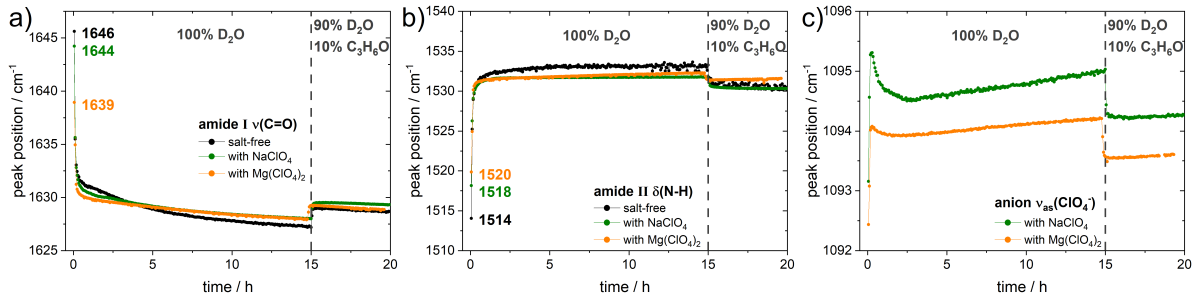

Figure 7.8.: Time-resolved peak positions of the (a) amide I, (b) amide II, (c) $\nu_{asym}(ClO_4^-)$ signals for a PNIPMAM film containing either $Mg(ClO_4)_2$ (orange) or $NaClO_4$ (green), as well as for a salt-free reference film (black). Initial peak positions in the dry state are given in the respective colors. Reprinted with permission from Ref. [231], licensed under CC BY 4.0.

By comparing the peak positions in the initial dry states for the amide I band, it can be inferred from the red shift that ion-dipole interactions between the cations and the carbonyl groups of the polymer are formed [199]. Upon the introduction of D_2O molecules, the amide I signal shows a pronounced shift toward lower wavenumbers, indicating hydrogen bond formation, irrespective of salt addition. In contrast, the peak shifts toward higher wavenumbers when a D_2O-acetone vapor mixture is introduced. Taking into account the observation from the ToF-NR investigation that during the collapse process D_2O is ejected from the film while acetone is incorporated, this shift can be attributed to a decreased D_2O content inside the films as well as to the inability of acetone to act as a hydrogen bond donor. However, it should be noted that the carbonyl group of acetone can still serve as a hydrogen bond acceptor. The reverse trend of the peak position shifts is observed for the amide II band since it originates mainly from a bending vibration. Furthermore, since the inorganic anion is chosen such that its absorption bands do not overlap with signals arising from the rest of the components, it can likewise be used as a probe of ion-solvent interactions. Based on the peak position shifts of the anions at the different solvent compositions, a hydration shell is formed during the D_2O uptake, while the solvation shell changes when acetone is added.

7.2.5. Sequence of Solvation Events

To further dissect the complex overlapping signals in the FTIR spectra, 2D FTIR correlation analysis is performed for both the swelling and collapse transitions, which is also used to infer a sequence of solvation events. The following discussion on the swelling process is restricted to key points necessary for understanding the subsequent collapse process caused by the cosolvent addition. A detailed account of the 2D FTIR correlation analysis of the swelling process of PNIPMAM thin films containing salts is provided in earlier work [167]. A closer inspection of the amide I signal at around 1640 cm^{-1} reveals that during the D_2O uptake, a shoulder at lower wavenumbers appears. The appearance and the further development of this shoulder are attributed to the formation of NHC=O···D−OD interactions, while the main part of the band stems from intra- or intermolecular NHC=O···H−N interactions between the polymer chains. In 2D correlation analysis, the sign of a crosspeak in the asynchronous spectrum gives information about whether the change in the signals is delayed or accelerated, respectively, to one another. In Figure 7.9, the crosspeak in the asynchronous spectrum between the amide I and II bands is positive (red), which – according to Noda's rules [205,232] – however, has to be interpreted as negative (blue) due to the negative sign of the crosspeak in the synchronous spectrum between the bands. Therefore, the changes in the amide I signal occur before the amide II signal evolves.

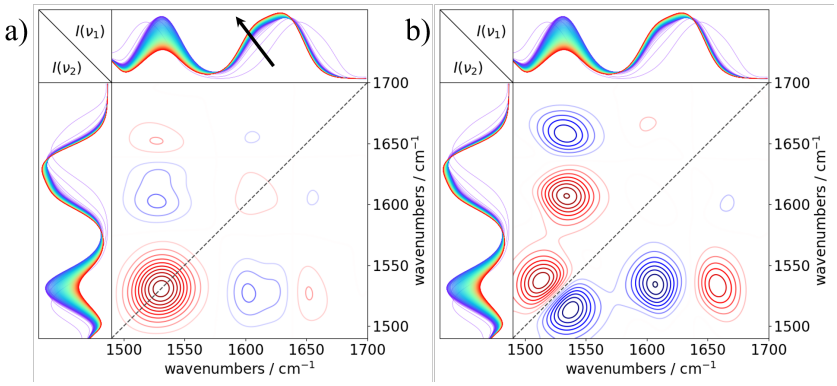

Figure 7.9.: (a) Synchronous and (b) asynchronous 2D FTIR correlation plots in the wavenumber range between 1490 and 1700 cm^{-1} attributed to the amide I and the amide II signals of the $NaClO_4$-containing PNIPMAM film during the swelling. A positive correlation is indicated in red, and a negative correlation is indicated in blue. The black arrow indicates the formation of NHC=O···D−OD hydrogen bonds. Reprinted with permission from Ref. [231], licensed under CC BY 4.0.

As the focus of this work is on the investigation of the changes in the solvation state upon the transition from a D_2O to a D_2O-acetone solvent vapor mixture atmosphere, in

the following section, the 2D FTIR correlation analysis is carried out for the contracting film. Since the origin of the cononsolvency effect of polymers is still under debate [3], which is due to the multicomponent nature of the investigated systems, the application of 2D FTIR correlation analysis is particularly attractive. Additionally, the investigation of thin films in a vapor atmosphere instead of using polymers in solution helps to decelerate the solvation process and, thus, allows to gain further insights. By choosing a polymer-(co)solvent system with several nonoverlapping signals, in addition to using IR-active anions, the intricate design of the chosen system is highlighted. First, the amide signals are investigated, for which the 2D FTIR correlation plots are shown in Figure 7.10.

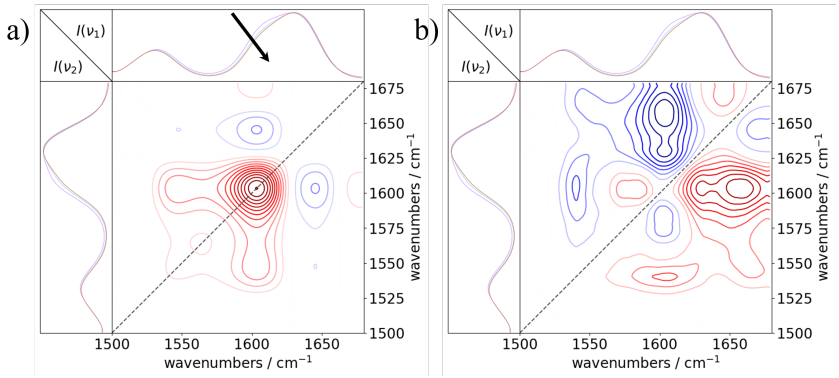

Figure 7.10.: (a) Synchronous and (b) asynchronous 2D FTIR correlation plots in the wavenumber range between 1500 and 1680 cm^{-1} attributed to the amide I and the amide II signals of the $NaClO_4$-containing PNIPMAM film during the contraction. A positive correlation is indicated in red, and a negative correlation is indicated in blue. The black arrow indicates the depletion of NHC=O···D−OD hydrogen bonds. Reprinted with permission from Ref. [231], licensed under CC BY 4.0.

The buildup of the shoulder in the amide I signal during the swelling process is attributed to NHC=O···D−OD interactions. During the exchange of vapor atmospheres, the previously incorporated D_2O is released, which is reflected by the decrease in the intensity of the shoulder, revealing that hydrogen bonds between the polymer and D_2O are perturbed. By analyzing the correlation spectra for the amide bands during the contraction process, the order NHC=O···D−OD > NHC=O···H−N > amide II can be deduced, in which the first two interactions are attributed to the amide I signal. This sequence of events is the same as for the swelling process. It is believed that the introduction of acetone molecules reduces amide-D_2O interactions and that due to the contraction and solvent release, polymer-polymer interactions are increasingly formed. To additionally elucidate cosolvent-polymer interactions, the signal arising from the carbonyl group of the acetone molecules in the range of 1680 to 1800 cm^{-1} is analyzed. Figure 7.11 shows the 2D FTIR correlation plots of this signal.

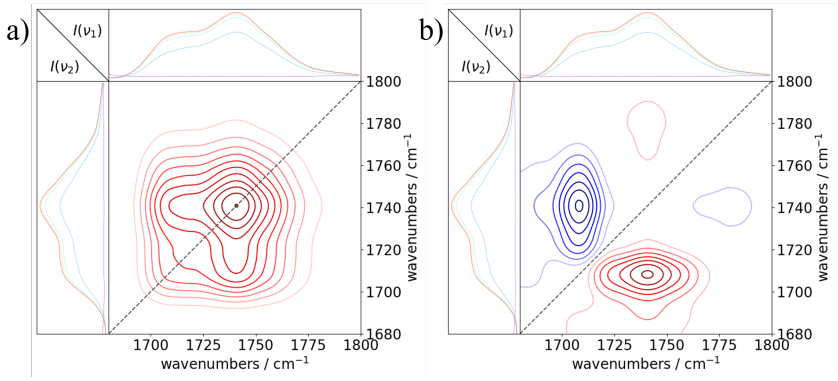

Figure 7.11.: (a) Synchronous and (b) asynchronous 2D FTIR correlation plots in the wavenumber range between 1680 and 1800 cm^{-1} attributed to the stretching vibration of the carbonyl group of acetone for the $NaClO_4$-containing PNIPMAM film during the contraction. A positive correlation is indicated in red, and a negative correlation is indicated in blue. Reprinted with permission from Ref. [231], licensed under CC BY 4.0.

A closer inspection reveals that the band consists of two individual signals. These are attributed to acetone-acetone interactions ($Me_2C{=}O$) at higher wavenumbers and acetone-amide interactions ($Me_2C{=}O{\cdots}H{-}N$) at lower wavenumbers. Evaluation of the correlation plots reveals that acetone is first introduced into the film before acetone-amide interactions are formed. Furthermore, cross analysis between the amide and acetone signals is performed, as shown in Figure 7.12.

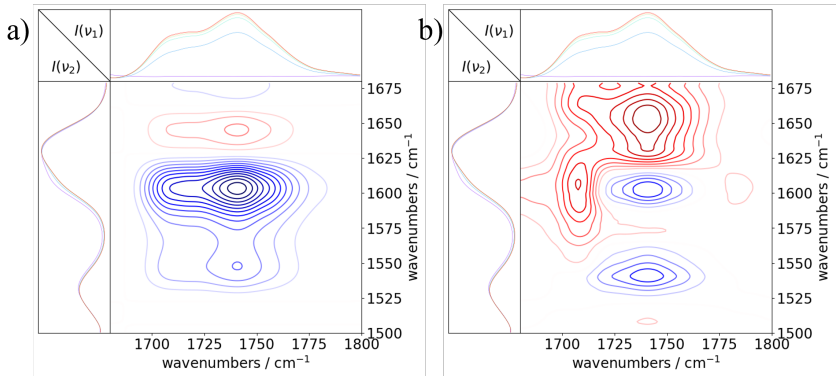

Figure 7.12.: (a) Synchronous and (b) asynchronous cross analysis 2D FTIR correlation plots in the wavenumber range between 1680 and 1800 cm^{-1} and between 1500 and 1680 cm^{-1} for the $NaClO_4$-containing PNIPMAM film during the contraction. A positive correlation is indicated in red, and a negative correlation is indicated in blue. Reprinted with permission from Ref. [231], licensed under CC BY 4.0.

The overall sequence of changes in the signals is deduced as $\nu(Me_2C{=}O) > \nu(NHC{=}O{\cdots}D{-}OD) > \nu(Me_2C{=}O{\cdots}H{-}N) > \nu(NHC{=}O{\cdots}H{-}N)$. This finding signifies

that first acetone is incorporated into the films, followed by the depletion of the amide-D_2O interactions, which is accompanied by the formation of amide-acetone interactions and the formation of the again more preferred amide-amide interactions of the polymer itself. Finally, the role of the introduced anions in the solvation mechanism can be evaluated by cross-correlating the changes in the $\nu(ClO_4^-)$ signal at around 1095 cm^{-1} with the signals arising from the acetone molecules and from the amide functional groups of the polymer. Figure 7.13 shows the corresponding 2D FTIR correlation plots.

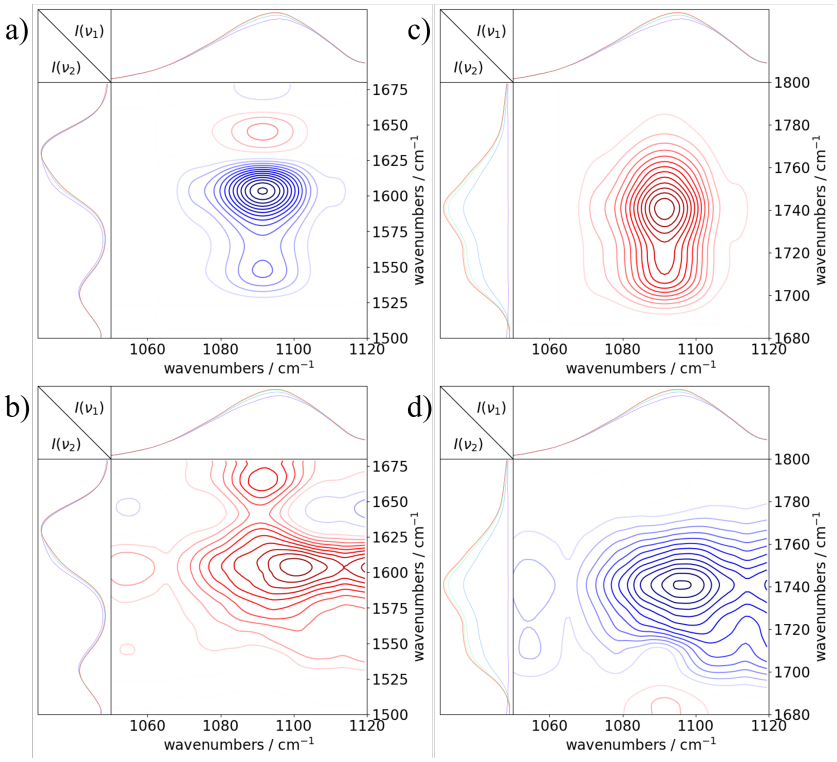

Figure 7.13.: (a,c) Synchronous and (b,d) asynchronous cross analysis 2D FTIR correlation plots in the wavenumber range between 1050 and 1120 cm^{-1} and between 1500 and 1680 cm^{-1} and also between 1050 and 1120 cm^{-1} and between 1680 and 1800 cm^{-1} for the $NaClO_4$-containing PNIPMAM film during the contraction. A positive correlation is indicated in red, and a negative correlation is indicated in blue. Reprinted with permission from Ref. [231], licensed under CC BY 4.0.

Figure 7.13a,b illustrates the cross analysis between the anion and the amide signals, revealing the sequence of $\nu(NHC{=}O{\cdots}D{-}OD) > \nu(ClO_4^-) > \nu(NHC{=}O{\cdots}H{-}N) >$ amide II. Additionally, the cross analysis between the anion and the acetone signals in Figure 7.13c,d indicates the order of $\nu(Me_2C{=}O) > \nu(ClO_4^-) > \nu(Me_2C{=}O{\cdots}H{-}N)$. In general, due to the charged nature of the anion, interactions with polar solvent molecules are preferred over the interactions with the polymer chains. Therefore, as expected, acetone molecules first change the solvation shell around the perchlorate anion before they

participate in hydrogen bonding with the amide moiety. Nevertheless, the amide-D_2O interactions are also rapidly disturbed due to the strong sensitivity of the polymer toward the cosolvent. Together with the change in the solvation shell around the anion, this constitutes the first step of the contraction process. Overall, due to the incorporation of acetone molecules, the D_2O hydration shells around the polar and protic amide functional groups of the polymer, as well as around the perchlorate anions, get disturbed. Additionally, despite the formation of amide-acetone interactions, an increase in amide-amide interactions is observed, which is attributed to the contraction of the polymer films.

7.3. Conclusion

In this study, the response behavior of $NaClO_4$- and $Mg(ClO_4)_2$-containing PNIPMAM films is investigated in terms of the swelling behavior in a D_2O vapor atmosphere, as well as the subsequent contraction in a D_2O-acetone vapor mixture atmosphere, inducing a cononsolvency effect. For the as-prepared thin films, XRR and GISAXS measurements confirm the uniform vertical and lateral distribution of the introduced salts inside the polymer matrix. Static and time-resolved ToF-NR measurements enable the investigation of the solvent incorporation and reveal that the response of the films toward the different vapor atmospheres can be modulated by the type of perchlorate salt added. The $NaClO_4$-containing PNIPMAM thin films exhibit a strong film thickness increase of 177% in D_2O and a pronounced decrease of 51% in D_2O-acetone vapor atmosphere. In contrast, the $Mg(ClO_4)_2$-containing PNIPMAM thin films reach a moderate film thickness increase of 39% and a slight decrease of 9%. Investigation of the evolution of the solvent contents inside the films reveals the solvent incorporation and release processes caused by cosolvent addition. After the D_2O molecules are incorporated during the swelling process, the contraction of the films leads to a release of D_2O molecules, while the acetone concentration inside the films first builds up to 7 vol% before subsequently depleting to around 2 vol%. Furthermore, the solvation behavior is studied on a molecular level by *in situ* FTIR. The spectra series are analyzed by investigating the peak position shifts of signals corresponding to functional groups, which participate in the solvation events. Furthermore, the spectra are subjected to 2D FTIR correlation analysis to elucidate the sequence of solvation events. Exemplarily using the amide functional group as a probe for the solvation behavior, reveals that during the swelling process D_2O-amide interactions are formed, which are perturbed upon the addition of acetone. During the vapor exchange D_2O-amide interactions reduce, while acetone-amide interactions develop accompanied by amide-amide interactions, which again become favored during the contraction. A detailed

understanding of the complex kinetic processes during water uptake and cosolvent-induced water release is beneficial for a fundamental knowledge-based development of polymer-based nanodevices in thin film geometry. With proper parameter tuning, such as by salt addition, desired properties, such as an enhanced response, can be implemented for the limited set of established polymers without the need to design new polymers for a special purpose. Consequently, it is highly desirable to be able to attribute the complex response behavior of polymer thin films in the presence of salts to the properties of the involved ions and their corresponding specific ion effects in future work.

8. Summary and Outlook

Thermoresponsive polymers are promising candidates for a variety of applications, particularly in areas such as drug delivery, tissue engineering, and sensors. These applications take advantage of their ability to undergo a coil-to-globule transition upon temperature change, i.e., switching between a hydrophilic and a hydrophobic state. Fundamental to the applicability of a thermoresponsive polymer is the reversibility of the transition and the responsiveness of the material. In this regard, thermoresponsive polymer thin films offer improved stability and controlled thickness compared to conventional polymer solutions, which can lead to improved performance in applications requiring precise spatial and temporal control. In addition, thin films can provide a more homogeneous and conformable surface compared to polymer brushes deposited on substrates, allowing for uniform interactions across the surface. Furthermore, unlike bulk materials, thin films allow for enhanced responsiveness, making them ideal for dynamic environments where rapid changes occur. These changes can include not only the temperature of the environment, but also the humidity and composition of the vapor atmosphere. In this context, thermoresponsive, hydrophilic polymer thin films offer, in addition to responding to temperature changes, the possibility of incorporating polar solvent molecules such as water to form a hydrogel network. For such multi-responsive hydrogel thin films, the response behavior is accompanied by volume changes upon external stimuli. The different degrees of swelling of the thin film can thus be easily detected, facilitating their use in mechanical devices. Since the responsiveness of a system is the key property determining the applicability of a material, the tuning thereof has become a wide field of research. In general, a simple, inexpensive, and non-toxic tuning approach is advantageous for large-scale manufacturing of devices based on hydrogel thin films. Inspired by the early work of Hofmeister on the effect of salts on the solubility of proteins in aqueous solution, the addition of salts is considered to be a promising choice to tune the properties of a given material. The ability of the added ions to interact with solvent molecules as well as with functional groups of the polymer can influence fundamental properties of the thin film response. This includes the water uptake behavior to form a hydrogel or more complex phenomena such as the response to cononsolvency conditions.

In the first research project investigated in this thesis, the water uptake behavior of the thermoresponsive homopolymer PNIPMAM in thin film geometry is studied. It is successfully demonstrated that the response to a water vapor atmosphere can be significantly influenced by the addition of a small amount of salt during the fabrication process. Specifically, the influence of two different magnesium salts with ClO_4^- and NO_3^- anions is compared, with the more chaotropic anion being ClO_4^-. While the thickness of salt-free PNIPMAM increases by about 29% during the swelling process, the addition of $Mg(ClO_4)_2$ leads to an increase of about 37%. However, the addition of $Mg(NO_3)_2$ results in an even greater final swelling increase of 125% over the same swelling time. The evolution of the macroscopic response behavior in terms of film thickness evolution is followed by static and time-resolved ToF-NR measurements. By contrast variation between the solvent and the polymer, the vertical material distribution and the solvent volume fraction inside the films are determined. For both salt-containing PNIPMAM thin films, an initial rapid water uptake is observed, followed by a slower second stage until an equilibrium is reached. According to the SLD profiles, a homogeneous vertical material distribution in the bulk region is observed for the dry and swollen films, with short-range deviations at the interfaces towards the substrate and the vapor atmosphere. XRR measurements before and after the swelling experiment reveal no diffusion of ions towards either interface and further confirm the reversibility of the swelling process. The deviations of the observed vertical material distribution must therefore be caused by the solvent distribution. In order to relate the macroscopic film changes to the underlying molecular interaction processes during the swelling process, *in situ* FTIR measurements are performed. The analysis is performed in terms of peak area evolution and peak position shifts of the IR signals related to the functional groups of the polymer as well as to the solvent and the added ions. The solvent buildup within the polymer matrix and the hydration of each functional group are determined. While D_2O is incorporated during the swelling process, H_2O is released from the thin film. Furthermore, in contrast to the previously studied PNIPAM, PNIPMAM does not show H/D exchange at the protic amide moiety, indicating that the additional methyl group at the polymer backbone of PNIPMAM causes steric hindrance in the side chains. However, it is noteworthy that the salt-containing PNIPMAM thin films show different peak positions for the amide group in the dry state. It is believed that the Mg^{2+} cations are able to weakly coordinate or form cation-dipole complexes with the amide groups. Overall, as analyzed by the changes in peak position shifts, all functional groups of the polymer as well as the anion are hydrated during the swelling process. By further evaluating the FTIR spectra by 2D correlation analysis, the sequence of hydration events for a salt-free as well as for the salt-containing PNIPMAM thin films are determined. In the case of the salt-containing films, the anion

is hydrated prior to the functional groups of the polymer. Interestingly, the hydration sequence for the polymer reveals that changes to the hydrophobic alkyl moieties occur more rapidly than changes to the polar amide functionality. Again, this indicates that the amide group is due to the steric hindrance of the methyl group at the polymer backbone less solvent accessible. Combining the findings from ToF-NR and FTIR investigations, two hydration stages of the polymer thin films can be identified. Initially, a rapid water uptake is observed, accompanied by a strong increase in film thickness, which is attributed to the hydration of the anions and the hydrophobic hydration of the polymer. Once the polymer network is sufficiently loosened and able to move and rearrange, the sterically hindered amide groups become solvent-accessible, ending in a thermodynamically favorable equilibrium.

In the second research project, the study of the influence of salts on the response of PNIPMAM thin films to saturated solvent vapor atmospheres is extended. After studying the influence of the anion in the first research project, the second project deals with the influence of the cations of a salt, namely $NaClO_4$ and $Mg(ClO_4)_2$. In addition, the analysis of the response behavior is extended to a cononsolvency-induced collapse transition of a previously water swollen thin film. Cononsolvency conditions are realized by changing from a D_2O to a mixed D_2O-acetone vapor atmosphere with a volume-to-volume ratio of 9:1. While the swelling behavior of the $Mg(ClO_4)_2$-containing PNIPMAM thin film shows great resemblance with the first study, the $NaClO_4$-containing PNIPMAM thin film exhibits an even larger final thickness increase of over 177% throughout the swelling time. Similarly, the swelling process of the thin film samples is subdivided into two stages, i.e., an initial rapid water uptake followed by a slower equilibrium formation, which is again investigated by the combination of ToF-NR and FTIR experiments. Furthermore, static and time-resolved ToF-NR measurements during the collapse process again reveal a strong difference in the film response for the different salts. The system containing $Mg(ClO_4)_2$ contracted by 9%, whereas the system containing $NaClO_4$ contracted by 51%. Nevertheless, both systems shrink to the same remaining swelling ratio of about 134% within the first 15 min after the onset of contraction. The evolution of the solvent content during contraction shows a rapid release of D_2O molecules, while acetone is initially incorporated followed by the formation of an equilibrium with a lower acetone content. For connecting the macroscopic film changes to the underlying molecular interactions, FTIR measurements are performed. The FTIR spectra confirm the release of D_2O molecules as acetone is incorporated during the collapse process. Furthermore, the IR signals originating from the polymer and the anion shift upon changing from a D_2O to a mixed D_2O-acetone vapor atmosphere, indicating that the hydration shells formed around each

species change upon acetone addition. 2D FTIR correlation analysis reveals the sequence of events during the collapse process. First, acetone molecules are incorporated into the thin films followed by the disarrangement of the solvation shell around the perchlorate anions. Next, acetone-amide interactions develop, accompanied by amide-amide interactions, which again become favored during the contraction, while D_2O is ejected from the film.

In summary, a low-cost and simple approach is presented to adjust the responsiveness of a polymer thin film to a changing environment. The swelling behavior of PNIPMAM thin films in a water vapor atmosphere with the addition of $Mg(ClO_4)_2$, $Mg(NO_3)_2$ or $NaClO_4$ shows strong differences. While a low concentration of $Mg(ClO_4)_2$ already leads to a slightly higher swelling degree compared to a salt-free PNIPMAM thin film, the same concentration of $Mg(NO_3)_2$ or $NaClO_4$ increases the swelling ratio even further. Furthermore, the volume contraction of the thin films induced by cononsolvency conditions for the polymer is shown to be sensitive to salt addition. In all cases, the addition of salt leads to a more pronounced collapse of the thin films compared to a salt-free film, with $NaClO_4$ having the strongest film contraction. Therefore, $NaClO_4$ is found to enhance the responsiveness of a PNIPMAM thin film to a D_2O vapor atmosphere as well as to a mixed D_2O-acetone vapor atmosphere. Regarding the Hofmeister series for polymers in aqueous solution in the presence of salts, a more dominant effect for anions compared to cations and a higher polymer solubility for more chaotropic ions is expected. However, the effects appear to be more complex for polymers in thin film geometry, where no trend along the Hofmeister series is identified. The investigation of the cononsolvency effect reveals that by cosolvent addition an equilibrated solvent composition within the film forms and that interactions between the polymer with both solvents develop. Despite the low uptake of cosolvent inside the film, the strong film response indicates a high sensitivity of the system. Theories explaining the cononsolvency effect based on the formation of solvent-cosolvent clusters would therefore require a very strong influence of the cosolvent on the bulk water, even at low concentrations. Furthermore, theories based on the explanation of competitive binding between the two solvents to the polymer are statistically hampered by the low cosolvent content. The development of polymer-cosolvent and the simultaneous depletion of polymer-water interactions, as observed in this work during the collapse rather indicates preferential adsorption of the cosolvent to the polymer. Still the complex interplay between the components prevents ruling out the individual theories conclusively. Therefore, intelligent system design is crucial to unravel the underlying interaction mechanisms of the individual components to gain unambiguous insights.
Based on the findings presented in this thesis, the cononsolvency effect as well as the influ-

ence of specific ion effects on the performance of stimuli-responsive polymers in thin film geometry are important subjects for more extensive research in the future. Identifying trends in the highly complex behavior of the presented class of functional materials is essential to enable the targeted design of devices with the desired properties. Therefore, the present investigation should be extended to other thermoresponsive polymers, e.g., related derivatives of PNIPMAM. Likewise, for the cononsolvency effect, the volume phase transition of polymer thin films should be investigated for other solvent-cosolvent combinations and volume fractions. Furthermore, the importance of the order of the vapor series needs to be taken into consideration, i.e., swelling in water and collapsing in water-cosolvent mixtures versus swelling in the cosolvent and collapsing in water-cosolvent mixtures. In the light of future applications, the addition of salts has proven to be a promising tuning parameter greatly facilitating to adjust the responsiveness of a given system. Consequently, assessing the ability of other salts to influence the response behavior is attractive for the design of functional materials, thereby possibly also identifying trends in an ion series. Naturally, the concentration of the added salts process and even the combination of different salts in the fabrication are further factors to consider.

A. Effect of Magnesium Salts on the Swelling Behavior

Appendix A is based on and reprinted with permission from J. Reitenbach, C. Geiger, P. Wang, A. Vagias, R. Cubitt, D. Schanzenbach, A. Laschewsky, C. M. Papadakis, P. Müller-Buschbaum, Effect of Magnesium Salts with Chaotropic Anions on the Swelling Behavior of PNIPMAM Thin Films, *Macromolecules* 2023, 56, 567-577; DOI: 10.1021/acs.macromol.2c02282.

In the following the supplementary 2D FTIR correlation spectra for the analysis presented in Chapter 6 are given. In order to investigate the sequence of hydration events of salt-free and $Mg(ClO_4)_2$- or $Mg(NO_3)_2$-containing PNIPMAM thin films in a D_2O vapor atmosphere, prominent IR signals originating from the solvent D_2O, the individual functional groups of the polymer as well as from the anions are investigated. Furthermore, by cross-correlating the signals obtained for different moieties, the relative order between the signals can be determined. By combining the obtained relative orders between two moieties, the overall sequence of hydration events is deduced. For this purpose, Figures A.2-A.6 show the synchronous and asynchronous 2D FTIR correlation spectra for the hydrophobic alkyl groups of the polymer, the amide functional group of the polymer, and the anions of the added salts. While Figures A.1–A.3 show the correlation spectra for the individual moieties with themselves, Figures A.4–A.6 show the cross correlation between the aforementioned moieties.

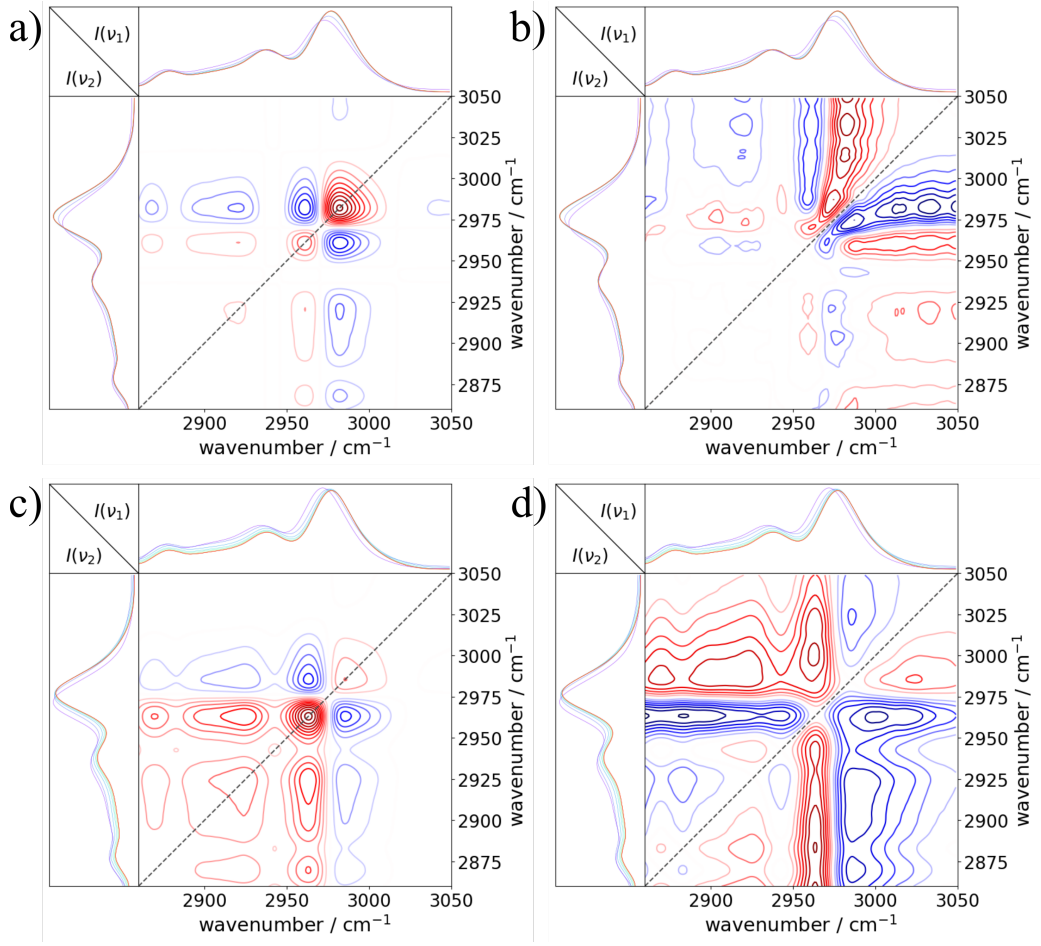

Figure A.1.: (a,c) Synchronous and (b,d) asynchronous 2D FTIR correlation plots of the $Mg(ClO_4)_2$-containing PNIPMAM film (top) and of the $Mg(NO_3)_2$-containing PNIPMAM film (bottom) in the wavenumber range between 2860 and 3050 cm^{-1} for the $\nu_{asym}(C-H_3)$, $\nu_{asym}(C-H_2)$, and $\nu_{sym}(C-H_3)$ signals coming from the isopropyl group of the side chain and the polymer backbone for the first 10 spectra taken in the interval from 0 to 35 min. Areas colored in red indicate positive correlation and areas colored in blue negative correlation. Reprinted with permission from Ref. [167]. Copyright 2023 American Chemical Society.

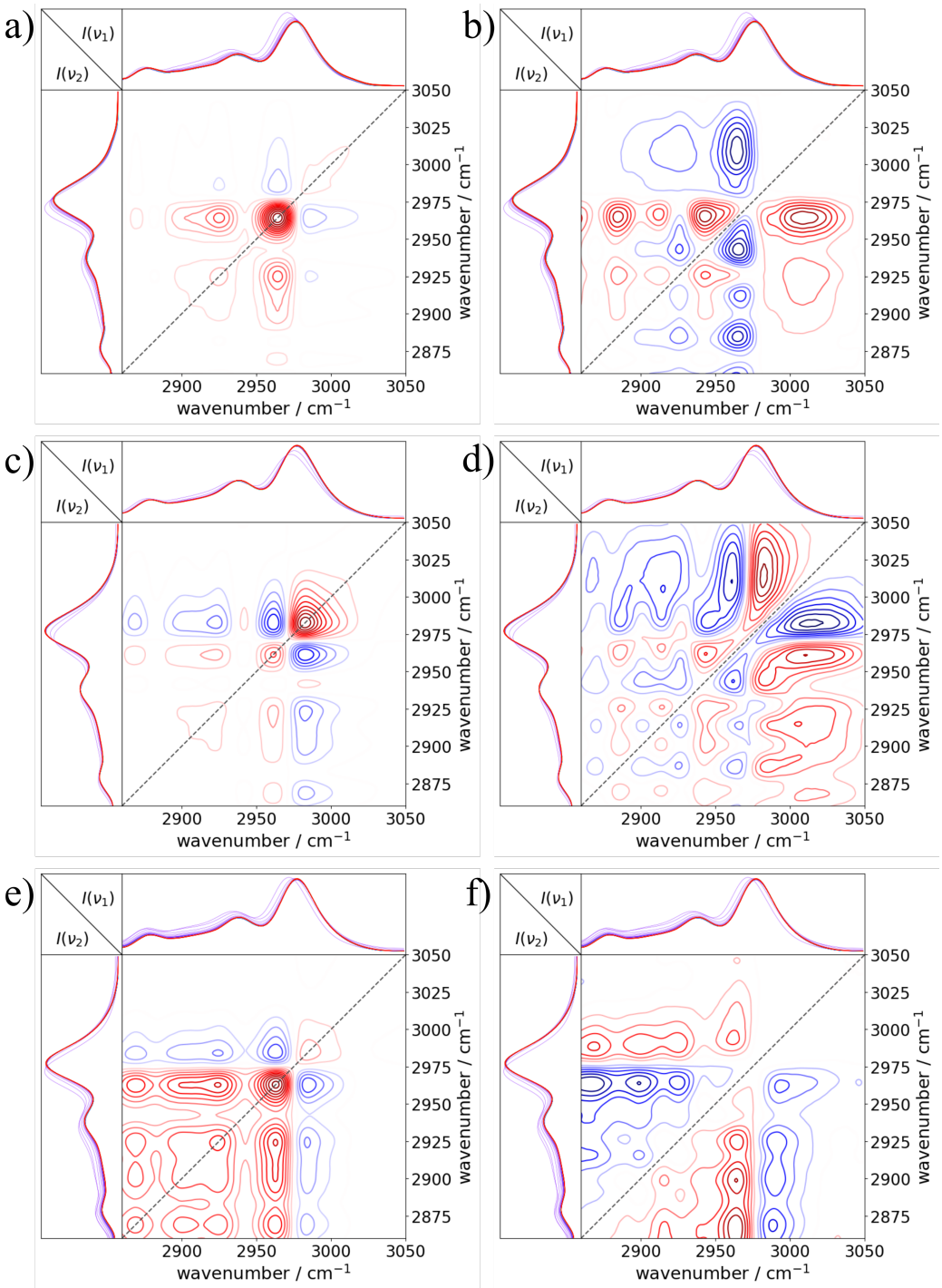

Figure A.2.: (a,c,e) Synchronous and (b,d,f) asynchronous 2D FTIR correlation plots of the pure PNIPMAM film (top), of the $Mg(ClO_4)_2$-containing PNIPMAM film (middle) and of the $Mg(NO_3)_2$-containing PNIPMAM film (bottom) in the wavenumber range between 2860 and 3050 cm^{-1} for $\nu_{asym}(C-H_3)$, $\nu_{asym}(C-H_2)$, and $\nu_{sym}(C-H_3)$ signals coming from the isopropyl group of the side chain and the polymer backbone for all collected spectra. Areas colored in red indicate positive correlation and areas colored in blue negative correlation. Reprinted with permission from Ref. [167]. Copyright 2023 American Chemical Society.

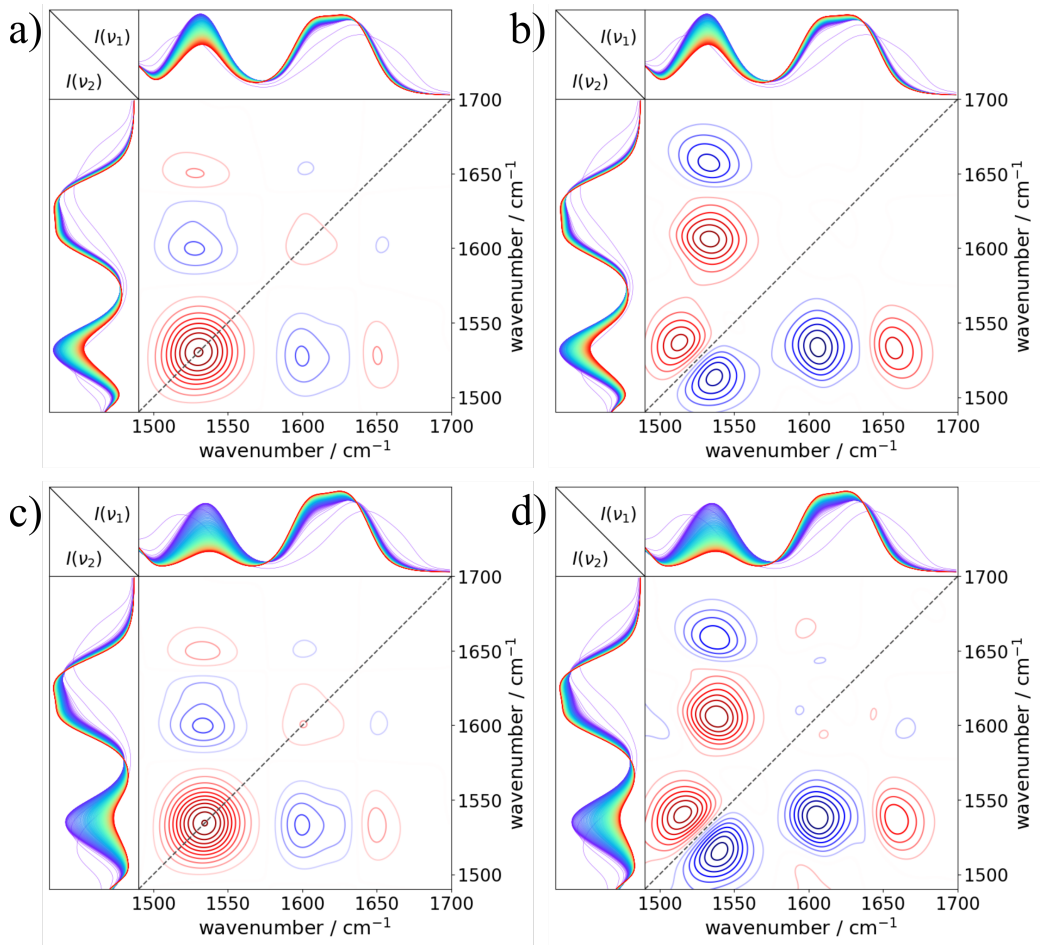

Figure A.3.: (a,c) Synchronous and (b,d) asynchronous 2D FTIR correlation plots of the $Mg(ClO_4)_2$-containing PNIPMAM film (top) and of the $Mg(NO_3)_2$-containing PNIPMAM film (bottom) in the wavenumber range between 1490 and 1700 cm^{-1} for the signals of amide I and amide II for all collected spectra. Areas colored in red indicate positive correlation and areas colored in blue negative correlation. Reprinted with permission from Ref. [167]. Copyright 2023 American Chemical Society.

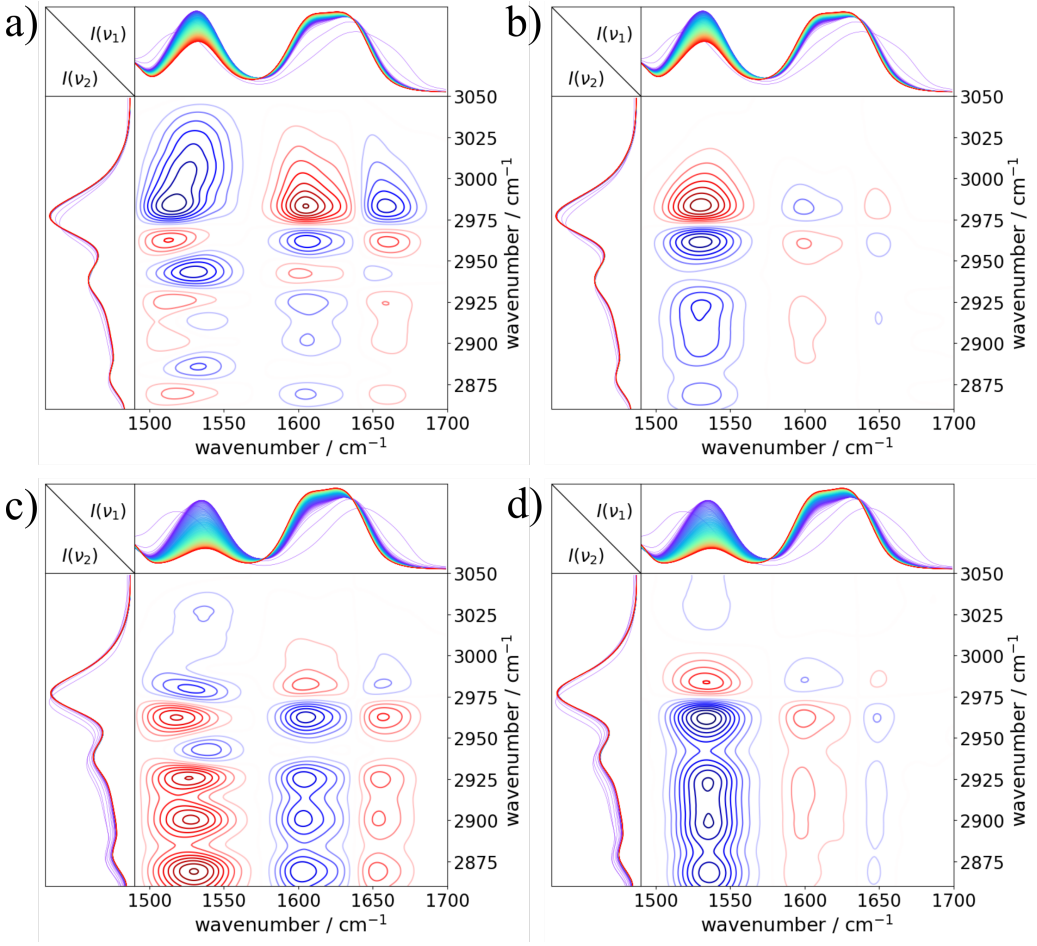

Figure A.4.: (a,c) Synchronous and (b,d) asynchronous 2D FTIR correlation plots of the $Mg(ClO_4)_2$-containing PNIPMAM film (top) and of the $Mg(NO_3)_2$-containing PNIPMAM film (bottom) in the wavenumber range between 1490 and 1700 cm^{-1}, and between 2860 and 3050 cm^{-1}, for amide I, amide II, $\nu_{asym}(C-H_3)$, $\nu_{asym}(C-H_2)$, and $\nu_{sym}(C-H_3)$ signals for all collected spectra. Areas colored in red indicate positive correlation and areas colored in blue negative correlation. Reprinted with permission from Ref. [167]. Copyright 2023 American Chemical Society.

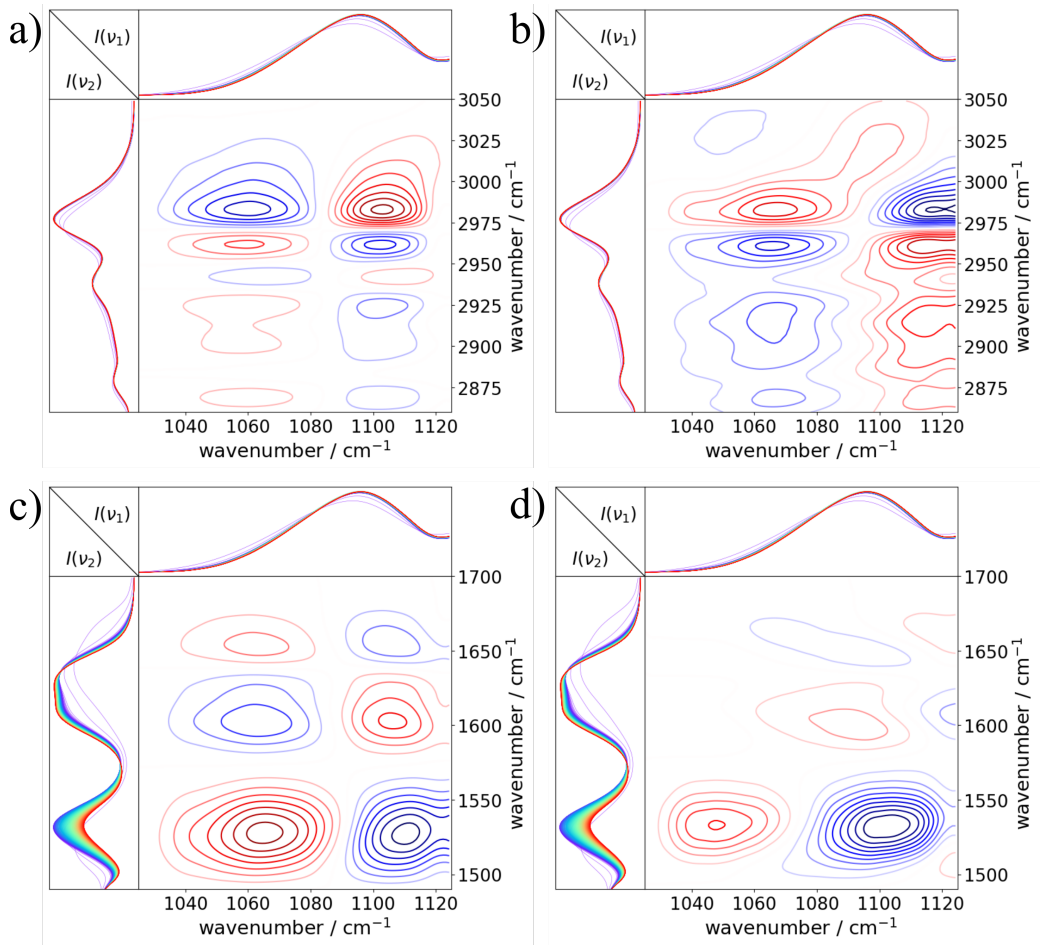

Figure A.5.: (a,c) Synchronous and (b,d) asynchronous 2D FTIR correlation plots of the $Mg(ClO_4)_2$-containing PNIPMAM film in the wavenumber range between 1030 and 1130 cm^{-1}, and between 2860 and 3050 cm^{-1} (top), also between 1030 and 1130 cm^{-1}, and between 1490 and 1700 cm^{-1} (bottom), for $\nu_{asym}(ClO_4^-)$, $\nu_{asym}(C-H_3)$, $\nu_{asym}(C-H_2)$, and $\nu_{sym}(C-H_3)$, amide I and amide II signals for all collected spectra. Areas colored in red indicate positive correlation and areas colored in blue negative correlation. Reprinted with permission from Ref. [167]. Copyright 2023 American Chemical Society.

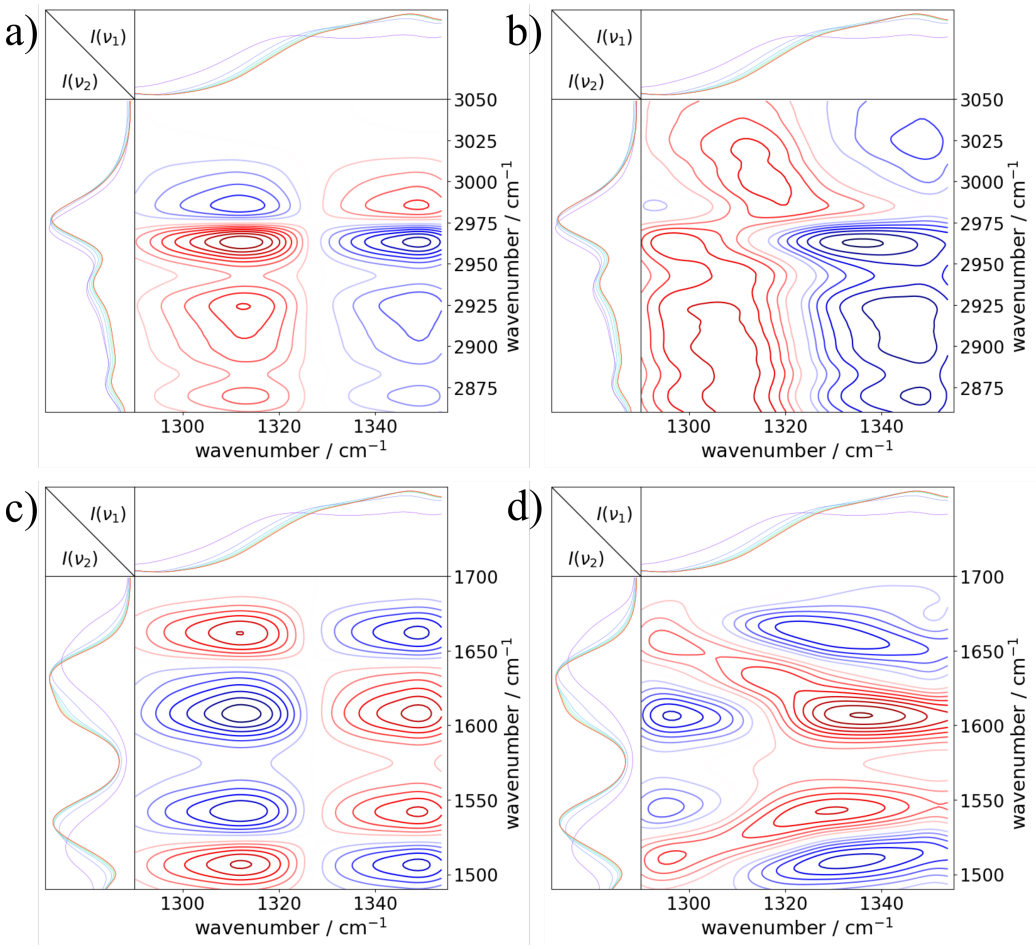

Figure A.6.: (a,c) Synchronous and (b,d) asynchronous 2D FTIR correlation plots of the $Mg(NO_3)_2$-containing PNIPMAM film in the wavenumber range between 1290 and 1355 cm^{-1}, and between 2860 and 3050 cm^{-1} (top), also between 1290 and 1355 cm^{-1}, and 1490 and 1700 cm^{-1} (bottom), for $\nu_{asym}(NO_3^-)$, $\nu_{asym}(C-H_3)$, $\nu_{asym}(C-H_2)$, and $\nu_{sym}(C-H_3)$, amide I and amide II signals for the first 10 spectra taken in the interval from 0 to 35 min. Areas colored in red indicate positive correlation and areas colored in blue negative correlation. Reprinted with permission from Ref. [167]. Copyright 2023 American Chemical Society.

B. Salt-Mediated Tuning of the Cononsolvency Response Behavior

Appendix B is based on and reprinted with permission from J. Reitenbach, P. Wang, L. F. Huber, S. A. Wegener, R. Cubitt, D. Schanzenbach, A. Laschewsky, C. M. Papadakis, P. Müller-Buschbaum, Salt-Mediated Tuning of the Cononsolvency Response Behavior of PNIPMAM Thin Films, *Macromolecules* 2024, 57, 10635-10647; DOI: 10.1021/acs.macromol.4c02053 licensed under CC BY 4.0.

In the following, supplementary information for the conducted GISAXS measurements and 2D FTIR correlation analysis is given. GISAXS measurements are performed on salt-free and $Mg(ClO_4)_2$- or $NaClO_4$-containing PNIPMAM thin films to verify the lateral uniformity of the salt distribution inside the polymer thin films, for which the corresponding 2D GISAXS images are shown in Figure B.1. For this, horizontal line cuts at the Yoneda peak region of the polymer are analyzed (Figure B.2). Additionally, 2D FTIR correlation spectra are investigated to determine the sequence of solvation events during the swelling and the collapse process of the salt-containing polymer thin films. Figure B.3 shows the synchronous and asynchronous 2D FTIR correlation plots for the swelling process of the $NaClO_4$-containing PNIPMAM thin film, whereas Figure B.4 shows the data for the $Mg(ClO_4)_2$-containing PNIPMAM thin film. Additionally, Figure B.5 presents the 2D FTIR correlation plots for the collapse process of a $Mg(ClO_4)_2$-containing PNIPMAM thin film.

GISAXS of Salt-free and Salt-Containing PNIPMAM Thin Films

GISAXS measurements are performed with a Ganesha SAXSLAB laboratory X-ray instrument. It is equipped with a Cu X-ray source (Xenocs GeniX3D, $\lambda_{\mathrm{Cu\ K\alpha}} = 1.5406$ Å) with an energy of 8.04 keV and an area detector (Pilatus 300k, Dectris) with dimensions of 72×72 pixels. The sample detector distance (SDD) is set to 1046 mm, and the GISAXS measurements are acquired for 18 h with an incident angle of 0.4°. The X-ray SLD of the polymer is calculated to be 10.37×10^{-6} Å^{-2}, which corresponds to a critical angle of

0.16°. Horizontal line cuts are performed at the Yoneda peak region of the polymer, and for statistical purposes, the left and right parts are accumulated.

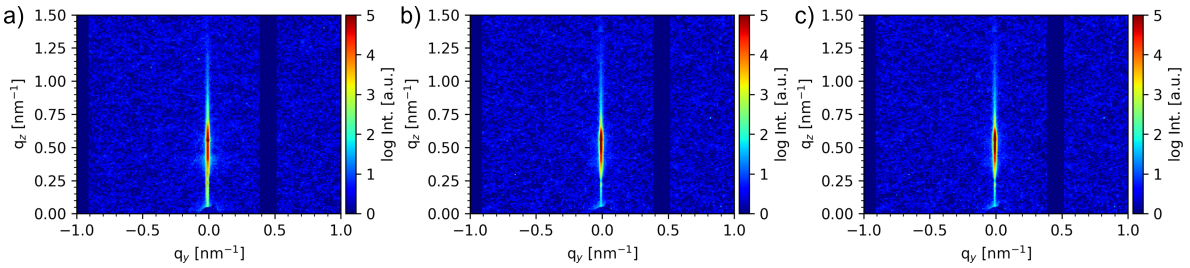

Figure B.1.: 2D GISAXS data of (a) a salt-free PNIPMAM thin film, (b) a $Mg(ClO_4)_2$-containing PNIPMAM thin film, and (c) a $NaClO_4$-containing PNIPMAM thin film. Reprinted with permission from Ref. [231], licensed under CC BY 4.0.

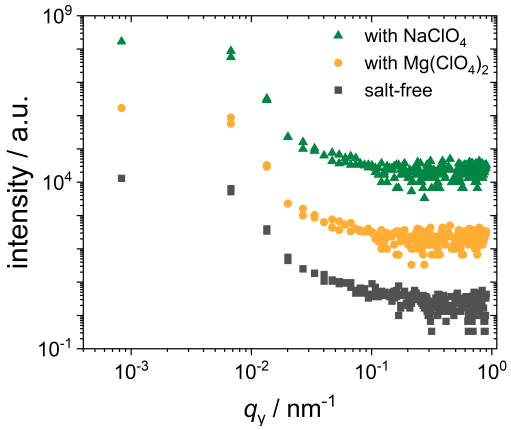

Figure B.2.: Horizontal line cuts of the 2D GISAXS data for a salt-free PNIPMAM thin film (black), a $Mg(ClO_4)_2$-containing PNIPMAM thin film (orange), and a $NaClO_4$-containing PNIPMAM thin film (green). The curves are shifted along the y-axis for clarity of presentation. Reprinted with permission from Ref. [231], licensed under CC BY 4.0.

2D FTIR Correlation Plots

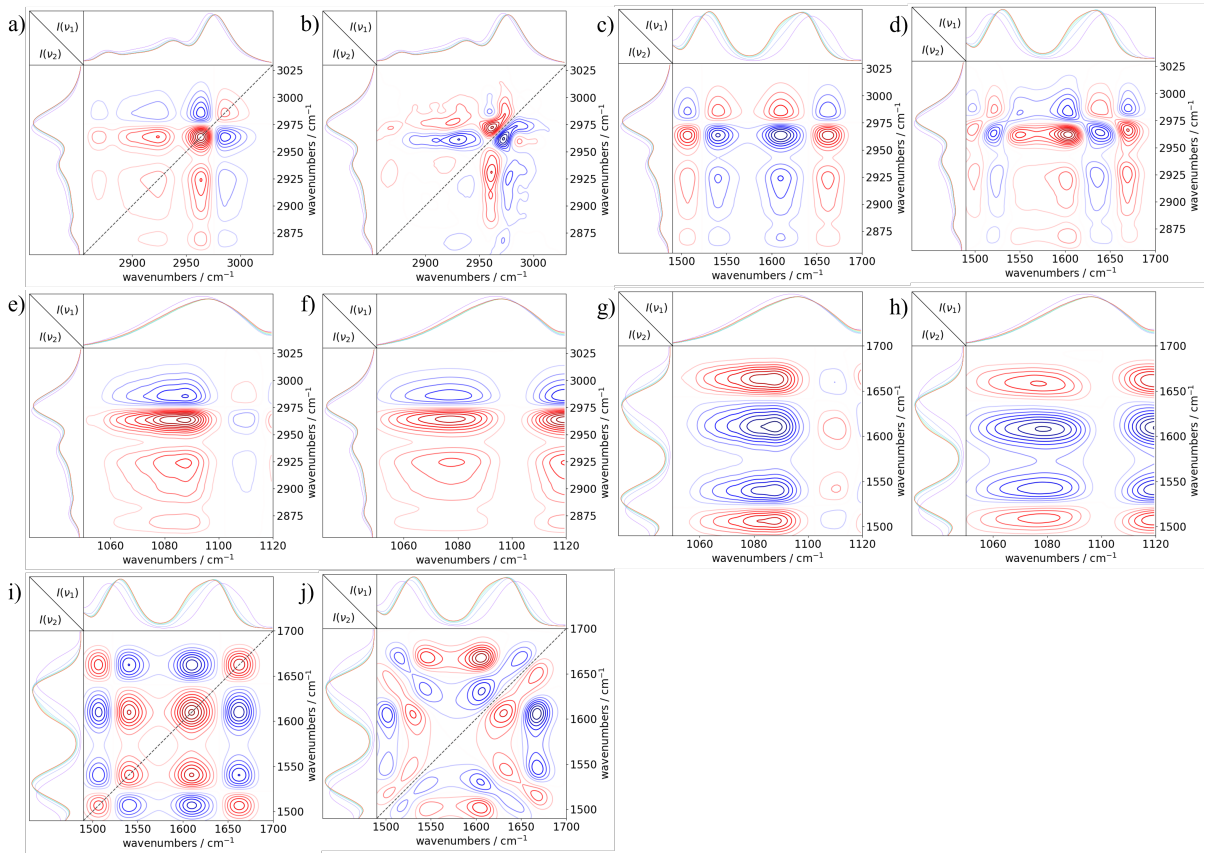

Figure B.3.: 2D FTIR correlation plots for the swelling process of the $NaClO_4$-containing PNIPMAM film. (a,b) Synchronous and asynchronous spectra in the wavenumber range between 2855 and 3030 cm^{-1} for the $\nu_{sym/asym}(C-H_3)$ and $\nu_{asym}(C-H_2)$ signals originating from the isopropyl group of the side chain and polymer backbone. (c,d) Synchronous and asynchronous spectra in the wavenumber range between 1490 and 1700 cm^{-1} and between 2855 and 3030 cm^{-1} for the amide I, amide II, $\nu_{sym/asym}(C-H_3)$ and $\nu_{asym}(C-H_2)$ signals. (e,f) Synchronous and asynchronous spectra in the wavenumber range between 1050 and 1120 cm^{-1} and between 2855 and 3030 cm^{-1} for the $\nu_{asym}(ClO_4{}^-)$, $\nu_{sym/asym}(C-H_3)$ and $\nu_{asym}(C-H_2)$ signals. (g,h) Synchronous and asynchronous spectra in the wavenumber range between 1050 and 1120 cm^{-1} and between 1490 and 1700 cm^{-1} for the $\nu_{asym}(ClO_4{}^-)$, amide I, and amide II signals. (i,j) Synchronous and asynchronous spectra in the wavenumber range between 1490 and 1700 cm^{-1} for the amide I and amide II signals. All correlation plots are shown by analyzing the first 10 spectra taken in the interval from 0 to 35 min. Positive correlation is indicated in red and negative correlation in blue. Reprinted with permission from Ref. [231], licensed under CC BY 4.0.

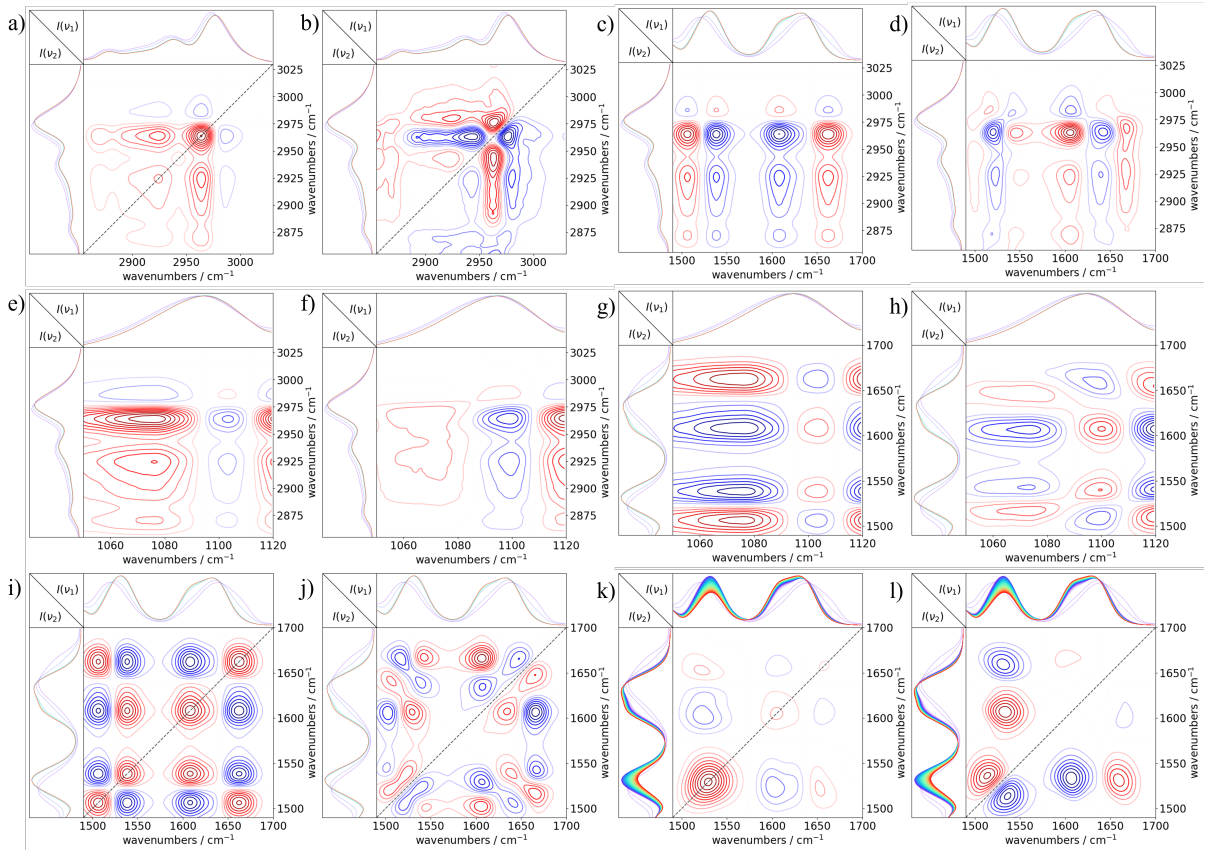

Figure B.4.: 2D FTIR correlation plots for the swelling process of the $Mg(ClO_4)_2$-containing PNIPMAM film. (a,b) Synchronous and asynchronous spectra in the wavenumber range between 2855 and 3030 cm^{-1} for the $\nu_{sym/asym}(C-H_3)$ and $\nu_{asym}(C-H_2)$ signals originating from the isopropyl group of the side chain and polymer backbone. (c,d) Synchronous and asynchronous spectra in the range between 1490 and 1700 cm^{-1} and between 2855 and 3030 cm^{-1} for the amide I, amide II, $\nu_{sym/asym}(C-H_3)$ and $\nu_{asym}(C-H_2)$ signals. (e,f) Synchronous and asynchronous spectra in the range between 1050 and 1120 cm^{-1} and between 2855 and 3030 cm^{-1} for the $\nu_{asym}(ClO_4^-)$, $\nu_{sym/asym}(C-H_3)$ and $\nu_{asym}(C-H_2)$ signals. (g,h) Synchronous and asynchronous spectra between 1050 and 1120 cm^{-1} and between 1490 and 1700 cm^{-1} for the $\nu_{asym}(ClO_4^-)$, amide I, and amide II signals. (i,j) Synchronous and asynchronous spectra between 1490 and 1700 cm^{-1} for the amide I and amide II signals. (k,l) Synchronous and asynchronous spectra between 1490 and 1700 cm^{-1} for the amide I and amide II signals. (a-j) Correlation plots are shown by analyzing the first 10 spectra taken in the interval from 0 to 35 min, while (k,l) plots are shown by analyzing the entire spectra. Positive correlation is indicated in red and negative correlation in blue. Reprinted with permission from Ref. [231], licensed under CC BY 4.0.

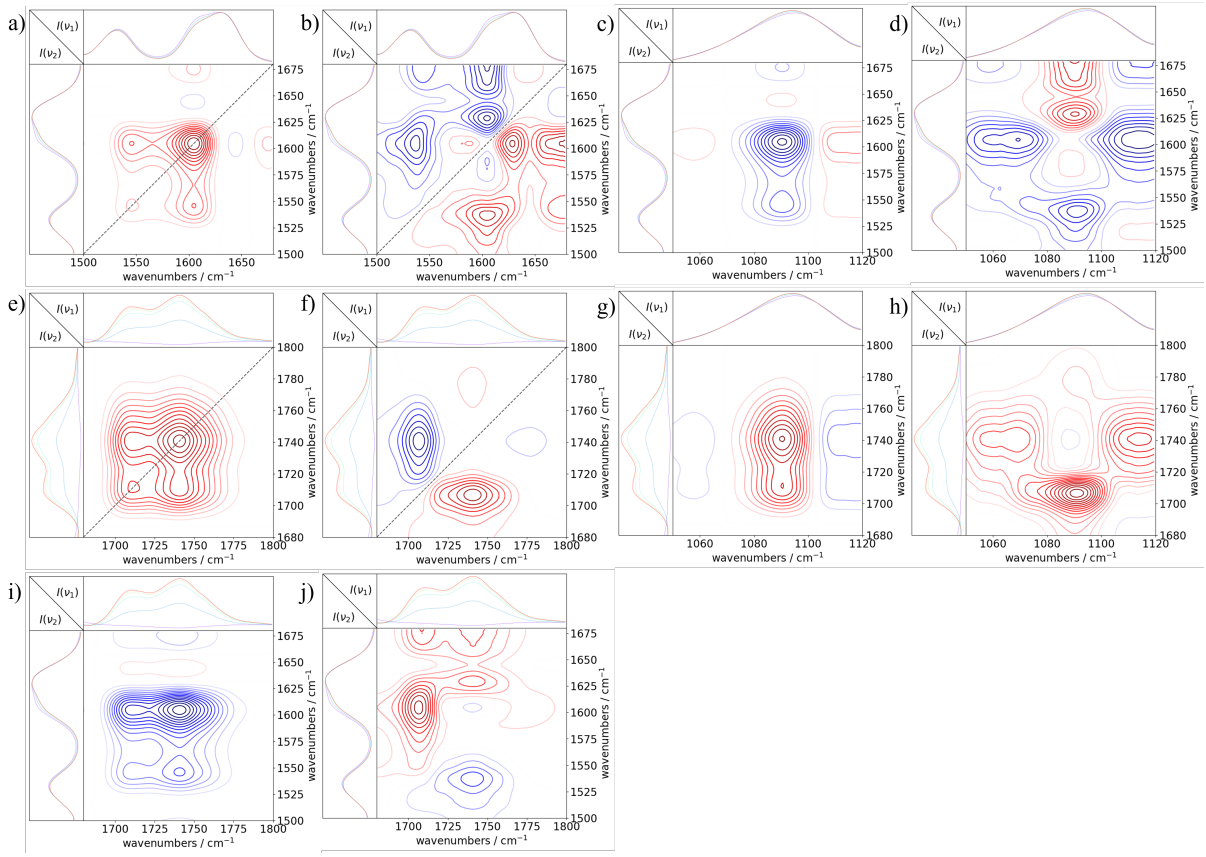

Figure B.5.: 2D FTIR correlation plots for the collapse process of the $Mg(ClO_4)_2$-containing PNIPMAM film. (a,b) Synchronous and asynchronous spectra in the wavenumber range between 1500 and 1680 cm^{-1} for the amide I and amide II signals. (c,d) Synchronous and asynchronous spectra in the wavenumber range between 1050 and 1120 cm^{-1} and between 1500 and 1680 cm^{-1} for the $\nu_{asym}(ClO_4^-)$, amide I, and amide II signals. (e,f) Synchronous and asynchronous spectra in the wavenumber range between 1680 and 1800 cm^{-1} for the $\nu(Me_2C{=}O)$ signals originating from the acetone molecules. (g,h) Synchronous and asynchronous spectra in the wavenumber range between 1050 and 1120 cm^{-1} and between 1680 and 1800 cm^{-1} for the $\nu_{asym}(ClO_4^-)$, and $\nu(Me_2C{=}O)$ signals. (i,j) Synchronous and asynchronous spectra in the wavenumber range between 1680 and 1800 cm^{-1} and between 1500 and 1680 cm^{-1} for the $\nu(Me_2C{=}O)$, amide I, and amide II signals. All correlation plots are shown by analyzing the first 6 spectra taken in the interval from 0 to 20 min. Positive correlation is indicated in red and negative correlation in blue. Reprinted with permission from Ref. [231], licensed under CC BY 4.0.

References

[1] O. Bertrand, J. F. Gohy, "Photo-responsive polymers: Synthesis and applications", *Polymer Chemistry* **2017**, *8*, 52–73, DOI 10.1039/c6py01082b.

[2] S. Dai, P. Ravi, K. C. Tam, "pH-Responsive polymers: Synthesis, properties and applications", *Soft Matter* **2008**, *4*, 435–449, DOI 10.1039/b714741d.

[3] S. Bharadwaj, B.-J. Niebuur, K. Nothdurft, W. Richtering, N. F. van der Vegt, C. M. Papadakis, "Cononsolvency of thermoresponsive polymers: where we are now and where we are going", *Soft Matter* **2022**, *18*, 2884–2909, DOI 10.1039/d2sm00146b.

[4] V. V. Khutoryanskiy, T. K. Georgiou, *Temperature-responsive polymers*, John Wiley & Sons, Ltd., Nashville, **2018**, DOI 10.1002/9781119157830.

[5] C. Katsuno, A. Konda, K. Urayama, T. Takigawa, M. Kidowaki, K. Ito, "Pressure-responsive polymer membranes of slide-ring gels with movable cross-links", *Advanced Materials* **2013**, *25*, 4636–4640, DOI 10.1002/adma.201301252.

[6] T. Hiratani, O. Kose, W. Y. Hamad, M. J. Maclachlan, "Stable and sensitive stimuli-responsive anisotropic hydrogels for sensing ionic strength and pressure", *Materials Horizons* **2018**, *5*, 1076–1081, DOI 10.1039/c8mh00586a.

[7] M. A. Stuart, W. T. Huck, J. Genzer, M. Müller, C. Ober, M. Stamm, G. B. Sukhorukov, I. Szleifer, V. V. Tsukruk, M. Urban, F. Winnik, S. Zauscher, I. Luzinov, S. Minko, "Emerging applications of stimuli-responsive polymer materials", *Nature Materials* **2010**, *9*, 101–113, DOI 10.1038/nmat2614.

[8] I. Tokarev, S. Minko, "Stimuli-responsive hydrogel thin films", *Soft Matter* **2009**, *5*, 511–524, DOI 10.1039/b813827c.

[9] D. Mukherji, C. M. Marques, K. Kremer, "Smart responsive polymers: fundamentals and design principles", *Annual Review of Condensed Matter Physics* **2020**, *11*, 271–299, DOI 10.1146/annurev-conmatphys-031119-050618.

[10] A. K. Bajpai, S. K. Shukla, S. Bhanu, S. Kankane, "Responsive polymers in controlled drug delivery", *Progress in Polymer Science* **2008**, *33*, 1088–1118, DOI 10.1016/j.progpolymsci.2008.07.005.

[11] M. Wei, Y. Gao, X. Li, M. J. Serpe, "Stimuli-responsive polymers and their applications", *Polymer Chemistry* **2017**, *8*, 127–143, DOI 10.1039/c6py01585a.

[12] L. Hu, Q. Zhang, X. Li, M. J. Serpe, "Stimuli-responsive polymers for sensing and actuation", *Materials Horizons* **2019**, *6*, 1774–1793, DOI 10.1039/c9mh00490d.

[13] M. L. Galbraith, J. D. Madura, "Identifying trends in hydration behavior for modifications to the hydrophobicity of poly(n-isopropylacrylamide)", *Journal of Molecular Graphics and Modelling* **2017**, *78*, 168–175, DOI 10.1016/j.jmgm.2017.09.021.

[14] N. Hu, C. Chen, E. Metwalli, L. Bießmann, C. Herold, J. Fu, R. Cubitt, Q. Zhong, P. Müller-Buschbaum, "Hydration and thermal response kinetics of a cross-linked thermoresponsive copolymer film on a hydrophobic PAN substrate coating probed by *in situ* neutron reflectivity", *Langmuir* **2021**, *37*, 6819–6829, DOI 10.1021/acs.langmuir.1c00931.

[15] D. Roy, W. L. Brooks, B. S. Sumerlin, "New directions in thermoresponsive polymers", *Chemical Society Reviews* **2013**, *42*, 7214–7243, DOI 10.1039/c3cs35499g.

[16] S. Furyk, Y. Zhang, D. Ortiz-Acosta, P. S. Cremer, D. E. Bergbreiter, "Effects of end group polarity and molecular weight on the lower critical solution temperature of poly(*N*-isopropylacrylamide)", *Journal of Polymer Science Part A: Polymer Chemistry* **2006**, *44*, 1492–1501, DOI 10.1002/pola.21256.

[17] Y. Xia, N. A. Burke, H. D. Stöver, "End group effect on the thermal response of narrow-disperse poly(*N*-isopropylacrylamide) prepared by atom transfer radical polymerization", *Macromolecules* **2006**, *39*, 2275–2283, DOI 10.1021/ma0519617.

[18] Y. Katsumoto, Y. Etoh, N. Shimoda, "Phase diagrams of stereocontrolled poly(*N*,*N*-diethylacrylamide) in water", *Macromolecules* **2010**, *43*, 3120–3121, DOI 10.1021/ma902673z.

[19] K. Nishi, T. Hiroi, K. Hashimoto, K. Fujii, Y.-S. Han, T.-H. Kim, Y. Katsumoto, M. Shibayama, "SANS and DLS study of tacticity effects on hydrophobicity and phase separation of poly(*N*-isopropylacrylamide)", *Macromolecules* **2013**, *46*, 6225–6232, DOI 10.1021/ma401349v.

[20] Y. Zhang, S. Furyk, D. E. Bergbreiter, P. S. Cremer, "Specific ion effects on the water solubility of macromolecules: PNIPAM and the Hofmeister series", *Journal of the American Chemical Society* **2005**, *127*, 14505–14510, DOI 10.1021/ja0546424.

[21] Y. Zhang, S. Furyk, L. B. Sagle, Y. Cho, D. E. Bergbreiter, P. S. Cremer, "Effects of Hofmeister anions on the LCST of PNIPAM as a function of molecular weight", *Journal of Physical Chemistry C* **2007**, *111*, 8916–8924, DOI 10.1021/jp0690603.

[22] H. G. Schild, M. Muthukumar, D. A. Tirrell, "Cononsolvency in mixed aqueous solutions of Poly(*N*-isopropylacrylamide)", *Macromolecules* **1991**, *24*, 948–952, DOI 10.1021/ma00004a022.

[23] S. Z. Moghaddam, E. Thormann, "The Hofmeister series: Specific ion effects in aqueous polymer solutions", *Journal of Colloid and Interface Science* **2019**, *555*, 615–635, DOI 10.1016/j.jcis.2019.07.067.

[24] K. P. Gregory, G. R. Elliott, H. Robertson, A. Kumar, E. J. Wanless, G. B. Webber, V. S. J. Craig, G. G. Andersson, A. J. Page, "Understanding specific ion effects and the Hofmeister series", *Physical Chemistry Chemical Physics* **2022**, *24*, 12682–12718, DOI 10.1039/d2cp00847e.

[25] F. Hofmeister, "Zur Lehre von der Wirkung der Salze", *Archiv für Experimentelle Pathologie und Pharmakologie* **1888**, *24*, 247–260, DOI 10.1007/BF01838161.

[26] W. Kunz, J. Henle, B. W. Ninham, "'Zur Lehre von der Wirkung der Salze' (about the science of the effect of salts): Franz Hofmeister's historical papers", *Current Opinion in Colloid and Interface Science* **2004**, *9*, 19–37, DOI 10.1016/j.cocis.2004.05.005.

[27] Y. Zhang, P. S. Cremer, "Chemistry of Hofmeister anions and osmolytes", *Annual Review of Physical Chemistry* **2010**, *61*, 63–83, DOI 10.1146/annurev.physchem.59.032607.093635.

[28] E. Wischerhoff, T. Zacher, A. Laschewsky, E. D. Rekaï, "Direct observation of the lower critical solution temperature of surface-attached thermo-responsive hydrogels by surface plasmon resonance", *Angewandte Chemie - International Edition* **2000**, *39*, 4602–4604, DOI 10.1002/1521-3773(20001215)39:24<4602::AID-ANIE4602>3.0.CO;2-E.

[29] K. Dušek, M. Dušková-Smrčková, "Volume phase transition in gels: its discovery and development", *Gels* **2020**, *6*, 1–12, DOI 10.3390/gels6030022.

[30] M. A. Haq, Y. Su, D. Wang, "Mechanical properties of PNIPAM based hydrogels: A review", *Materials Science and Engineering C* **2017**, *70*, 842–855, DOI 10.1016/j.msec.2016.09.081.

[31] T. R. Hoare, D. S. Kohane, "Hydrogels in drug delivery: Progress and challenges", *Polymer* **2008**, *49*, 1993–2007, DOI 10.1016/j.polymer.2008.01.027.

[32] A. C. Hunter, S. M. Moghimi, "Smart polymers in drug delivery: A biological perspective", *Polymer Chemistry* **2017**, *8*, 41–51, DOI 10.1039/c6py00676k.

[33] F.-M. Cheng, H.-X. Chen, H.-D. Li, "Recent progress on hydrogel actuators", *Journal of Materials Chemistry B* **2021**, *9*, 1762–1780, DOI 10.1039/d0tb02524k.

[34] V. Chytrý, M. Netopilík, M. Bohdanecký, K. Ulbrich, "Phase transition parameters of potential thermosensitive drug release systems based on polymers of *N*-alkylmethacrylamides", *Journal of Biomaterials Science Polymer Edition* **1997**, *8*, 817–824, DOI 10.1163/156856297X00010.

[35] P. Gu, B. Li, B. Wu, J. Wang, P. Müller-Buschbaum, Q. Zhong, "Controlled hydration, transition, and drug release realized by adjusting layer thickness in alginate-Ca^{2+}/poly(*N*-isopropylacrylamide) interpenetrating polymeric network hydrogels on cotton fabrics", *ACS Biomaterials Science and Engineering* **2020**, *6*, 5051–5060, DOI 10.1021/acsbiomaterials.0c00756.

[36] K. J. Hogan, A. G. Mikos, "Biodegradable thermoresponsive polymers: Applications in drug delivery and tissue engineering", *Polymer* **2020**, *211*, 123063, DOI 10.1016/j.polymer.2020.123063.

[37] E. Djokpé, W. Vogt, "*N*-isopropylacrylamide and *N*-isopropylmethacrylamide: Cloud points of mixtures and copolymers", *Macromolecular Chemistry and Physics* **2001**, *202*, 750–757, DOI 10.1002/1521-3935(20010301)202:5<750::AID-MACP750>3.0.CO;2-8.

[38] I. Berndt, W. Richtering, "Doubly temperature sensitive core-shell microgels", *Macromolecules* **2003**, *36*, 8780–8785, DOI 10.1021/ma034771+.

[39] N. S. Vishnevetskaya, V. Hildebrand, B.-J. Niebuur, I. Grillo, S. K. Filippov, A. Laschewsky, P. Müller-Buschbaum, C. M. Papadakis, ""Schizophrenic" micelles from doubly thermoresponsive polysulfobetaine-*b*-poly(*N*-isopropylmethacrylamide) di-block copolymers", *Macromolecules* **2017**, *50*, 3985–3999, DOI 10.1021/acs.macro-mol.7b00356.

[40] C.-H. Ko, K.-L. Claude, B.-J. Niebuur, F. A. Jung, J.-J. Kang, D. Schanzenbach, H. Frielinghaus, L. C. Barnsley, B. Wu, V. Pipich, A. Schulte, P. Müller-Buschbaum, A. Laschewsky, C. M. Papadakis, "Temperature-dependent phase behavior of the thermoresponsive polymer poly(*N*-isopropylmethacrylamide) in an aqueous solution", *Macromolecules* **2020**, *53*, 6816–6827, DOI 10.1021/acs.macromol.0c01256.

[41] Y. Hannappel, L. Wiehemeier, M. Dirksen, T. Kottke, T. Hellweg, "Smart microgels from unconventional acrylamides", *Macromolecular Chemistry and Physics* **2021**, *222*, 2100067, DOI 10.1002/macp.202100067.

[42] S. Fujishige, K. Kubota, I. Ando, "Phase transition of aqueous solutions of poly(*N*-isopropylacrylamide) and poly(*N*-isopropylmethacrylamide)", *The Journal of Physical Chemistry* **1989**, *93*, 3311–3313, DOI 10.1021/j100345a085.

[43] K. Kubota, K. Hamano, N. Kuwahara, "Characterization of poly(*N*-isopropylmethacrylamide) in water", *Polymer Journal* **1990**, *22*, 1051–1057, DOI 10.1295/polymj.22.1051.

[44] J. Dybal, M. Trchová, P. Schmidt, "The role of water in structural changes of poly(*N*-isopropylacrylamide) and poly(*N*-isopropylmethacrylamide) studied by FTIR, Raman spectroscopy and quantum chemical calculations", *Vibrational Spectroscopy* **2009**, *51*, 44–51, DOI 10.1016/j.vibspec.2008.10.003.

[45] M. K. Kokufuta, S. Sato, E. Kokufuta, "LCST behavior of copolymers of *N*-isopropylacrylamide and *N*-isopropylmethacrylamide in water", *Colloid and Polymer Science* **2012**, *290*, 1671–1681, DOI 10.1007/s00396-012-2706-y.

[46] J. Cowie, V. Arrighi, *Polymers: Chemistry and Physics of Modern Materials*, 3rd ed., CRC Press, **2007**, DOI 10.1201/9781420009873.

[47] G. Strobl, *The Physics of Polymers*, 3rd ed., Springer Berlin, Heidelberg, **2007**, DOI 10.1007/978-3-540-68411-4.

[48] P. J. Flory, "Thermodynamics of high polymer solutions", *Journal of Chemical Physics* **1942**, *10*, 51–61, DOI 10.1007/s12045-017-0481-2.

[49] M. L. Huggins, "Theory of solutions of high polymers", *Journal of the American Chemical Society* **1942**, *64*, 1712–1719, DOI 10.1021/ja01259a068.

[50] M. L. Huggins, "Some properties of solutions of long-chain compounds", *Journal of Physical Chemistry* **1942**, *46*, 151–158, DOI 10.1007/BF01300681.

[51] I. Teraoka, *Polymer Solutions*, John Wiley & Sons, Inc., New York, **2002**, DOI 10.1002/0471224510.

[52] P. Knychała, K. Timachova, M. Banaszak, N. P. Balsara, "50th Anniversary perspective: Phase behavior of polymer solutions and blends", *Macromolecules* **2017**, *50*, 3051–3065, DOI 10.1021/acs.macromol.6b02619.

[53] P. R. Lang, Y. Liu, *Soft Matter at Aqueous Interfaces*, Springer, Cham, **2016**, DOI 10.1007/978-3-319-24502-7.

[54] R. Rubinstein, R. H. Colby, *Polymer Physics*, Oxford University Press, Oxford, **2003**, DOI 10.1093/oso/9780198520597.001.0001.

[55] K. Binder, M. Müller, P. Virnau, L. G. MacDowell, "Polymer + solvent systems: Phase diagrams, interface free energies, and nucleation", *Advances in Polymer Science* **2005**, *173*, 1–110, DOI 10.1007/b99426.

[56] R. Pamies, K. Zhu, A.-L. Kjøniksen, B. Nyström, "Thermal response of low molecular weight poly-(*N*-isopropylacrylamide) polymers in aqueous solution", *Polymer Bulletin* **2009**, *62*, 487–502, DOI 10.1007/s00289-008-0029-4.

[57] A. Halperin, M. Kröger, F. M. Winnik, "Poly(*N*-isopropylacrylamide) phase diagrams: Fifty years of research", *Angewandte Chemie - International Edition* **2015**, *54*, 15342–15367, DOI 10.1002/anie.201506663.

[58] C. Zhao, Z. Ma, X. X. Zhu, "Rational design of thermoresponsive polymers in aqueous solutions: A thermodynamics map", *Progress in Polymer Science* **2019**, *90*, 269–291, DOI 10.1016/j.progpolymsci.2019.01.001.

[59] R. O. R. Costa, R. F. S. Freitas, "Phase behavior of poly(*N*-isopropylacrylamide) in binary aqueous solutions", *Polymer* **2002**, *43*, 5879–5885, DOI 10.1016/S0032-3861(02)00507-4.

[60] F. Tanaka, T. Koga, H. Kojima, N. Xue, F. M. Winnik, "Preferential adsorption and Co-nonsolvency of thermoresponsive polymers in mixed solvents of water/methanol", *Macromolecules* **2011**, *44*, 2978–2989, DOI 10.1021/ma102695n.

[61] C. Scherzinger, A. Schwarz, A. Bardow, K. Leonhard, W. Richtering, "Cononsolvency of poly-*N*-isopropyl acrylamide (PNIPAM): Microgels versus linear chains and macrogels", *Current Opinion in Colloid and Interface Science* **2014**, *19*, 84–94, DOI 10.1016/j.cocis.2014.03.011.

[62] D. Mukherji, M. Wagner, M. D. Watson, S. Winzen, T. E. de Oliveira, C. M. Marques, K. Kremer, "Relating side chain organization of PNIPAm with its conformation in aqueous methanol", *Soft Matter* **2016**, *12*, 7995–8003, DOI 10.1039/c6sm01789d.

[63] M. Yang, K. Zhao, "Cononsolvency of poly(*N*-isopropylacrylamide) in methanol aqueous solution – insight by dielectric spectroscopy", *Journal of Polymer Science Part B: Polymer Physics* **2017**, *55*, 1227–1234, DOI 10.1002/polb.24377.

[64] N. Xue, X.-P. Qiu, V. Aseyev, F. M. Winnik, "Nonequilibrium liquid-liquid phase separation of poly(*N*-isopropylacrylamide) in water/methanol mixtures", *Macromolecules* **2017**, *50*, 4446–4453, DOI 10.1021/acs.macromol.7b00407.

[65] V. Y. Grinberg, T. V. Burova, N. V. Grinberg, A. P. Moskalets, A. S. Dubovik, I. G. Plashchina, A. R. Khokhlov, "Energetics and mechanisms of poly(N-isopropylacrylamide) phase transitions in water-methanol solutions", *Macromolecules* **2020**, *53*, 10765–10772, DOI 10.1021/acs.macromol.0c02253.

[66] K. N. Raftopoulos, K. Kyriakos, M. Nuber, B.-J. Niebuur, O. Holderer, M. Ohl, O. Ivanova, S. Pasini, C. M. Papadakis, "Co-nonsolvency in concentrated aqueous solutions of PNIPAM: Effect of methanol on the collective and the chain dynamics", *Soft Matter* **2020**, *16*, 8462–8472, DOI 10.1039/d0sm01007c.

[67] C.-H. Ko, C. Henschel, G. P. Meledam, M. A. Schroer, R. Guo, L. Gaetani, P. Müller-Buschbaum, A. Laschewsky, C. M. Papadakis, "Co-nonsolvency effect in solutions of poly(methyl methacrylate)-*b*-poly(*N*-isopropylacrylamide) diblock copolymers in water/methanol mixtures", *Macromolecules* **2021**, *54*, 5825–5837, DOI 10.1021/acs.macromol.1c00512.

[68] A. Hüther, X. Xu, G. Maurer, "Swelling of *n*-isopropyl acrylamide hydrogels in water and aqueous solutions of ethanol and acetone", *Fluid Phase Equilibria* **2004**, *219*, 231–244, DOI 10.1016/j.fluid.2003.08.002.

[69] F. Wang, Y. Shi, S. Luo, Y. Chen, J. Zhao, "Conformational transition of poly(*N*-isopropylacrylamide) single chains in its cononsolvency process: A study by fluorescence correlation spectroscopy and scaling analysis", *Macromolecules* **2012**, *45*, 9196–9204, DOI 10.1021/ma301780f.

[70] M. J. A. Hore, B. Hammouda, Y. Li, H. Cheng, "Co-nonsolvency of poly(*n*-isopropylacrylamide) in deuterated water/ethanol mixtures", *Macromolecules* **2013**, *46*, 7894–7901, DOI 10.1021/ma401665h.

[71] I. Bischofberger, D. C. E. Calzolari, V. Trappe, "Co-nonsolvency of PNiPAM at the transition between solvation mechanisms", *Soft Matter* **2014**, *10*, 8288–8295, DOI 10.1002/9783527617050.

[72] H. A. Pérez-Ramírez, C. Haro-Pérez, G. Odriozola, "Effect of temperature on the Cononsolvency of poly(*N*-isopropylacrylamide) (PNIPAM) in aqueous 1-propanol", *ACS Applied Polymer Materials* **2019**, *1*, 2961–2972, DOI 10.1021/acsapm.9b00665.

[73] P.-W. Zhu, L. Chen, "Effects of cosolvent partitioning on conformational transitions and chain flexibility of thermoresponsive microgels", *Physical Review E* **2019**, *99*, 022501, DOI 10.1103/PhysRevE.99.022501.

[74] K. Mukae, M. Sakurai, S. Sawamura, K. Makino, S. W. Kim, I. Ueda, K. Shirahama, "Swelling of poly(N-isopropylacrylamide) gels in water-aprotic solvent mixtures", *Colloid & Polymer Science* **1994**, *272*, 655–663, DOI 10.1007/BF00659279.

[75] J. Hao, H. Cheng, P. Butler, L. Zhang, C. C. Han, "Origin of cononsolvency, based on the structure of tetrahydrofuran-water mixture", *The Journal of Chemical Physics* **2010**, *132*, 154902, DOI 10.1063/1.3381177.

[76] J. Wang, N. Wang, B. Liu, J. Bai, P. Gong, G. Ru, J. Feng, "Preferential adsorption of the additive is not a prerequisite for cononsolvency in water-rich mixtures", *Physical Chemistry Chemical Physics* **2017**, *19*, 30097–30106, DOI 10.1039/c7cp04384h.

[77] H. G. Schild, "Poly(*N*-isopropylacrylamide): experiment, theory and application", *Progress in Polymer Science* **1992**, *17*, 163–249, DOI 10.1016/0079-6700(92)90023-R.

[78] K. Van Durme, G. Van Assche, B. Van Mele, "Kinetics of demixing and remixing in poly(*N*-isopropylacrylamide)/water studied by modulated temperature DSC", *Macromolecules* **2004**, *37*, 9596–9605, DOI 10.1021/ma048472b.

[79] V. Aseyev, H. Tenhu, F. M. Winnik, "Non-ionic thermoresponsive polymers in water", *Advances in Polymer Science* **2011**, *242*, 29–89, DOI 10.1007/12_2010_57.

[80] G.-F. Luo, W.-H. Chen, X.-Z. Zhang, "100th Anniversary of macromolecular science viewpoint: Poly(*N*-isopropylacrylamide)-based thermally responsive micelles", *ACS Macro Letters* **2020**, *9*, 872–881, DOI 10.1021/acsmacrolett.0c00342.

[81] I. Alenichev, Z. Sedláková, M. Ilavský, "Swelling and mechanical behavior of charged poly(*N*-isopropylmethacrylamide) and poly(*N*-isopropylacrylamide) networks in water/ethanol mixtures. Cononsolvency effect", *Polymer Bulletin* **2007**, *58*, 191–199, DOI 10.1007/s00289-006-0586-3.

[82] H. Kouřilová, L. Hanyková, J. Spěváček, "NMR study of phase separation in D_2O/ethanol solutions of poly(*N*-isopropylmethacrylamide) induced by solvent composition and temperature", *European Polymer Journal* **2009**, *45*, 2935–2941, DOI 10.1016/j.eurpolymj.2009.06.011.

[83] C. Geiger, J. Reitenbach, C. Henschel, L. P. Kreuzer, T. Widmann, P. Wang, G. Mangiapia, J.-F. Moulin, C. M. Papadakis, A. Laschewsky, P. Müller-Buschbaum, "Ternary nanoswitches realized with multiresponsive PMMA-*b*-PNIPMAM films in mixed water/acetone vapor atmospheres", *Advanced Engineering Materials* **2021**, *23*, 2100191, DOI 10.1002/adem.202100191.

[84] L. P. Kreuzer, C. Lindenmeir, C. Geiger, T. Widmann, V. Hildebrand, A. Laschewsky, C. M. Papadakis, P. Müller-Buschbaum, "Poly(sulfobetaine) versus poly(*N*-isopropylmethacrylamide): Co-nonsolvency-type behavior of thin films in a water/methanol atmosphere", *Macromolecules* **2021**, *54*, 1548–1556, DOI 10.1021/acs.macromol.0c02281.

[85] P. Wang, C. Geiger, L. P. Kreuzer, T. Widmann, J. Reitenbach, S. Liang, R. Cubitt, C. Henschel, A. Laschewsky, C. M. Papadakis, P. Müller-Buschbaum, "Poly(sulfobetaine)-based diblock copolymer thin films in water/acetone atmosphere: Modulation of water hydration and co-nonsolvency-triggered film contraction", *Langmuir* **2022**, *38*, 6934–6948, DOI 10.1021/acs.langmuir.2c00451.

[86] C. Henschel, D. Schanzenbach, A. Laschewsky, C.-H. Ko, C. M. Papadakis, P. Müller-Buschbaum, "Thermoresponsive and co-nonsolvency behavior of poly(*N*-vinyl isobutyramide) and poly(*N*-isopropyl methacrylamide) as poly(*N*-isopropyl acrylamide) analogs in aqueous media", *Colloid and Polymer Science* **2023**, *301*, 703–720, DOI 10.1007/s00396-023-05083-4.

[87] G. Zhang, C. Wu, "The water/methanol complexation induced reentrant coil-to-globule-to-coil transition of individual homopolymer chains in extremely dilute solution", *Journal of the American Chemical Society* **2001**, *123*, 1376–1380, DOI 10.1021/ja003889s.

[88] I. Bischofberger, D. C. Calzolari, P. De Los Rios, I. Jelezarov, V. Trappe, "Hydrophobic hydration of poly-N-isopropyl acrylamide: A matter of the mean energetic state of water", *Scientific Reports* **2014**, *4*, 4377, DOI 10.1038/srep04377.

[89] F. Tanaka, T. Koga, F. M. Winnik, "Temperature-responsive polymers in mixed solvents: Competitive hydrogen bonds cause cononsolvency", *Physical Review Letters* **2008**, *101*, 028302, DOI 10.1103/PhysRevLett.101.028302.

[90] C. Dalgicdir, F. Rodríguez-Ropero, N. F. van der Vegt, "Computational calorimetry of PNIPAM cononsolvency in water/methanol mixtures", *Journal of Physical Chemistry B* **2017**, *121*, 7741–7748, DOI 10.1021/acs.jpcb.7b05960.

[91] J. Walter, J. Sehrt, J. Vrabec, H. Hasse, "Molecular dynamics and experimental study of conformation change of poly(*N*-isopropylacrylamide) hydrogels in mixtures of water and methanol", *Journal of Physical Chemistry B* **2012**, *116*, 5251–5259, DOI 10.1021/jp212357n.

[92] J. Heyda, A. Muzdalo, J. Dzubiella, "Rationalizing polymer swelling and collapse under attractive cosolvent conditions", *Macromolecules* **2013**, *46*, 1231–1238, DOI 10.1021/ma302320y.

[93] D. Mukherji, C. M. Marques, K. Kremer, "Polymer collapse in miscible good solvents is a generic phenomenon driven by preferential adsorption", *Nature Communications* **2014**, *5*, 4882, DOI 10.1038/ncomms5882.

[94] Y. Marcus, G. Hefter, "Ion pairing", *Chemical Reviews* **2006**, *106*, 4585–4621, DOI 10.1021/cr040087x.

[95] K. P. Gregory, E. J. Wanless, G. B. Webber, V. S. Craig, A. J. Page, "The electrostatic origins of specific ion effects: Quantifying the Hofmeister series for anions", *Chemical Science* **2021**, *12*, 15007–15015, DOI 10.1039/d1sc03568a.

[96] R. G. Pearson, "Hard and soft acids and bases", *Journal of the American Chemical Society* **1963**, *85*, 3533–3539, DOI 10.1021/ja00905a001.

[97] G. Jones, M. Dole, "The viscosity of aqueous solutions of the silicates of soda", *Journal of the American Chemical Society* **1929**, *51*, 2950–2964, DOI 10.1021/j150262a010.

[98] A. A. Zavitsas, "Properties of water solutions of electrolytes and nonelectrolytes", *Journal of Physical Chemistry B* **2001**, *105*, 7805–7817, DOI 10.1021/jp011053l.

[99] A. P. dos Santos, A. Diehl, Y. Levin, "Surface tensions, surface potentials, and the Hofmeister series of electrolyte solutions", *Langmuir* **2010**, *26*, 10778–10783, DOI 10.1021/la100604k.

[100] F. Cugia, S. Sedda, F. Pitzalis, D. F. Parsons, M. Monduzzi, A. Salis, "Are specific buffer effects the new frontier of Hofmeister phenomena? Insights from lysozyme adsorption on ordered mesoporous silica", *RSC Advances* **2016**, *6*, 94617–94621, DOI 10.1039/c6ra17356j.

[101] M. Mura, B. Humphreys, J. Gilbert, A. Salis, T. Nylander, "Cation and buffer specific effects on the DNA-lipid interaction", *Colloids and Surfaces B: Biointerfaces* **2023**, *223*, 113187, DOI 10.1016/j.colsurfb.2023.113187.

[102] M. Boström, D. R. M. Williams, P. R. Stewart, B. W. Ninham, "Hofmeister effects in membrane biology: The role of ionic dispersion potentials", *Physical Review E* **2003**, *68*, 041902, DOI 10.1103/PhysRevE.68.041902.

[103] K. D. Collins, "Ions from the Hofmeister series and osmolytes: Effects on proteins in solution and in the crystallization process", *Methods* **2004**, *34*, 300–311, DOI 10.1016/j.ymeth.2004.03.021.

[104] L. Abezgauz, K. Kuperkar, P. A. Hassan, O. Ramon, P. Bahadur, D. Danino, "Effect of Hofmeister anions on micellization and micellar growth of the surfactant cetylpyridinium chloride", *Journal of Colloid and Interface Science* **2010**, *342*, 83–92, DOI 10.1016/j.jcis.2009.08.045.

[105] A. Salis, D. Bilaničova, B. W. Ninham, M. Monduzzi, "Hofmeister effects in enzymatic activity: Weak and strong electrolyte influences on the activity of *candida rugosa* lipase", *Journal of Physical Chemistry B* **2007**, *111*, 1149–1156, DOI 10.1021/jp066346z.

[106] D. Bilaničová, A. Salis, B. W. Ninham, M. Monduzzi, "Specific anion effects on enzymatic activity in nonaqueous media", *Journal of Physical Chemistry B* **2008**, *112*, 12066–12072, DOI 10.1021/jp805451w.

[107] Y. Zhang, P. S. Cremer, "The inverse and direct Hofmeister series for lysozyme", *Proceedings of the National Academy of Sciences of the United States of America* **2009**, *106*, 15249–15253, DOI 10.1073/pnas.0907616106.

[108] V. Štěpánková, J. Paterová, J. Damborský, P. Jungwirth, R. Chaloupková, J. Heyda, "Cation-specific effects on enzymatic catalysis driven by interactions at the tunnel mouth", *Journal of Physical Chemistry B* **2013**, *117*, 6394–6402, DOI 10.1021/jp401506v.

[109] H. Zhao, "Protein stabilization and enzyme activation in ionic liquids: Specific ion effects", *Journal of Chemical Technology and Biotechnology* **2016**, *91*, 25–50, DOI 10.1002/jctb.4837.

[110] K. Garajová, A. Balogová, E. Dušeková, D. Sedláková, E. Sedlák, R. Varhač, "Correlation of lysozyme activity and stability in the presence of Hofmeister series anions", *Biochimica et Biophysica Acta* **2017**, *1865*, 281–288, DOI 10.1016/j.bbapap.2016.11.016.

[111] C. Carucci, F. Raccis, A. Salis, E. Magner, "Specific ion effects on the enzymatic activity of alcohol dehydrogenase from *saccharomyces cerevisiae*", *Physical Chemistry Chemical Physics* **2020**, *22*, 6749–6754, DOI 10.1039/c9cp06800g.

[112] M. Collu, C. Carucci, A. Salis, "Specific anion effects on lipase adsorption and enzymatic synthesis of biodiesel in nonaqueous media", *Langmuir* **2020**, *36*, 9465–9471, DOI 10.1021/acs.langmuir.0c01330.

[113] J. Heyda, J. Dzubiella, "Thermodynamic description of Hofmeister effects on the LCST of thermosensitive polymers", *Journal of Physical Chemistry B* **2014**, *118*, 10979–10988, DOI 10.1021/jp5041635.

[114] M. Jaspers, A. E. Rowan, P. H. Kouwer, "Tuning hydrogel mechanics using the Hofmeister effect", *Advanced Functional Materials* **2015**, *25*, 6503–6510, DOI 10.1002/adfm.201502241.

[115] B. A. Humphreys, E. J. Wanless, G. B. Webber, "Effect of ionic strength and salt identity on poly(*N*-isopropylacrylamide) brush modified colloidal silica particles", *Journal of Colloid and Interface Science* **2018**, *516*, 153–161, DOI 10.1016/j.jcis.2018.01.058.

[116] Y. Marcus, *Ions in Solution and their Solvation*, John Wiley & Sons, Inc., Hoboken, **2015**, DOI 10.1002/9781118892336.

[117] Y. Zhang, P. S. Cremer, "Interactions between macromolecules and ions: The Hofmeister series", *Current Opinion in Chemical Biology* **2006**, *10*, 658–663, DOI 10.1016/j.cbpa.2006.09.020.

[118] L. M. Pegram, M. T. Record, "Hofmeister salt effects on surface tension arise from partitioning of anions and cations between bulk water and the air-water interface", *Journal of Physical Chemistry B* **2007**, *111*, 5411–5417, DOI 10.1021/jp070245z.

[119] L. M. Pegram, M. T. Record, "The thermodynamic origin of Hofmeister ion effects", *Journal of Physical Chemistry B* **2008**, *112*, 9428–9436, DOI 10.1021/jp800816a.The.

[120] L. M. Pegram, M. T. Record, "Quantifying accumulation or exclusion of H^+, HO^-, and Hofmeister salt ions near interfaces", *Chemical Physical Letters* **2008**, *467*, 1–8, DOI 10.1016/j.coph.2007.10.002.Taste.

[121] L. M. Pegram, M. T. Record, "Using surface tension data to predict differences in surface and bulk concentrations of nonelectrolytes in water", *Journal of Physical Chemistry C* **2009**, *113*, 2171–2174.

[122] M. T. Record, E. Guinn, L. Pegram, M. Capp, "Introductory lecture: Interpreting and predicting Hofmeister salt ion and solute effects on biopolymer and model processes using the solute partitioning model", *Faraday Discussions* **2013**, *160*, 9–44, DOI 10.1039/c2fd20128c.

[123] P. J. Flory, J. Rehner, "Statistical mechanics of cross-linked polymer networks II. Swelling", *The Journal of Chemical Physics* **1943**, *11*, 521–526.

[124] A. Mateescu, Y. Wang, J. Dostalek, U. Jonas, "Thin hydrogel films for optical biosensor applications", *Membranes* **2012**, *2*, 40–69, DOI 10.3390/membranes2010040.

[125] G. D. Nicodemus, S. J. Bryant, "Cell encapsulation in biodegradable hydrogels for tissue engineering applications", *Tissue Engineering - Part B: Reviews* **2008**, *14*, 149–165, DOI 10.1089/ten.teb.2007.0332.

[126] M. Hamidi, A. Azadi, P. Rafiei, "Hydrogel nanoparticles in drug delivery", *Advanced Drug Delivery Reviews* **2008**, *60*, 1638–1649, DOI 10.1016/j.addr.2008.08.002.

[127] L. Ionov, "Hydrogel-based actuators: Possibilities and limitations", *Materials Today* **2014**, *17*, 494–503, DOI 10.1016/j.mattod.2014.07.002.

[128] G. Gerlach, M. Guenther, T. Härtling, "Hydrogel-based chemical and biochemical sensors - A review and tutorial paper", *IEEE Sensors Journal* **2021**, *21*, 12798–12807, DOI 10.1109/JSEN.2020.3042988.

[129] Y. Lee, W. J. Song, J.-Y. Sun, "Hydrogel soft robotics", *Materials Today Physics* **2020**, *15*, 100258, DOI 10.1016/j.mtphys.2020.100258.

[130] W. J. Smith, *Modern Optical Engineering*, 4th ed., McGraw-Hill Education, New York, **2008**.

[131] A. J. Jackson, "Introduction to small-angle neutron scattering and neutron reflectometry", *NIST Center for Neutron Research* **2008**, 1–24.

[132] J. Als-Nielsen, D. McMorrow, *Elements of Modern X-ray Physics*, 2nd ed., John Wiley & Sons, Ltd., **2011**, DOI 10.1002/9781119998365.

[133] F. Cousin, G. Fadda, "An introduction to neutron reflectometry", *EPJ Web of Conferences* **2020**, *236*, 04001, DOI 10.1051/epjconf/202023604001.

[134] D. Sivia, *Elementary Scattering Theory*, Oxford University Press, Oxford, **2011**, DOI 10.1093/acprof:oso/9780199228676.001.0001.

[135] J. Daillant, A. Gibaud, *X-ray and Neutron Reflectivity*, Springer Berlin, Heidelberg, **2009**, DOI 10.1007/978-3-540-88588-7.

[136] X.-L. Zhou, S.-H. Chen, "Theoretical foundation of X-ray and neutron reflectometry", *Physics Reports* **1995**, *257*, 223–348, DOI 10.1016/0370-1573(94)00110-O.

[137] D. K. G. de Boer, A. J. G. Leenaers, W. W. van den Hoogenhof, "Glancing-incidence X-ray analysis of thin-layered materials: A review", *X-Ray Spectometry* **1995**, *24*, 91–102, DOI 10.1002/xrs.1300240304.

[138] K. Stoev, K. Sakurai, "Recent theoretical models in grazing incidince X-ray reflectometry", *The Rigaku Journal* **1997**, *14*, 1–37.

[139] P. Müller-Buschbaum, "GISAXS and GISANS as metrology technique for understanding the 3D morphology of block copolymer thin films", *European Polymer Journal* **2016**, *81*, 470–493, DOI 10.1016/j.eurpolymj.2016.04.007.

[140] E. Chason, T. M. Mayer, "Thin film and surface characterization by specular X-ray reflectivity", *Critical Reviews in Solid State and Materials Sciences* **1997**, *22*, 1–67, DOI 10.1080/10408439708241258.

[141] H. Zabel, "X-ray and neutron reflectivity analysis of thin films and superlattices", *Applied Physics A* **1994**, *58*, 159–168, DOI 10.1007/BF00324371.

[142] M. W. Skoda, "Recent developments in the application of X-ray and neutron reflectivity to soft-matter systems", *Current Opinion in Colloid and Interface Science* **2019**, *42*, 41–54, DOI 10.1016/j.cocis.2019.03.003.

[143] M. D. Foster, "X-ray scattering methods for the study of polymer interfaces", *Critical Reviews in Analytical Chemistry* **1993**, *24*, 179–241, DOI 10.1080/10408349308-050553.

[144] L. G. Parratt, "Surface studies of solids by total reflection of x-rays", *Physical Review* **1954**, *95*, 359–369, DOI 10.1103/PhysRev.95.359.

[145] R. Storn, K. Price, "Differential evolution - A simple and efficient heuristic for global optimization over continuous spaces", *Journal of Global Optimization* **1997**, *11*, 341–359, DOI 10.1071/AP09004.

[146] G. Hölzer, M. Fritsch, M. Deutsch, J. Härtwig, E. Förster, "$K\alpha_{1,2}$ and $K\beta_{1,2}$ x-ray emission lines of the 3d transition metals", *Physical Review A* **1997**, *56*, 4554–4568, DOI 10.1103/PhysRevA.56.4554.

[147] G. F. Harrington, J. Santiso, "Back-to-Basics tutorial: X-ray diffraction of thin films", *Journal of Electroceramics* **2021**, *47*, 141–163, DOI 10.1007/s10832-021-00263-6.

[148] A. Nelson, "Co-refinement of multiple-contrast neutron/X-ray reflectivity data using *MOTOFIT*", *Journal of Applied Crystallography* **2006**, *39*, 273–276, DOI 10.1107/S0021889806005073.

[149] A. R. Nelson, S. W. Prescott, "Refnx: Neutron and X-ray reflectometry analysis in python", *Journal of Applied Crystallography* **2019**, *52*, 193–200, DOI 10.1107/S1600576718017296.

[150] J. Higgins, H. Benoît, H. Benoît, *Polymers and Neutron Scattering*, Clarendon Press, Oxford, **1996**.

[151] V. F. Sears, "Neutron scattering lengths and cross sections", *Neutron News* **1992**, *3*, 26–37, DOI 10.1080/10448639208218770.

[152] J. Dawidowski, J. R. Granada, J. R. Santisteban, F. Cantargi, L. A. R. Palomino in *Neutron Scattering – Fundamentals*, *Vol. 44*, Academic Press, San Diego, **2013**, pp. 471–528, DOI https://doi.org/10.1016/B978-0-12-398374-9.09989-7.

[153] R. Cubitt, G. Fragneto, "D17: The new reflectometer at the ILL", *Applied Physics A* **2002**, *74*, 329–331, DOI 10.1007/s003390201611.

[154] T. Saerbeck, R. Cubitt, A. Wildes, G. Manzin, K. H. Andersen, P. Gutfreund, "Recent upgrades of the neutron reflectometer D17 at ILL", *Journal of Applied Crystallography* **2018**, *51*, 249–256, DOI 10.1107/S160057671800239X.

[155] I. Bodnarchuk, S. Manoshin, S. Yaradaikin, V. Kazimirov, V. Bodnarchuk, "The effect of gravity on the resolution for time-of-flight specular neutron reflectivity", *Nuclear Instruments and Methods in Physics Research A* **2011**, *631*, 121–124, DOI 10.1016/j.nima.2010.12.074.

[156] R. Cubitt, T. Saerbeck, R. A. Campbell, R. Barker, P. Gutfreund, "An improved algorithm for reducing reflectometry data involving divergent beams or non-flat samples", *Journal of Applied Crystallography* **2015**, *48*, 2006–2011, DOI 10.1107/S1600576715019500.

[157] P. Gutfreund, T. Saerbeck, M. A. Gonzalez, E. Pellegrini, M. Laver, C. Dewhurst, R. Cubitt, "Towards generalized data reduction on a chopperbased time-of-flight neutron reflectometer", *Journal of Applied Crystallography* **2018**, *51*, 606–615, DOI 10.1107/S160057671800448X.

[158] P. W. Atkins, J. De Paula, J. Keeler, *Atkins' Physical Chemistry*, 11th ed., Oxford University Press, Oxford, **2018**.

[159] S. J. Jang, *Quantum Mechanics for Chemistry*, Springer, Cham, **2023**, DOI 10.1007/978-3-031-30218-3.

[160] M. A. Linne in *Spectroscopic Measurement*, Academic Press, London, **2024**, pp. 211–256, DOI 10.1016/B978-0-44-315474-4.00016-6.

[161] J. S. Gaffney, N. A. Marley, D. E. Jones in *Characterization of Materials*, John Wiley & Sons, Ltd., **2012**, pp. 1–33, DOI 10.1002/0471266965.com107.pub2.

[162] I. Noda, "Progress in two-dimensional (2D) correlation spectroscopy", *Journal of Molecular Structure* **2006**, *799*, 2–15, DOI 10.1016/j.molstruc.2006.03.053.

[163] I. Noda, "Techniques of two-dimensional (2D) correlation spectroscopy useful in life science research", *Biomedical Spectroscopy and Imaging* **2015**, *4*, 109–127, DOI 10.3233/bsi-150105.

[164] Y. Park, I. Noda, Y. M. Jung, "Two-dimensional correlation spectroscopy in polymer study", *Frontiers in Chemistry* **2015**, *3*, 1–16, DOI 10.3389/fchem.2015.00014.

[165] I. Noda, "Recent developments in two-dimensional (2D) correlation spectroscopy", *Chinese Chemical Letters* **2015**, *26*, 167–172, DOI 10.1016/j.cclet.2014.10.006.

[166] I. Noda, A. E. Dowrey, C. Marcott, G. M. Story, "Generalized two-dimensional correlation spectroscopy", *Applied Spectroscopy* **2000**, *54*, 236–248, DOI 10.1366/0003702001950454.

[167] J. Reitenbach, C. Geiger, P. Wang, A. Vagias, R. Cubitt, D. Schanzenbach, A. Laschewsky, C. M. Papadakis, P. Müller-Buschbaum, "Effect of magnesium salts with chaotropic anions on the swelling behavior of PNIPMAM thin films", *Macromolecules* **2023**, *56*, 567–577, DOI 10.1021/acs.macromol.2c02282.

[168] P. R. Griffiths, J. A. de Haseth, *Fourier Transform Infrared Spectrometry*, 2nd ed., John Wiley & Sons, Inc., Hoboken, **2006**, DOI 10.1002/047010631X.

[169] A. Dutta in *Spectroscopic Methods for Nanomaterials Characterization*, Elsevier, **2017**, pp. 73–93, DOI 10.1016/B978-0-323-46140-5.00004-2.

[170] T. Widmann, L. P. Kreuzer, G. Mangiapia, M. Haese, H. Frielinghaus, P. Müller-Buschbaum, "3D printed spherical environmental chamber for neutron reflectometry and grazing-incidence small-angle neutron scattering experiments", *Review of Scientific Instruments* **2020**, *91*, 113903, DOI 10.1063/5.0012652.

[171] L. P. Kreuzer, PhD thesis, Technical University of Munich, **2021**, p. 58.

[172] T. Widmann, L. P. Kreuzer, M. Kühnhammer, A. J. Schmid, L. Wiehemeier, S. Jaksch, H. Frielinghaus, O. Löhmann, H. Schneider, A. Hiess, R. von Klitzing, T. Hellweg, P. Müller-Buschbaum, "Flexible sample environment for the investigation of soft matter at the european spallation source: part II - The GISANS setup", *Applied Sciences* **2021**, *11*, 4036, DOI 10.3390/app11094036.

[173] K. Norrman, A. Ghanbari-Siahkali, N. B. Larsen, "Studies of spin-coated polymer films", *Annual Reports on the Progress of Chemistry - Section C* **2005**, *101*, 174–201, DOI 10.1039/b408857n.

[174] D. W. Schubert, T. Dunkel, "Spin coating from a molecular point of view: Its concentration regimes, influence of molar mass and distribution", *Materials Research Innovations* **2003**, *7*, 314–321, DOI 10.1007/s10019-003-0270-2.

[175] K. Bauri, M. Nandi, P. De, "Amino acid-derived stimuli-responsive polymers and their applications", *Polymer Chemistry* **2018**, *9*, 1257–1287, DOI 10.1039/c7py02014g.

[176] S. Chatterjee, P. C.-l. Hui, "Review of stimuli-responsive polymers in drug delivery and textile application", *Molecules* **2019**, *24*, 2547, DOI 10.3390/molecules24142547.

[177] E. M. White, J. Yatvin, J. B. Grubbs, J. A. Bilbrey, J. Locklin, "Advances in smart materials: Stimuli-responsive hydrogel thin films", *Journal of Polymer Science Part B: Polymer Physics* **2013**, *51*, 1084–1099, DOI 10.1002/polb.23312.

[178] Y. C. Wong, B. C. Ang, A. S. M. A. Haseeb, A. A. Baharuddin, Y. H. Wong, "Review-conducting polymers as chemiresistive gas sensing materials: A review", *Journal of The Electrochemical Society* **2020**, *167*, 037503, DOI 10.1149/2.0032003jes.

[179] A. Buchberger, S. Peterka, A. M. Coclite, A. Bergmann, "Fast optical humidity sensor based on hydrogel thin film expansion for harsh environment", *Sensors* **2019**, *19*, 999, DOI 10.3390/s19050999.

[180] M. R. Cavallari, L. M. Pastrana, C. D. F. Sosa, A. M. R. Marquina, J. E. E. Izquierdo, F. J. Fonseca, C. A. de Amorim, L. G. Paterno, I. Kymissis, "Organic thin-film transistors as gas sensors: A review", *Materials* **2021**, *14*, 3, DOI 10.3390/ma14010003.

[181] W. Wang, G. Kaune, J. Perlich, C. M. Papadakis, A. M. Bivigou Koumba, A. Laschewsky, K. Schlage, R. Röhlsberger, S. V. Roth, R. Cubitt, P. Müller-Buschbaum, "Swelling and switching kinetics of gold coated end-capped poly(*N*-isopropylacrylamide) thin films", *Macromolecules* **2010**, *43*, 2444–2452, DOI 10.1021/ma902637a.

[182] Y. Sakai, Y. Sadaoka, M. Matsuguchi, "Humidity sensors based on polymer thin films", *Sensors and Actuators B* **1996**, *35*, 85–90, DOI 10.1016/S0925-4005(96)02019-9.

[183] Y.-J. Kim, Y. T. Matsunaga, "Thermo-responsive polymers and their application as smart biomaterials", *Journal of Materials Chemistry B* **2017**, *5*, 4307–4321, DOI 10.1039/c7tb00157f.

[184] X. Zhang, L. P. Kreuzer, D. M. Schwaiger, M. Lu, Z. Mao, R. Cubitt, P. Müller-Buschbaum, Q. Zhong, "Abnormal fast dehydration and rehydration of light- and thermo-dual-responsive copolymer films triggered by UV radiation", *Soft Matter* **2021**, *17*, 2603–2613, DOI 10.1039/d0sm02007a.

[185] L. P. Kreuzer, T. Widmann, C. Geiger, P. Wang, A. Vagias, J. E. Heger, M. Haese, V. Hildebrand, A. Laschewsky, C. M. Papadakis, P. Müller-Buschbaum, "Salt-dependent phase transition behavior of doubly thermoresponsive poly(sulfobetaine)-based diblock copolymer thin films", *Langmuir* **2021**, *37*, 9179–9191, DOI 10.1021/acs.langmuir.1c01342.

[186] P. Lavalle, J.-C. Voegel, D. Vautier, B. Senger, P. Schaaf, V. Ball, "Dynamic aspects of films prepared by a sequential deposition of species: Perspectives for smart and responsive materials", *Advanced Materials* **2011**, *23*, 1191–1221, DOI 10.1002/adma.201003309.

[187] C. Geiger, J. Reitenbach, L. P. Kreuzer, T. Widmann, P. Wang, R. Cubitt, C. Henschel, A. Laschewsky, C. M. Papadakis, P. Müller-Buschbaum, "PMMA-*b*-PNIPAM thin films display cononsolvency-driven response in mixed water/methanol vapors", *Macromolecules* **2021**, *54*, 3517–3530, DOI 10.1021/acs.macromol.1c00021.

[188] M. Heskins, J. E. Guillet, "Solution properties of poly(N-isopropylacrylamide)", *Journal of Macromolecular Science Part A* **1968**, *2*, 1441–1455, DOI 10.1080/10601326808051910.

[189] R. Alexander, E. C. F. Ko, A. J. Parker, T. J. Broxton, "Solvation of Ions. XIV. Protic-dipolar aprotic solvent effects on rates of bimolecular reactions. Solvent activity coefficients of reactants and transition states at 25°", *Journal of the American Chemical Society* **1968**, *90*, 5049–5069, DOI 10.5005/jp/books/10642_2.

[190] Z. Yang, X.-J. Liu, C. Chen, P. J. Halling, "Hofmeister effects on activity and stability of alkaline phosphatase", *Biochimica et Biophysica Acta* **2010**, *1804*, 821–828, DOI 10.1016/j.bbapap.2009.12.005.

[191] P. Lo Nostro, B. W. Ninham, "Hofmeister phenomena: An update on ion specificity in biology", *Chemical Reviews* **2012**, *112*, 2286–2322, DOI 10.1021/cr200271j.

[192] A. M. Hyde, S. L. Zultanski, J. H. Waldman, Y.-L. Zhong, M. Shevlin, F. Peng, "General principles and strategies for salting-out informed by the Hofmeister series", *Organic Process Research and Development* **2017**, *21*, 1355–1370, DOI 10.1021/acs.oprd.7b00197.

[193] E. E. Bruce, H. I. Okur, S. Stegmaier, C. I. Drexler, B. A. Rogers, N. F. van der Vegt, S. Roke, P. S. Cremer, "Molecular mechanism for the interactions of Hofmeister cations with macromolecules in aqueous solution", *Journal of the American Chemical Society* **2020**, *142*, 19094–19100, DOI 10.1021/jacs.0c07214.

[194] E. E. Bruce, P. T. Bui, B. A. Rogers, P. S. Cremer, N. F. van der Vegt, "Nonadditive ion effects drive both collapse and swelling of thermoresponsive polymers in water", *Journal of the American Chemical Society* **2019**, *141*, 6609–6616, DOI 10.1021/jacs.9b00295.

[195] L. Pérez-Fuentes, D. Bastos-González, J. Faraudo, C. Drummond, "Effect of organic and inorganic ions on the lower critical solution transition and aggregation of PNIPAM", *Soft Matter* **2018**, *14*, 7818–7828, DOI 10.1039/c8sm01679h.

[196] K. Sakota, D. Tabata, H. Sekiya, "Macromolecular crowding modifies the impact of specific Hofmeister ions on the coil-globule transition of PNIPAM", *Journal of Physical Chemistry B* **2015**, *119*, 10334–10340, DOI 10.1021/acs.jpcb.5b01255.

[197] D. R. Lide, *CRC Handbook of Chemistry and Physics*, 84th ed., CRC Press, Boca Raton, **2003**.

[198] L. Konermann, J. Pan, Y.-H. Liu, "Hydrogen exchange mass spectrometry for studying protein structure and dynamics", *Chemical Society Reviews* **2011**, *40*, 1224–1234, DOI 10.1039/c0cs00113a.

[199] M. Mahalakshmi, S. Selvanayagam, S. Selvasekarapandian, V. Moniha, R. Manjuladevi, P. Sangeetha, "Characterization of biopolymer electrolytes based on cellulose acetate with magnesium perchlorate ($Mg(ClO_4)_2$) for energy storage devices", *Journal of Science: Advanced Materials and Devices* **2019**, *4*, 276–284, DOI 10.1016/j.jsamd.2019.04.006.

[200] S. Shanmuga Priya, M. Karthika, S. Selvasekarapandian, R. Manjuladevi, S. Monisha, "Study of biopolymer I-carrageenan with magnesium perchlorate", *Ionics* **2018**, *24*, 3861–3875, DOI 10.1007/s11581-018-2535-1.

[201] R. Manjuladevi, M. Thamilselvan, S. Selvasekarapandian, R. Mangalam, M. Premalatha, S. Monisha, "Mg-ion conducting blend polymer electrolyte based on poly(vinyl alcohol)-poly (acrylonitrile) with magnesium perchlorate", *Solid State Ionics* **2017**, *308*, 90–100, DOI 10.1016/j.ssi.2017.06.002.

[202] M. Mahalakshmi, S. Selvanayagam, S. Selvasekarapandian, M. V. Leena Chandra, P. Sangeetha, R. Manjuladevi, "Magnesium ion-conducting solid polymer electrolyte based on cellulose acetate with magnesium nitrate ($Mg(NO_3)_2 \cdot 6H_2O$) for electrochemical studies", *Ionics* **2020**, *26*, 4553–4565, DOI 10.1007/s11581-020-03615-4.

[203] R. Manjuladevi, S. Selvasekarapandian, M. Thamilselvan, R. Mangalam, S. Monisha, P. C. Selvin, "A study on blend polymer electrolyte based on poly(vinyl alcohol)-poly (acrylonitrile) with magnesium nitrate for magnesium battery", *Ionics* **2018**, *24*, 3493–3506, DOI 10.1007/s11581-018-2500-z.

[204] S. Shanmuga Priya, M. Karthika, S. Selvasekarapandian, R. Manjuladevi, "Preparation and characterization of polymer electrolyte based on biopolymer I - Carrageenan with magnesium nitrate", *Solid State Ionics* **2018**, *327*, 136–149, DOI 10.1016/j.ssi.2018.10.031.

[205] I. Noda, "Two-dimensional infrared spectroscopy", *Journal of American Chemical Society* **1989**, *111*, 8116–8118, DOI 10.1021/ja00203a008.

[206] B. Sun, Y. Lin, P. Wu, H. W. Siesler, "A FTIR and 2D-IR spectroscopic study on the microdynamics phase separation mechanism of the poly(*N*-isopropylacrylamide) aqueous solution", *Macromolecules* **2008**, *41*, 1512–1520, DOI 10.1021/ma702062h.

[207] B. Sun, Y. Lin, P. Wu, "Structure analysis of poly(N-isopropylacrylamide) using near-infrared spectroscopy and generalized two-dimensional correlation infrared spectroscopy", *Applied Spectroscopy* **2007**, *61*, 765–771, DOI 10.1366/000370207781393271.

[208] Y. Maeda, T. Nakamura, I. Ikeda, "Changes in the hydration states of poly(*N*-alkylacrylamide)s during their phase transitions in water observed by FTIR spectroscopy", *Macromolecules* **2001**, *34*, 1391–1399, DOI 10.1021/ma001306t.

[209] D. Roy, J. N. Cambre, B. S. Sumerlin, "Future perspectives and recent advances in stimuli-responsive materials", *Progress in Polymer Science* **2010**, *35*, 278–301, DOI 10.1016/j.progpolymsci.2009.10.008.

[210] X. Xu, N. Bizmark, K. S. Christie, S. S. Datta, Z. J. Ren, R. D. Priestley, "Thermoresponsive polymers for water treatment and collection", *Macromolecules* **2022**, *55*, 1894–1909, DOI 10.1021/acs.macromol.1c01502.

[211] M. Concilio, V. P. Beyer, C. R. Becer, "Thermoresponsive polymers in non-aqueous solutions", *Polymer Chemistry* **2022**, *13*, 6423–6474, DOI 10.1039/d2py01147f.

[212] F. Doberenz, K. Zeng, C. Willems, K. Zhang, T. Groth, "Thermoresponsive polymers and their biomedical application in tissue engineering - A review", *Journal of Materials Chemistry B* **2020**, *8*, 607–628, DOI 10.1039/c9tb02052g.

[213] M. A. Ward, T. K. Georgiou, "Thermoresponsive polymers for biomedical applications", *Polymers* **2011**, *3*, 1215–1242, DOI 10.3390/polym3031215.

[214] C. M. Papadakis, P. Müller-Buschbaum, A. Laschewsky, "Switch it inside-out: "Schizophrenic" behavior of all thermoresponsive UCST-LCST diblock copolymers", *Langmuir* **2019**, *35*, 9660–9676, DOI 10.1021/acs.langmuir.9b01444.

[215] Y. Kotsuchibashi, M. Ebara, T. Aoyagi, R. Narain, "Recent advances in dual temperature responsive block copolymers and their potential as biomedical applications", *Polymers* **2016**, *8*, 380, DOI 10.3390/polym8110380.

[216] C. Hofmann, M. Schönhoff, "Do additives shift the LCST of poly (*N*-isopropylacrylamide) by solvent quality changes or by direct interactions?", *Colloid and Polymer Science* **2009**, *287*, 1369–1376, DOI 10.1007/s00396-009-2103-3.

[217] M. Panayiotou, F. Garret-Flaudy, R. Freitag, "Co-nonsolvency effects in the thermoprecipitation of oligomeric polyacrylamides from hydro-organic solutions", *Polymer* **2004**, *45*, 3055–3061, DOI 10.1016/j.polymer.2004.02.046.

[218] R. Umapathi, P. M. Reddy, A. Rani, P. Venkatesu, "Influence of additives on thermoresponsive polymers in aqueous media: A case study of poly(*N*-isopropylacrylamide)", *Physical Chemistry Chemical Physics* **2018**, *20*, 9717–9744, DOI 10.1039/c7cp08172c.

[219] H. Yong, J.-U. Sommer, "Cononsolvency effect: When the hydrogen bonding between a polymer and a cosolvent matters", *Macromolecules* **2022**, *55*, 11034–11050, DOI 10.1021/acs.macromol.2c01428.

[220] K. Kyriakos, M. Philipp, L. Silvi, W. Lohstroh, W. Petry, P. Müller-Buschbaum, C. M. Papadakis, "Solvent dynamics in solutions of PNIPAM in water/methanol mixtures - A quasi-elastic neutron scattering study", *Journal of Physical Chemistry B* **2016**, *120*, 4679–4688, DOI 10.1021/acs.jpcb.6b01200.

[221] B. Liu, J. Wang, G. Ru, C. Liu, J. Feng, "Phase transition and preferential alcohol adsorption of poly(*N*,*N*-diethylacrylamide) gel in water/alcohol mixtures", *Macromolecules* **2015**, *48*, 1126–1133, DOI 10.1021/ma502393z.

[222] S. Sun, P. Wu, "Role of water/methanol clustering dynamics on thermosensitivity of poly(N-isopropylacrylamide) from spectral and calorimetric insights", *Macromolecules* **2010**, *43*, 9501–9510, DOI 10.1021/ma1016693.

[223] Q. Zhang, R. Hoogenboom, "Polymers with upper critical solution temperature behavior in alcohol/water solvent mixtures", *Progress in Polymer Science* **2015**, *48*, 122–142, DOI 10.1016/j.progpolymsci.2015.02.003.

[224] N. Osaka, M. Shibayama, "Pressure effects on cononsolvency behavior of poly(*N*-isopropylacrylamide) in water/DMSO mixed solvents", *Macromolecules* **2012**, *45*, 2171–2174, DOI 10.1021/ma2027116.

[225] D. Ihara, Y. Higaki, N. L. Yamada, F. Nemoto, Y. Matsuda, K. Kojio, A. Takahara, "Cononsolvency of poly[2-(methacryloyloxy)ethyl phosphorylcholine] in ethanol-water mixtures: A neutron reflectivity study", *Langmuir* **2022**, *38*, 5081–5088, DOI 10.1021/acs.langmuir.1c01762.

[226] S. Backes, P. Krause, W. Tabaka, M. U. Witt, D. Mukherji, K. Kremer, R. von Klitzing, "Poly(*N*-isopropylacrylamide) microgels under alcoholic intoxication: When a LCST polymer shows swelling with increasing temperature", *ACS Macro Letters* **2017**, *6*, 1042–1046, DOI 10.1021/acsmacrolett.7b00557.

[227] Q. Chen, E. S. Kooij, X. Sui, C. J. Padberg, M. A. Hempenius, P. M. Schön, G. J. Vancso, "Collapse from the top: Brushes of poly(*N*-isopropylacrylamide) in cononsolvent mixtures", *Soft Matter* **2014**, *10*, 3134–3142, DOI 10.1039/c4sm00195h.

[228] H. Yong, E. Bittrich, P. Uhlmann, A. Fery, J.-U. Sommer, "Co-Nonsolvency transition of poly(*N*-isopropylacrylamide) brushes in a series of binary mixtures", *Macromolecules* **2019**, *52*, 6285–6293, DOI 10.1021/acs.macromol.9b01286.

[229] C.-H. Ko, P. Wastian, D. Schanzenbach, P. Müller-Buschbaum, A. Laschewsky, C. M. Papadakis, "Dynamic behavior of poly(*N*-isopropylmethacrylamide) in neat water and in water/methanol mixtures", *Langmuir* **2024**, *40*, 15150–15160, DOI 10.1021/acs.langmuir.4c01515.

[230] M. M. Bloksma, D. J. Bakker, C. Weber, R. Hoogenboom, U. S. Schubert, "The effect of hofmeister salts on the LCST transition of poly(2-oxazoline)s with varying hydrophilicity", *Macromolecular Rapid Communications* **2010**, *31*, 724–728, DOI 10.1002/marc.200900843.

[231] J. Reitenbach, P. Wang, L. F. Huber, S. A. Wegener, R. Cubitt, D. Schanzenbach, A. Laschewsky, C. M. Papadakis, P. Müller-Buschbaum, "Salt-mediated tuning of the Cononsolvency response behavior of PNIPMAM thin films", *Macromolecules* **2024**, *57*, 10635–10647, DOI 10.1021/acs.macromol.4c02053.

[232] I. Noda, A. Dowrey, C. Marcott, "Recent developments in two-dimensional infrared (2D IR) correlation spectroscopy", *Applied Spectroscopy* **1993**, *47*, 1317–1323, DOI 10.1016/j.cclet.2014.10.006.

List of Publications

Publications Related to the Thesis

- **J. Reitenbach**, C. Geiger, P. Wang, A. Vagias, R. Cubitt, D. Schanzenbach, A. Laschewsky, C. M. Papadakis, P. Müller-Buschbaum, Effect of Magnesium Salts with Chaotropic Anions on the Swelling Behavior of PNIPMAM Thin Films. *Macromolecules* 2023, 56, 2, 567-577.

  (DOI: 10.1021/acs.macromol.2c02282)

- **J. Reitenbach**, P. Wang, L. F. Huber, S. A. Wegener, R. Cubitt, D. Schanzenbach, A. Laschewsky, C. M. Papadakis, P. Müller-Buschbaum, Salt-Mediated Tuning of the Cononsolvency Response Behavior of PNIPMAM Thin Films. *Macromolecules* 2024, 57, 22, 10635-10647.

  (DOI: 10.1021/acs.macromol.4c02053)

Further Publications

- C. Geiger, **J. Reitenbach**, L. P. Kreuzer, T. Widmann, P. Wang, R. Cubitt, C. Henschel, A. Laschewsky, C. M. Papadakis, P. Müller-Buschbaum, PMMA-*b*-PNIPAM Thin Films Display Cononsolvency-Driven Response in Mixed Water/Methanol Vapors. *Macromolecules* 2021, 54, 7, 3517-3530.

  (DOI: 10.1021/acs.macromol.1c00021)

- C. Geiger, **J. Reitenbach**, C. Henschel, L. P. Kreuzer, T. Widmann, P. Wang, G. Mangiapia, J.-F. Moulin, C. M. Papadakis, A. Laschewsky, P. Müller-Buschbaum, Ternary Nanoswitches Realized with Multiresponsive PMMA-*b*-PNIPMAM Films in Mixed Water/Acetone Vapor Atmospheres. *Adv. Eng. Mater.* 2021, 23, 11, 2100191.

  (DOI: 10.1002/adem.202100191)

- A. J. Schmid, L. Wiehemeier, S. Jaksch, H. Schneider, A. Hiess, T. Bögershausen, T. Widmann, **J. Reitenbach**, L. P. Kreuzer, M. Kühnhammer, O. Löhmann, G. Brandl, H. Frielinghaus, P. Müller-Buschbaum, R. von Klizting, T. Hellweg, European Spallation Source: Part I - The In Situ SANS/DLS Setup. *Appl. Sci.* 2021, 11, 9, 4089.

  (DOI: 10.3390/app11094089)

- P. Wang, C. Geiger, L. P. Kreuzer, T. Widmann, **J. Reitenbach**, S. Liang, R. Cubitt, C. Henschel, A. Laschewsky, C. M. Papadakis, P. Müller-Buschbaum, Poly(sulfobetaine)-Based Diblock Copolymer Thin Films in Water/Acetone Atmosphere: Modulation of Water Hydration and Co-nonsolvency-Triggered Film Contraction. *Langmuir* 2022, 38, 22, 6934-6948.

  (DOI: 10.1021/acs.langmuir.2c00451)

- X. Jiang, P. Chotard, K. Luo, F. Eckmann, S. Tu, M. A. Reus, S. Yin, **J. Reitenbach**, C. L. Weindl, M. Schwartzkopf, S. V. Roth, P. Müller-Buschbaum, Revealing Donor-Acceptor Interaction on the Printed Active Layer Morphology and the Formation Kinetics for Nonfullerene Organic Solar Cells at Ambient Conditions. *Adv. Energy Mater.* 2022, 12, 2103977.

  (DOI: 10.1002/aenm.202103977)

- P. Wang, C. Geiger, **J. Reitenbach**, A. Vagias, L. P. Kreuzer, S. Liang, R. Cubitt, V. Hildebrand, A. Laschewsky, C. M. Papadakis, P. Müller-Buschbaum, KCl-Modulated Hydration and Subsequent Thermoresponsive Behavior of Poly(sulfobetaine)-Based Diblock Copolymer Thin Films. *Macromolecules* 2023, 56, 11, 4087-4099.

  (DOI: 10.1021/acs.macromol.3c00484)

- A. Vagias, A. Nelson, P. Wang, **J. Reitenbach**, C. Geiger, L. P. Kreuzer, T. Saerbeck, R. Cubitt, E. M. Benetti, P. Müller-Buschbaum, The Topology of Polymer Brushes Determines Their Nanoscale Hydration. *Macromol. Rapid Commun.* 2023, 44, 2300035.

  (DOI: 10.1002/marc.202300035)

- P. Wang, T. Zheng, **J. Reitenbach**, S. A. Wegener, L. F. Huber, L. P. Kreuzer, S. Liang, R. Cubitt, Y.-J. Cheng, T. Xu, V. Hildebrand, A. Laschewsky, C. M. Papadakis, P. Müller-Buschbaum, Solvation Dynamics of Thermoresponsive Polymer Films: The Influence of Salt Series in Water and Mixed Water/Methanol Atmosphere. *Adv. Sci.* 2025, 12, 2408073.

(DOI: 10.1002/advs.202408073)

- M. P. Le Dû, **J. Reitenbach**, D. P. Kosbahn, L. V. Spanier, R. Cubitt, C. Henschel, A. Laschewsky, C. M. Papadakis, P. Müller-Buschbaum, Comparison of the Swelling Behavior of Poly(*N*-Isopropylacrylamide) and Poly(*N*-Vinylisobutyramide) Thin Films under Water Vapor Exposure. *Macromolecules* 2025, 58, 2, 1000-1010.
  (DOI: 10.1021/acs.macromol.4c02802)

Conference Contributions

Talks

- J. Reitenbach, C. Geiger, P. Wang, A. Vagias, R. Cubitt, D. Schanzenbach, A. Laschewsky, C. M. Papadakis, P. Müller-Buschbaum
  Investigation of the Effect of Magnesium Salts with Chaotropic Anions on the Swelling Behavior of PNIPMAM Thin Films
  European Polymer Federation, 27 June - 01 July 2022

- J. Reitenbach, C. Geiger, P. Wang, A. Vagias, R. Cubitt, D. Schanzenbach, A. Laschewsky, C. M. Papadakis, P. Müller-Buschbaum
  Investigation of the Effect of Magnesium Salts with Chaotropic Anions on the Swelling Behavior of PNIPMAM Thin Films
  DPG-Tagung der Sektion Kondensierte Materie, 04 - 09 September 2022

- J. Reitenbach, C. Geiger, P. Wang, A. Vagias, R. Cubitt, D. Schanzenbach, A. Laschewsky, C. M. Papadakis, P. Müller-Buschbaum
  Tuning the Sensitivity of PNIPMAM-based Nanosensors by the Addition of Salts
  ACS Spring 2023, Indianapolis, 26 - 30 March 2023

- J. Reitenbach, C. Geiger, P. Wang, T. Widmann, L. P. Kreuzer, R. Cubitt, D. Schanzenbach, A. Laschewsky, C. M. Papadakis, P. Müller-Buschbaum
  Investigation of the Solvent Uptake in Salt-containing PNIPMAM Thin Films
  MLZ User Meeting 2023, Garching, 04 - 05 December 2023

- J. Reitenbach, P. Wang, L. F. Huber, S. A. Wegener, R. Cubitt, D. Schanzenbach, A. Laschewsky, C. M. Papadakis, P. Müller-Buschbaum
  Investigation of the Solvent Uptake of Salt-containing PNIPMAM Thin Films
  DPG-Frühjahrstagung der Sektion Kondensierte Materie, 18 - 22 September 2024

- J. Reitenbach
  Influence of Salt Addition on the Responsiveness of PNIPMAM Thin Films Towards Solvent Vapor Atmospheres
  Sino-German Workshop, Exploration of Structure and Morphology in Polymers by Advanced Scattering Techniques (ExpAdvScaTech), 14 - 17 October 2024

Posters

- J. Reitenbach, C. Geiger, L. P. Kreuzer, T. Widmann, P. Wang, G. Mangiapia, C. Henschel, A. Laschewsky, C. M. Papadakis, P. Müller-Buschbaum
  Cononsolvency-induced Collapse Transition in Thin PMMA-b-PNIPMAM Films
  Osmolyte and Cosolvent Effects in Stimuli-responsive Polymers Virtual Conference, 25 - 26 February 2021

- J. Reitenbach, C. Geiger, L. P. Kreuzer, T. Widmann, P. Wang, G. Mangiapia, C. Henschel, A. Laschewsky, C. M. Papadakis, P. Müller-Buschbaum
  Cononsolvency-induced Collapse Transition in Thin PMMA-b-PNIPMAM Films
  ACS Spring Meeting 2021, 05 – 30 April 2021

- J. Reitenbach, C. Geiger, P. Wang, R. Cubitt, D. Schanzenbach, A. Laschewsky, C. M. Papadakis, P. Müller-Buschbaum
  Investigation of the Effect of Magnesium Salts with Chaotropic Anions on the Swelling Behavior of PNIPMAM Thin Films
  Virtual DPG Spring Meeting 2021, 27 September – 01 October 2021

- J. Reitenbach, C. Geiger, P. Wang, R. Cubitt, D. Schanzenbach, A. Laschewsky, C. M. Papadakis, P. Müller-Buschbaum
  Influence of Hofmeister Salts on the Swelling Behavior of PNIPMAM Thin Films
  MLZ User Meeting 2021, 07 – 08 December 2021

- J. Reitenbach, C. Geiger, P. Wang, A. Vagias, R. Cubitt, D. Schanzenbach, A. Laschewsky, C. M. Papadakis, P. Müller-Buschbaum
  Fine-tuning the Swelling Behavior of PNIPMAM Thin Films — The Case of Salt Addition
  European Conference on Neutron Scattering, Garching, 20 - 23 March 2023

Acknowledgments

This thesis would not have been possible without the support and cooperation of the remarkable people I had the privilege to work with during my time as a Ph.D. student at the Chair of Functional Materials. This period of my life has shaped and inspired me not only in my scientific journey, but also in my personal growth, on which many people have had a pronounced influence, and I would like to thank them at the end of this thesis.

First of all, I would like to thank my supervisor, Prof. Dr. Peter Müller-Buschbaum, for giving me the opportunity to work on this unique topic and for his scientific support, trust, and encouragement. Being a Ph.D. student at his chair gave me the opportunity to realize my own scientific ideas and to present my research at various national and international conferences. Furthermore, the chance to perform experiments at large neutron facilities allowed me to collaborate with many amazing scientists from different fields.

A special thanks goes to Prof. Dr. Christine M. Papadakis for being my mentor during my Ph.D. studies. Her honest and straightforward way of giving valuable feedback and her efforts to improve my scientific writing have greatly benefited my research.

None of my experimental work would have been possible without the fruitful collaboration with Prof. Dr. André Laschewsky and Dr. Dirk Schanzenbach from the University of Potsdam. I am grateful for their efforts in synthesizing, characterizing, and providing the homopolymer PNIPMAM investigated in this work. Their scientific knowledge and sharing were essential to gaining a fundamental understanding of the material and developing interesting and impactful experiments.

I would like to thank Dr. Robert Cubitt of the ILL neutron facility in France for his time, patience, and thoughtfulness. His guidance enabled me to perform and understand the unique and complex neutron measurements, which improved the scientific outcome of the presented studies.

I want to thank all current and former members of the hydrogel group, namely Christina Geiger, David Kosbahn, Dr. Lucas Kreuzer, Morgan Le Dû, Dr. Peixi Wang and Tobias

Widmann for the warm welcome, the support and the various scientific discussions at the beginning and throughout. Tinkering, maintaining and using our many custom setups has been a challenging but exciting experience where I could not have been in better hands.

My gratitude goes to all my beamtime colleagues Thomas Baier, Christina Geiger, Linus Huber, David Kosbahn, Dr. Lucas Kreuzer, Morgan Le Dû, Lukas Spanier, Dr. Peixi Wang, Simon Wegener, Dr. Apostolos Vagias and Prof. Dr. Qi Zhong for their help and support. Thank you for your patience in driving the long distance between Munich and Grenoble and for being reliable companions during the many day and night shifts. The trips were always joyful events, full of unforgettable memories and extraordinary moments.

I would like to express my sincere thanks to all the members of the Chair of Functional Materials and the Soft Matter Physics Group who have not yet been mentioned. I have thoroughly enjoyed the pleasant working environment, the harmonious and friendly atmosphere, and the delightful intercultural events. Many of them took an integral role in the group and became very dear friends over the years, namely Fabian Apfelbeck, Altantulga Buyan-Arivjikh, Christopher Everett, Dr. Tianfu Guan, Dr. Julian Heger, Pablo Alvarez Herrera, Dr. Xinyu Jiang, Yanan Li, Zerui Li, Yuxin Liang, Dr. Anna Lena Oechsle, Dominik Petz, Thien An Pham, Ivana Pivarnikova, Dr. Lennart Reb, Manuel Reus, Dr. Dominik Schwaiger, Kun Sun, Dr. Christian Weindl, Dr. Kerstin Wienhold, Tianxiao Xiao, Peiran Zhang, Feifei Zheng, and Huaying Zhong. Especially for the long walks along the Isar river, the spontaneous get-togethers after long working days, and the support in various areas of life.

I would also like to thank all those who work in the background of the chair for their efforts in organizing, assisting in bureaucratic matters, and assembling and establishing projects. Thanks to Carola Kappauf, Marion Waletzki, and Sanja Ulrich for their support in all administrative matters. I am grateful for the cooperation with Reinhold Funer, who had endless patience and a very good way to describe technical peculiarities – even to the uninitiated – and to realize unique plans. I would also like to thank Josef Kaplonski for all the hard work he put into the chair, organizing complex lab renovations, and always having an open door.

The financial and scientific support from the FlexiProb project is kindly appreciated. The collaboration between the groups of Prof. Dr. Thomas Hellweg, Prof. Dr. Regine von Klitzing, and Prof. Dr. Peter Müller-Buschbaum as well as with all associated group members was a great experience. The FlexiProb project gave me an insight into the

acquisition of funding and the opportunity to work with great scientists in the field of neutron scattering techniques.

My greatest gratitude belongs to my family and friends, who provided unconditional support, have always been there and affirmed me. I want to thank my mother Irina for encouraging me to pursue my studies and being my biggest supporter. Finally, I would like to express my deepest gratitude to my partner Felix, whose love, patience and understanding have been my constant source of strength and have made this achievement possible.